Supplement of: An advanced modelling study on the role of dimethyl sulfide in new particle formation in the pristine marine boundary layer

Robin Wollesen de Jonge[1], Zihao Fu[1,2], Pontus Roldin[3], and Michael Boy[1,4,5]

[1]Institute for Atmospheric and Earth Systems Research, University of Helsinki, FI-00014 Helsinki, Finland
[2]State Key Laboratory of Regional Environment and Sustainability, International Joint Laboratory for Regional Pollution Control, Ministry of Education (IJRC), College of Environmental Sciences and Engineering, Peking University, CN-100871 Beijing, China
[3]Department of Physics, Lund University, Lund SE-22363, Sweden
[4]Atmospheric Modelling Centre – Lahti, Lahti University Campus, FI-15110 Lahti, Finland
[5]School of Engineering Sciences, Lappeenranta-Lahti University of Technology LUT, Lahti FI-15110, Finland

Correspondence: Robin Wollesen de Jonge (robin.wollesendejonge@helsinki.fi)

Contents

S1 DMS oxidation mechanism

Table S1. Gas-phase DMS reactions

Nr.	Reaction			Reaction Rate Coefficient	Ref.
G1	DMS + OH	→	$CH_3SCH_2O_2$	$1.12 \times 10^{-11} \times \exp(-250/T)$	[A]
G2	DMS + OH	→	CH_3SOHCH_3	KMT18	[B]
G3	DMS + NO_3	→	$CH_3SCH_2O_2$ + HNO_3	$1.9 \times 10^{-13} \times \exp(520/T)$	[A]
G4	DMS + Cl	→	$CH_3SCH_2O_2$ + HCl	$0.45 \times 3.4 \times 10^{-10}$	[B]
G5	DMS + Cl	→	CH_3SCH_3Cl	$0.55 \times 3.4 \times 10^{-10}$	[B]
G6	DMS + ClO	→	DMSO + Cl	$0.73 \times 1.7 \times 10^{-15} \times \exp(340/T)$	[B]
G7	DMS + ClO	→	$CH_3SCH_2O_2$ + HOCl	$0.27 \times 1.7 \times 10^{-15} \times \exp(340/T)$	[B]
G8	DMS + Cl2	→	CH_3SCH_2Cl + HCl	3.4×10^{-14}	[B]
G9	DMS + Br	→	$CH_3SCH_2O_2$ + HBr	$9 \times 10^{-11} \times \exp(-2390/T)$	[B]
G10	DMS + Br	→	CH_3SCH_3Br	KMT54	[B]
G11	DMS + BrO	→	DMSO + Br	$1.5 \times 10^{-14} \times \exp(1000/T)$	[B]
G12	DMS + IO	→	DMSO + I	$3.3 \times 10^{-13} \times \exp(-925/T)$	[B]
G13	CH_3SOHCH_3	→	DMS + OH	$(1.7 \times 10^{-42} \times [O_2] \times \exp(7810/T)$ /$(1+5.5 \times 10^{-31} \times [O_2] \times \exp(7640/T)))$ /$(8.3 \times 10^{-29} \times T \times \exp(5136/T))$	[B]
G14	CH_3SOHCH_3	→	$HODMSO_2$	$8.5 \times 10^{-13} \times [O_2]$	[B]
G15	CH_3SOHCH_3	→	CH_3SOH + CH_3O_2	5×10^{5}	[B]
G16	CH_3SOH + OH	→	CH_3SO	5×10^{-11}	[B]
G17	CH_3SCH_2Cl + OH	→	CH_3SOH + CH_2ClO_2	2.5×10^{-12}	[B]
G18	CH_3SCH_3Cl + NO_2	→	DMS + $ClNO_2$	2.7×10^{-11}	[B]
G19	CH_3SCH_3Cl + NO	→	DMS + ClNO	1.2×10^{-11}	[B]
G20	CH_3SCH_3Cl	→	DMSO + ClO	$4 \times 10^{-18} \times [O_2]$	[B]
G21	CH_3SCH_3Cl	→	DMS + Cl	9×10^{1}	[B]
G22	CH_3SOCH_3Cl	→	$DMSO_2$ + ClO	$3 \times 10^{-18} \times [O_2]$	[B]
G23	CH_3SOCH_3Cl + NO	→	DMSO + ClNO	1.2×10^{-11}	[B]
G24	CH_3SOCH_3Cl + NO_2	→	DMSO + $ClNO_2$	2.1×10^{-11}	[B]
G25	CH_3SOCH_3Cl + CH_3SOCH_3Cl	→	DMSO + DMSO + Cl2	3×10^{-11}	[B]
G26	CH_3SOCH_3Cl	→	DMSO + Cl	9×10^{1}	[B]
G27	CH_3SCH_3Br	→	DMSO + BrO	$1 \times 10^{-18} \times [O_2]$	[B]
G28	CH_3SCH_3Br	→	DMS + Br	1.02×10^{4}	[B]
G29	DMSO + BrO	→	$DMSO_2$ + Br	1×10^{-14}	[B]

Table S1. Gas-phase DMS reactions continued

Nr.	Reaction			Reaction Rate Coefficient	Ref.
G30	$CH_3SCH_2O_2$	$\rightarrow$	$OOCH_2SCH_2OOH$	$2.2433 \times 10^{11} \times \exp(-9.8016 \times 10^3/T) \times \exp(1.0348 \times 10^8/T^3) \times 2.75$	[C][D]
G31	$OOCH_2SCH_2OOH$	$\rightarrow$	HPMTF + OH	$6.097 \times 10^{11} \times \exp(-9.4892 \times 10^3/T) \times \exp(1.102 \times 10^8/T^3)$	[C]
G32	$OOCH_2SCH_2OOH$ + NO	$\rightarrow$	$HOOCH_2S$ + NO_2 + HCHO	$4.9 \times 10^{-12} \times \exp(260/T)$	[C]
G33	$OOCH_2SCH_2OOH$ + HO_2	$\rightarrow$	$HOOCH_2SCH_2OOH$	$1.13 \times 10^{-13} \times \exp(1300/T)$	[C]
G34	HPMTF + OH	$\rightarrow$	$HOOCH_2SCO$	2.1×10^{-11}	[D]
G35	$HOOCH_2SCO$	$\rightarrow$	$HOOCH_2S$ + CO	$9.2 \times 10^9 \times \exp(-505.4/T)$	[E]
G36	$HOOCH_2SCO$	$\rightarrow$	HCHO + OH + OCS	$1.6 \times 10^7 \times \exp(-1468.6/T)$	[E]
G37	$HOOCH_2S$ + O_3	$\rightarrow$	$HOOCH_2SO$	$1.15 \times 10^{-12} \times \exp(430/T)$	[E]
G38	$HOOCH_2S$ + NO_2	$\rightarrow$	$HOOCH_2SO$ + NO	$6.00 \times 10^{-11} \times \exp(240/T)$	[E]
G39	$HOOCH_2SO$ + O_3	$\rightarrow$	SO_2 + HCHO + OH	4.00×10^{-13}	[E]
G40	$HOOCH_2SO$ + NO_2	$\rightarrow$	SO_2 + HCHO + OH + NO	1.20×10^{-11}	[E]
G41	CH_3SOH + O_3	$\rightarrow$	CH_3O_2 + HO_2 + SO_2	2×10^{-12}	[F]
G42	$CH_3SCH_2O_2$ + HO_2	$\rightarrow$	CH_3SCH_2OOH	$KRO_2HO_2 \times 0.387$	[A]
G43	$CH_3SCH_2O_2$ + NO	$\rightarrow$	CH_3SCH_2O + NO_2	$4.9 \times 10^{-12} \times \exp(260/T)$	[A]
G44	$CH_3SCH_2O_2$ + NO_3	$\rightarrow$	CH_3SCH_2O + NO_2	KRO_2NO_3	[A]
G45	$CH_3SCH_2O_2$	$\rightarrow$	CH_3SCH_2O	$3.74 \times 10^{-12} \times [RO_2] \times 0.8$	[A]
G46	$CH_3SCH_2O_2$	$\rightarrow$	CH_3SCH_2OH	$3.74 \times 10^{-12} \times [RO_2] \times 0.1$	[A]
G47	$CH_3SCH_2O_2$	$\rightarrow$	CH_3SCHO	$3.74 \times 10^{-12} \times [RO_2] \times 0.1$	[A]
G48	$HODMSO_2$ + NO	$\rightarrow$	$DMSO_2$ + HO_2 + NO_2	KRO_2NO	[A]
G49	$HODMSO_2$	$\rightarrow$	DMSO + HO_2	$8.90 \times 10^{10} \times \exp(-6040/T)$	[A]
G50	CH_3SCH_2OOH + OH	$\rightarrow$	CH_3SCHO + OH	7.03×10^{-11}	[A]
G51	CH_3SCH_2OOH	$\rightarrow$	CH_3SCH_2O + OH	J(41)	[A]
G52	CH_3SCH_2O	$\rightarrow$	CH_3S + HCHO	KDEC	[A]
G53	CH_3SCH_2OH + OH	$\rightarrow$	CH_3SCHO + HO_2	2.78×10^{-11}	[A]
G54	CH_3SCHO + OH	$\rightarrow$	CH_3S + CO	1.11×10^{-11}	[A]
G55	CH_3SCHO	$\rightarrow$	CH_3S + CO + HO_2	J(15)	[A]
G56	$DMSO_2$ + OH	$\rightarrow$	$DMSO_2O_2$	4.40×10^{-14}	[A]
G57	DMSO + OH	$\rightarrow$	MSIA + CH_3O_2	$6.10 \times 10^{-12} \times \exp(800/T)$	[A]
G58	DMSO + NO_3	$\rightarrow$	$DMSO_2$ + NO_2	2.9×10^{-13}	[B]
G59	DMSO + Cl	$\rightarrow$	$CH_3SOCH_2O_2$ + HCl	1.45×10^{-11}	[B]
G60	DMSO + Cl	$\rightarrow$	CH_3SOCH_3Cl	7.4×10^{-11}	[B]
G61	$CH_3SOCH_2O_2$ + NO	$\rightarrow$	CH_3SO + HCHO + NO_2	7.5×10^{-12}	[B]
G62	$CH_3SOCH_2O_2$ + HO_2	$\rightarrow$	CH_3SOCH_2OOH	1.5×10^{-12}	[B]

Table S1. Gas-phase DMS reactions continued

Nr.	Reaction			Reaction Rate Coefficient	Ref.
G63	MSIA + OH	→	CH_3SO_2	$4.3298 \times 10^{-12} \times \exp(904.2192/T)$	[G][H]
G64	MSIA + OH	→	HOMSIA	$9.6029 \times 10^{-13} \times \exp(825.0233/T)$	[G]
G65	HOMSIA	→	CH_3O_2 + SO_2	$1.7078 \times 10^{13} \times \exp(-1579.3/T)$	[G]
G66	HOMSIA	→	MSA + HO_2	$1.4388 \times 10^{-15} \times \exp(6181.5.3/T) \times [O_2]$	[G]
G67	MSIA + NO_3	→	CH_3SO_2 + HNO_3	1×10^{-13}	[B]
G68	CH_3SOO + HO_2	→	CH_3SOOH	4×10^{-12}	[B]
G69	CH_3SOO	→	CH_3SO_2	1	[B]
G70	CH_3SO_2 + OH	→	MSA	5×10^{-11}	[B]
G71	CH_3SO_2 + NO_2	→	CH_3SO_3 + NO	2.2×10^{-11}	[B]
G72	CH_3S + NO_2	→	CH_3SO + NO	$6.00 \times 10^{-11} \times \exp(240/T)$	[A]
G73	CH_3S + O_3	→	CH_3SO	$1.15 \times 10^{-12} \times \exp(430/T)$	[A]
G74	CH_3S	→	CH_3SOO	$1.20 \times 10^{-16} \times \exp(1580/T) \times [O_2]$	[A]
G75	$DMSO_2O_2$ + HO_2	→	$DMSO_2OOH$	$KRO_2HO_2 \times 0.387$	[A]
G76	$DMSO_2O_2$ + NO	→	$DMSO_2O$ + NO_2	KRO_2NO	[A]
G77	$DMSO_2O_2$ + NO_3	→	$DMSO_2O$ + NO_2	KRO_2NO_3	[A]
G78	$DMSO_2O_2$	→	CH_3SO_2CHO	$2.00 \times 10^{-12} \times [RO_2] \times 0.2$	[A]
G79	$DMSO_2O_2$	→	$DMSO_2O$	$2.00 \times 10^{-12} \times [RO_2] \times 0.6$	[A]
G80	$DMSO_2O_2$	→	$DMSO_2OH$	$2.00 \times 10^{-12} \times [RO_2] \times 0.2$	[A]
G81	CH_3SO + NO_2	→	CH_3O_2 + SO_2 + NO	$1.20 \times 10^{-11} \times 0.25$	[A]
G82	CH_3SO + NO_2	→	CH_3SO_2 + NO	$1.20 \times 10^{-11} \times 0.75$	[A]
G83	CH_3SO + O_3	→	CH_3O_2 + SO_2	4.00×10^{-13}	[A]
G84	CH_3SO	→	CH_3SOO_2	$3.12 \times 10^{-16} \times \exp(1580/T) \times [O_2]$	[A]
G85	CH_3SOO + NO	→	CH_3SO + NO_2	1.1×10^{-11}	[A]
G86	CH_3SOO + NO_2	→	CH_3SO + NO_3	2.2×10^{-11}	[A]
G87	CH_3SOO	→	CH_3O_2 + SO_2	$5.60 \times 10^{16} \times \exp(-10870/T)$	[A]
G88	CH_3SOO	→	CH_3S	$3.50 \times 10^{10} \times \exp(-3560/T)$	[A]
G89	$DMSO_2OOH$ + OH	→	CH_3SO_2CHO + OH	1.26×10^{-12}	[A]
G90	$DMSO_2OOH$ + OH	→	$DMSO_2O_2$	3.60×10^{-12}	[A]
G91	$DMSO_2OOH$	→	$DMSO_2O$ + OH	J(41)	[A]
G92	$DMSO_2O$	→	CH_3SO_2 + HCHO	KDEC	[A]
G93	CH_3SO_2CHO + OH	→	CH_3SO_2 + CO	1.78×10^{-12}	[A]
G94	CH_3SO_2CHO	→	CH_3SO_2 + CO + HO_2	J(15)	[A]
G95	$DMSO_2OH$ + OH	→	CH_3SO_2CHO + HO_2	5.23×10^{-13}	[A]
G96	$DMSO_2OH$ + OH	→	$DMSO_2O$	1.40×10^{-13}	[A]
G97	CH_3SO_2 + O_3	→	CH_3SO_3	3.00×10^{-13}	[A]

Table S1. Gas-phase DMS reactions continued

Nr.	Reaction			Reaction Rate Coefficient	Ref.
G98	CH_3SO_2	$\rightarrow$	$CH_3O_2 + SO_2$	$5.00 \times 10^{13} \times \exp(-9673/T)$	[A]
G99	CH_3SO_2	$\rightarrow$	$CH_3SO_2O_2$	$1.03 \times 10^{-16} \times \exp(1580/T) \times [O_2]$	[A]
G100	$CH_3SOO_2 + HO_2$	$\rightarrow$	$CH_3SO_2 + OH$	$KAPHO_2 \times 0.44$	[A]
G101	$CH_3SOO_2 + HO_2$	$\rightarrow$	CH_3SOOOH	$KAPHO_2 \times 0.41$	[A]
G102	$CH_3SOO_2 + HO_2$	$\rightarrow$	$MSIA + O_3$	$KAPHO_2 \times 0.15$	[A]
G103	$CH_3SOO_2 + NO$	$\rightarrow$	$CH_3SO_2 + NO_2$	1.00×10^{-11}	[A]
G104	$CH_3SOO_2 + NO_2$	$\rightarrow$	$CH_3SOO_2NO_2$	$1.20 \times 10^{-12} \times (T/300)^{-0.9}$	[A]
G105	$CH_3SOO_2 + NO_3$	$\rightarrow$	$CH_3SO_2 + NO_2$	$KRO_2NO_3 \times 1.74$	[A]
G106	CH_3SOO_2	$\rightarrow$	CH_3SO	$9.10 \times 10^{10} \times \exp(-3560/T)$	[A]
G107	CH_3SOO_2	$\rightarrow$	CH_3SO_2	$1.00 \times 10^{-11} \times [RO_2] \times 0.7$	[A]
G108	CH_3SOO_2	$\rightarrow$	MSIA	$1.00 \times 10^{-11} \times [RO_2] \times 0.3$	[A]
G109	$CH_3SO_3 + HO_2$	$\rightarrow$	MSA	5.00×10^{-11}	[A]
G110	$CH_3SO_3 + DMS$	$\rightarrow$	$MSA + CH_3SCH_2O_2$	1.45×10^{-13}	[I][J]
G111	CH_3SO_3	$\rightarrow$	$CH_3O_2 + SO_3$	$5.00 \times 10^{13} \times \exp(-9946/T)$	[A]
G112	$CH_3SO_2O_2 + HO_2$	$\rightarrow$	CH_3SO_2OOH	$KAPHO_2 \times 0.41$	[A]
G113	$CH_3SO_2O_2 + HO_2$	$\rightarrow$	$CH_3SO_3 + OH$	$KAPHO_2 \times 0.44$	[A]
G114	$CH_3SO_2O_2 + HO_2$	$\rightarrow$	$MSA + O_3$	$KAPHO_2 \times 0.15$	[A]
G115	$CH_3SO_2O_2 + NO$	$\rightarrow$	$CH_3SO_3 + NO_2$	1.00×10^{-11}	[A]
G116	$CH_3SO_2O_2 + NO_2$	$\rightarrow$	$CH_3SO_4NO_2$	$1.20 \times 10^{-12} \times (T/300)^{-0.9}$	[A]
G117	$CH_3SO_2O_2 + NO_3$	$\rightarrow$	$CH_3SO_3 + NO_2$	$KRO_2NO_3 \times 1.74$	[A]
G118	$CH_3SO_2O_2$	$\rightarrow$	CH_3SO_2	$3.01 \times 10^{10} \times \exp(-3560/T)$	[A]
G119	$CH_3SO_2O_2$	$\rightarrow$	CH_3SO_3	$1.00 \times 10^{-11} \times [RO_2] \times 0.7$	[A]
G120	$CH_3SO_2O_2$	$\rightarrow$	MSA	$1.00 \times 10^{-11} \times [RO_2] \times 0.3$	[A]
G121	$CH_3SOOOH + OH$	$\rightarrow$	CH_3SOO_2	9.00×10^{-11}	[A]
G122	CH_3SOOOH	$\rightarrow$	$CH_3SO_2 + OH$	J(41)	[A]
G123	$CH_3SOO_2NO_2 + OH$	$\rightarrow$	$MSIA + NO_2$	1.00×10^{-11}	[A]
G124	$CH_3SOO_2NO_2$	$\rightarrow$	$CH_3SOO_2 + NO_2$	$5.40 \times 10^{16} \times \exp(-13112/T)$	[A]

[A] MCMv3.1.1, [B] Hoffmann et al. (2016), [C] Veres et al. (2020), [D] Ye et al. (2022), [E] Wu et al. (2014), [F] Berndt et al. (2020), [G] This work, [H] Kukui et al. (2003), [I] Yin et al. (1990), [J] Jacob et al. (2024)

Table S2. Aqueous-phase DMS reactions

Nr.	Reaction			Reaction Rate Coefficient	Ref.
A1	DMS + O_3	$\rightarrow$	DMSO	$8.61 \times 10^8 \times$ exp(-2600 $\times$ (1/T-1/298));	[B]
A2	DMS + OH	$\rightarrow$	DMSO + HO_2	1.9×10^{10}	[B]
A3	DMS + Cl_2^-	$\rightarrow$	CH_3SCH_3Cl + Cl^-	3×10^9	[B]
A4	DMS + Br_2^-	$\rightarrow$	CH_3SCH_3Br + Br^-	3.2×10^9	[B]
A5	DMS + H_2O_2	$\rightarrow$	DMSO	3.4×10^{-2}	[B]
A6	CH_3SCH_3Cl + O_2	$\rightarrow$	DMSO + ClO	2.41×10^3	[B]
A7	CH_3SCH_3Br + O_2	$\rightarrow$	DMSO + BrO	6.02×10^2	[B]
A8	DMSO + O_3	$\rightarrow$	$DMSO_2$	3×10^0	[B]
A9	DMSO + OH	$\rightarrow$	MSIA	$6.65 \times 10^9 \times$ exp(-1270 $\times$ (1/T-1/298))	[B]
A10	DMSO + SO_4^-	$\rightarrow$	$DMSO^+$ + SO_4^{2-}	$2.97 \times 10^9 \times$ exp(-1440 $\times$ (1/T-1/298))	[B]
A11	DMSO + Cl	$\rightarrow$	CH_3SOCH_3Cl	6.3×10^9	[B]
A12	DMSO + Cl_2^-	$\rightarrow$	CH_3SOCH_3Cl + Cl^-	1.6×10^7	[B]
A13	DMSO + H_2O_2	$\rightarrow$	$DMSO_2$	2.75×10^{-6}	[B]
A14	DMSOion + Br^-	$\rightarrow$	CH_3SOCH_3Br	5×10^9	[B]
A15	CH_3SOCH_3Br + Br^-	$\rightarrow$	DMSO + Br_2^-	2.6×10^8	[B]
A16	CH_3SOCH_3Cl	$\rightarrow$	MSIA + HCl	$55.6 \times 1 \times 10^7$	[B]
A17	CH_3SOCH_3OH	$\rightarrow$	MSIA	1×10^7	[B]
A18	$DMSO_2$ + OH	$\rightarrow$	$CH_3SO_2CH_2$	$1.77 \times 10^7 \times$ exp(-1690 $\times$ (1/T-1/298))	[B]
A19	$DMSO_2$ + SO_4^-	$\rightarrow$	$CH_3SO_2CH_2$ + SO_4^{2-}	$3.95 \times 10^6 \times$ exp(-1360 $\times$ (1/T-1/298))	[B]
A20	$DMSO_2$ + Cl	$\rightarrow$	$CH_3SO_2CH_2$ + HCl	8.2×10^5	[B]
A21	$DMSO_2$ + Cl_2^-	$\rightarrow$	$CH_3SO_2CH_2$ + HCl + Cl^-	8.24×10^3	[B]
A22	$DMSO_2$ + O_2	$\rightarrow$	$CH_3SO_2CH_2O_2$	2×10^9	[B]
A23	MSIA + O_3	$\rightarrow$	CH_3SO_3H	3.5×10^7	[B]
A24	MSIA + OH	$\rightarrow$	$CH_3SO_3H_2$	6×10^9	[B]
A25	$CH_3SO_2^-$ + OH	$\rightarrow$	CH_3SO_2	$0.9 \times 1.2 \times 10^{10}$	[B]
A26	$CH_3SO_2^-$ + OH	$\rightarrow$	HSO_3^-	$0.1 \times 1.2 \times 10^{10}$	[B]
A27	$CH_3SO_2^-$ + SO_4^-	$\rightarrow$	CH_3SO_2 + SO_4^{2-}	1×10^9	[B]
A28	$CH_3SO_2^-$ + Cl_2^-	$\rightarrow$	CH_3SO_2 + Cl^- + Cl^-	8×10^8	[B]
A29	$CH_3SO_2^-$ + H_2O_2	$\rightarrow$	$CH_3SO_3^-$	1.2×10^{-2}	[B]
A30	$CH_3SO_2^-$ + O_3	$\rightarrow$	$CH_3SO_3^-$	2×10^6	[B]

Table S2. Aqueous-phase DMS reactions continued

Nr.	Reaction		Reaction Rate Coefficient	Ref.
A31	$CH_3SO_3H_2 + O_2$	$\rightarrow$ $CH_3SO_3H + HO_2$	1.2×10^9	[B]
A32	$CH_3SO_3H + OH$	$\rightarrow$ CH_2SO_3H	1.5×10^7	[B]
A33	$CH_3SO_3^- + OH$	$\rightarrow$ $CH_2SO_3^-$	$1.29 \times 10^7 \times \exp(-2630 \times (1/T-1/298))$	[B]
A34	$CH_3SO_3^- + SO_4^-$	$\rightarrow$ $CH_3SO_3 + SO_4^{2-}$	$1.13 \times 10^4 \times \exp(-2490 \times (1/T-1/298))$	[B]
A35	$CH_3SO_3^- + Cl$	$\rightarrow$ $CH_3SO_3 + Cl^-$	4.9×10^5	[B]
A36	$CH_3SO_3^- + Cl_2^-$	$\rightarrow$ $CH_3SO_3 + Cl^- + Cl^-$	3.89×10^3	[B]
A37	$CH_3SO_2 + OH$	$\rightarrow$ CH_3SO_3H	1×10^{10}	[B]
A38	$CH_3SO_2 + O_3$	$\rightarrow$ CH_3SO_3	1.5×10^9	[B]
A39	$CH_3SO_2 + SO_3^{2-}$	$\rightarrow$ $CH_3SO_2^- + SO_4^{2-}$	1.7×10^9	[B]
A40	CH_3SO_2	$\rightarrow$ SO_2	8.3×10^4	[B]
A41	$CH_3SO_2 + O_2$	$\rightarrow$ $CH_3SO_2O_2$	1.2×10^9	[B]
A42	$CH_3SO_2 + CH_3SO_2$	$\rightarrow$ MSIA + CH_3SO_3H	8×10^8	[B]
A43	$CH_3SO_2O_2 + CH_3SO_2^-$	$\rightarrow$ $CH_3SO_3^- + CH_3SO_3$	6.2×10^8	[B]
A44	$CH_3SO_3 + CH_3SO_2^-$	$\rightarrow$ $CH_3SO_3^- + CH_3SO_2$	1×10^8	[B]
A45	CH_3SO_3	$\rightarrow$ SO_3	8.3×10^4	[B]
A46	$CH_3SO_3 + HO_2$	$\rightarrow$ CH_3SO_3H	8.3×10^5	[B]
A47	$CH_2SO_3H + O_2$	$\rightarrow$ $O_2CH_2SO_3H$	2×10^9	[B]
A48	$CH_2SO_3^- + O_2$	$\rightarrow$ $O_2CH_2SO_3^-$	2×10^9	[B]
A49	$O_2CH_2SO_3^-$	$\rightarrow$ $HCHO + SO_3^-$	$[H^+] \times 7 \times 10^3$	[B]

[B] Hoffmann et al. (2016)

S2 Quantum chemical calculations

The schematic potential energy surfaces (PESs) for the reactions of MSIA with OH are shown in Figure S1.1. Two reaction pathways were identified: H-abstraction and OH-addition. For the H-abstraction channel, OH can abstract either the hydrogen atom from the S–OH group or from the methyl group of MSIA. Two transition-state conformations (TS_{abs-1} and TS_{abs-3}) were found for abstraction from the S–OH site, corresponding to different energy barriers, while TS_{abs-2} corresponds to abstraction from the methyl group. The most favourable H-abstraction pathway proceeds via TS_{abs-1}, which is stabilized by a pre-reaction complex involving two hydrogen bonds between MSIA and OH. The calculated barrier height for TS_{abs-1} is 7.1 kcal mol^{-1}. For the OH-addition reaction, a single transition state (TS_{add}) was identified, with a barrier of 5.8 kcal mol^{-1}.

The fate of the OH-addition intermediate IM_{add} (or HOMSIA as reffered to in the main text) was also investigated. Earlier studies suggested that IM_{add} undergoes rapid S–C bond cleavage to form H_2SO_3 and a CH_3 radical (Lv et al., 2019; Gonzalez-García et al., 2007). Our results, however, indicate that IM_{add} can also react with O_2 to produce MSA and HO_2. The calculated unimolecular dissociation rate of IM_{add} is 8.5×10^{10} s^{-1}, while the pseudo-first-order rate constant for the O_2-assisted H-abstraction pathway is 7.3×10^{12} s^{-1} (based on a bimolecular rate constant of 1.47×10^{-6} cm^3 $molecules^{-1}$ s^{-1} and an O_2 concentration of 5×10^{18} molecules cm^{-3}). This additional pathway provides a previously uninvestigated source of MSA formation in the atmosphere.

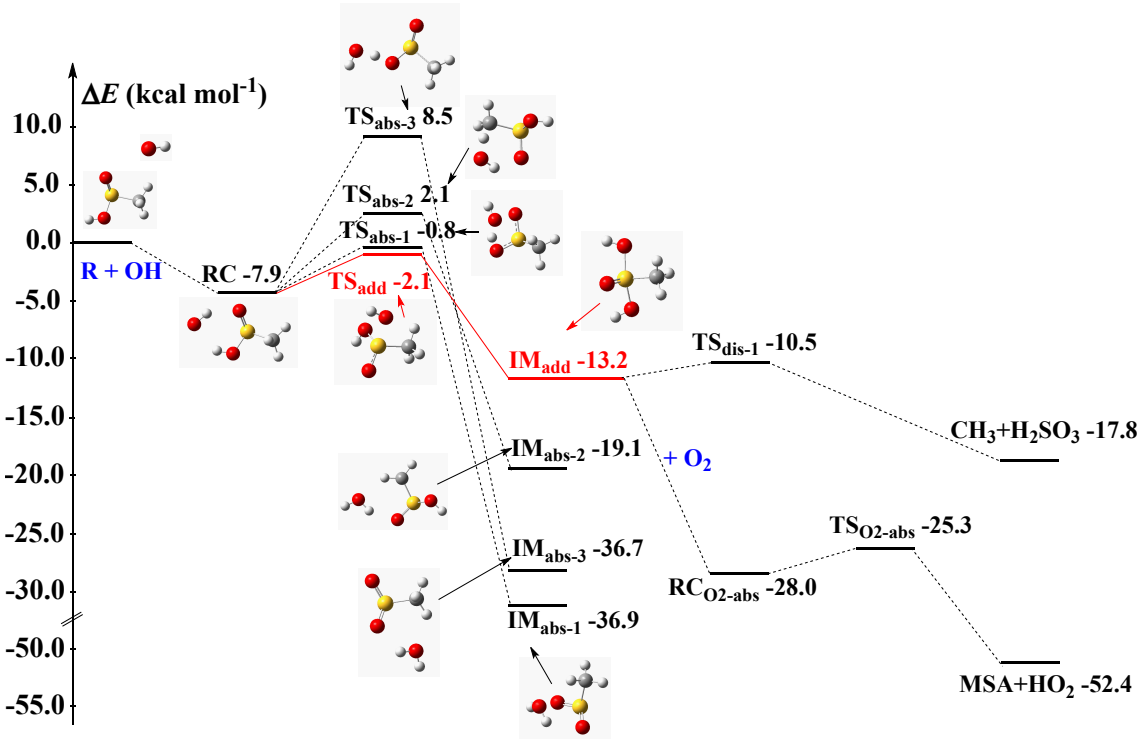

Figure S1. Schematic potential energy surfaces for the reactions of MSIA and OH at the F12a//M06-2X/6-311+G(3df,2p) level of theory.

S3 Additional results from the BaseCase simulation

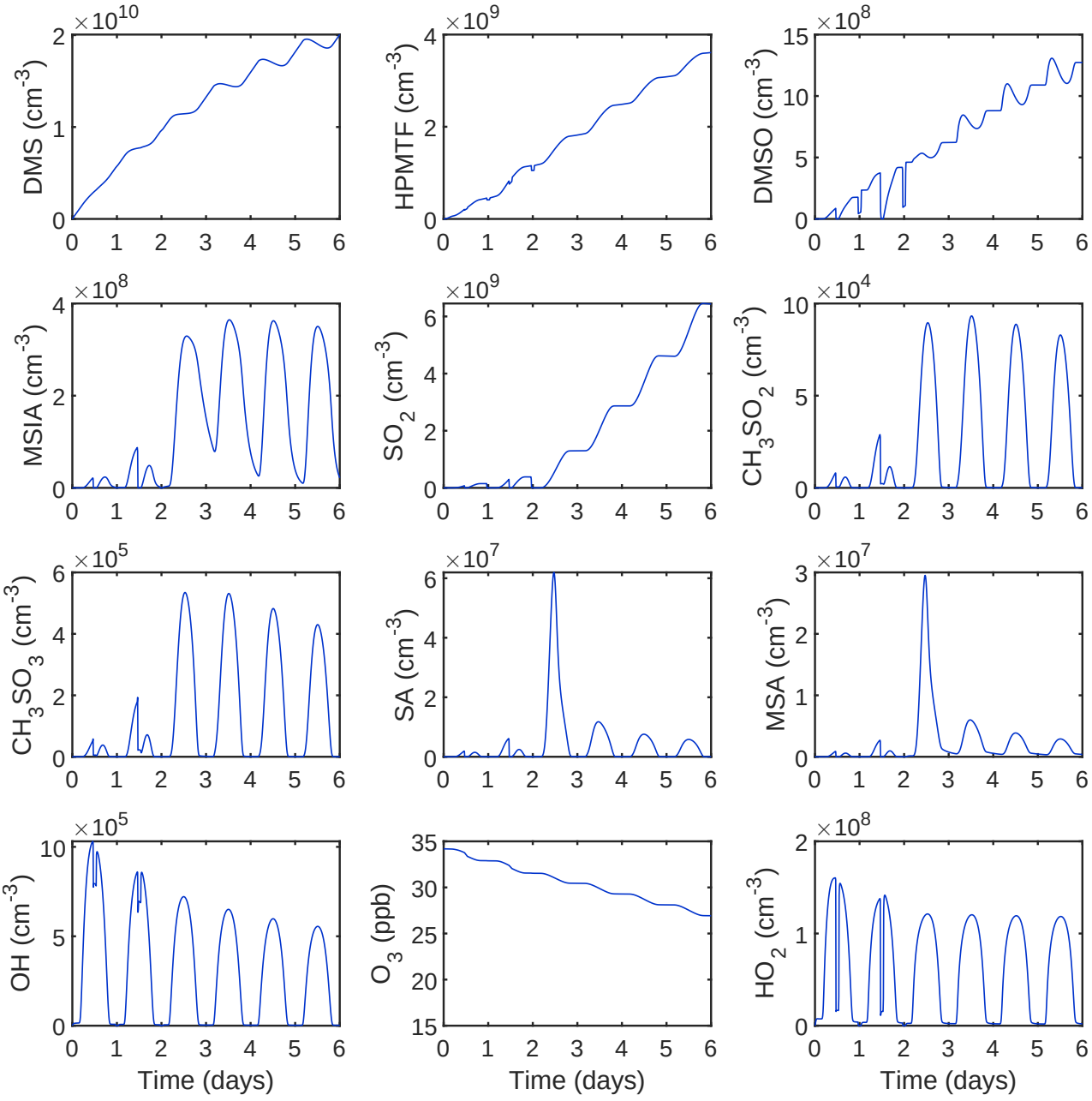

Figure S2. Concentrations of key gas-phase species in the BaseCase Simulation.

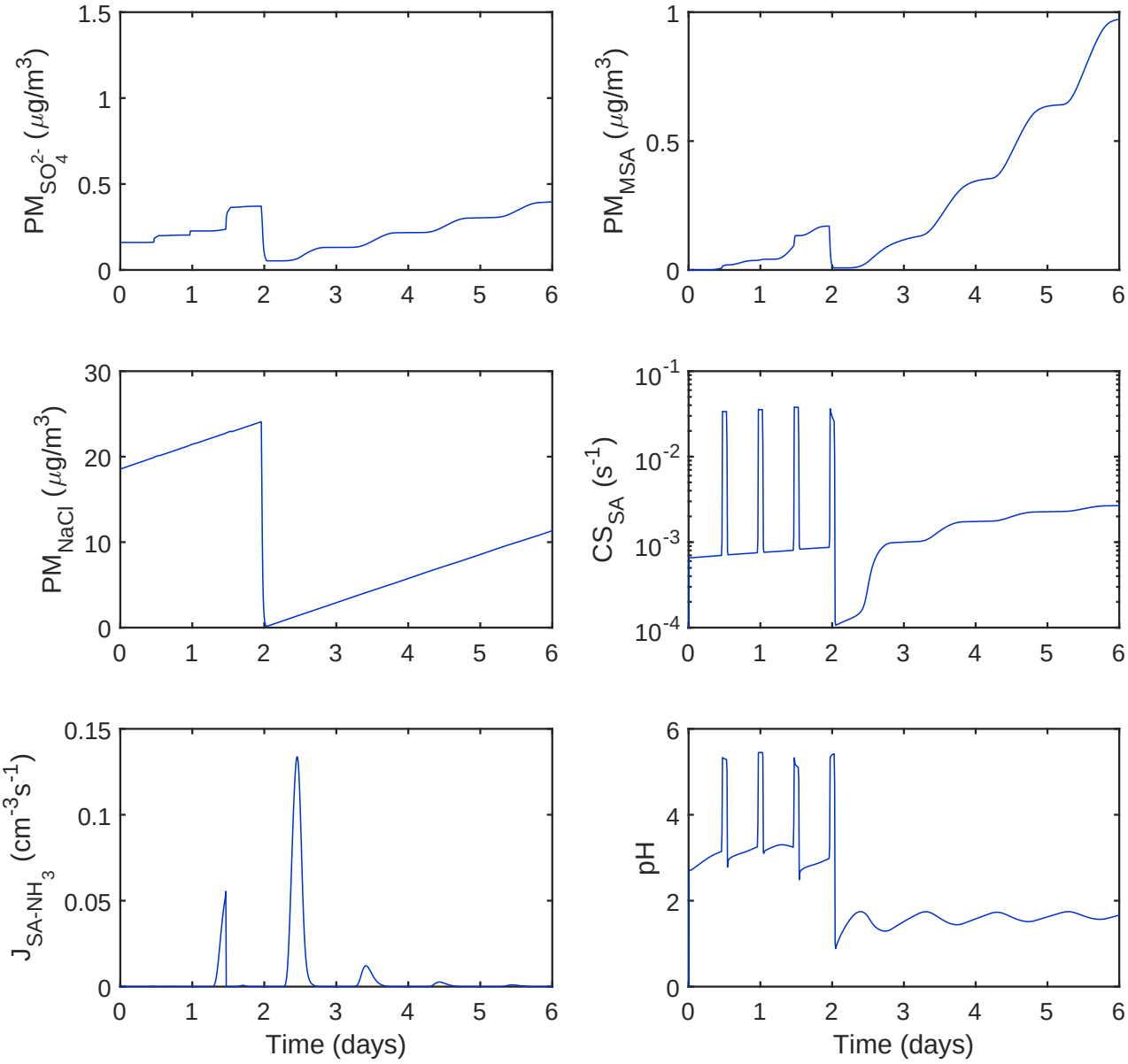

Figure S3. Total SO_4^{2-}, MSA and NaCl PM along with the SA condensation sink, SA-NH_3 driven nucleation rate and bulk pH in the BaseCase Simulation.

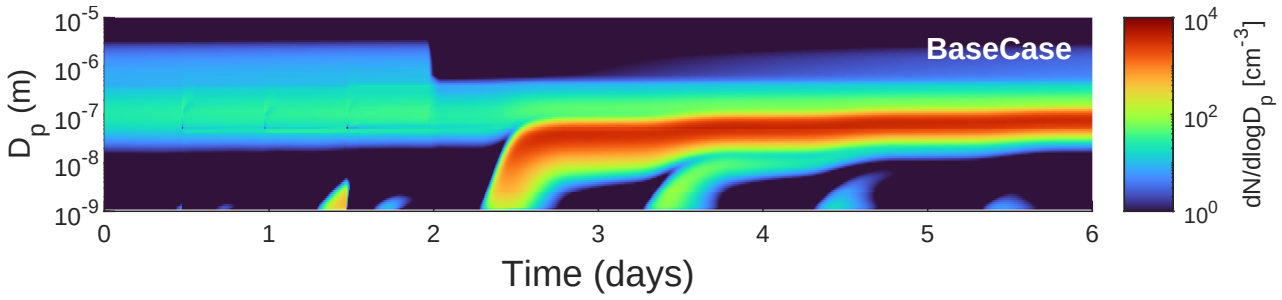

Figure S4. Aerosol particle number size distributions throughout the full simulation period in the BaseCase Simulation.

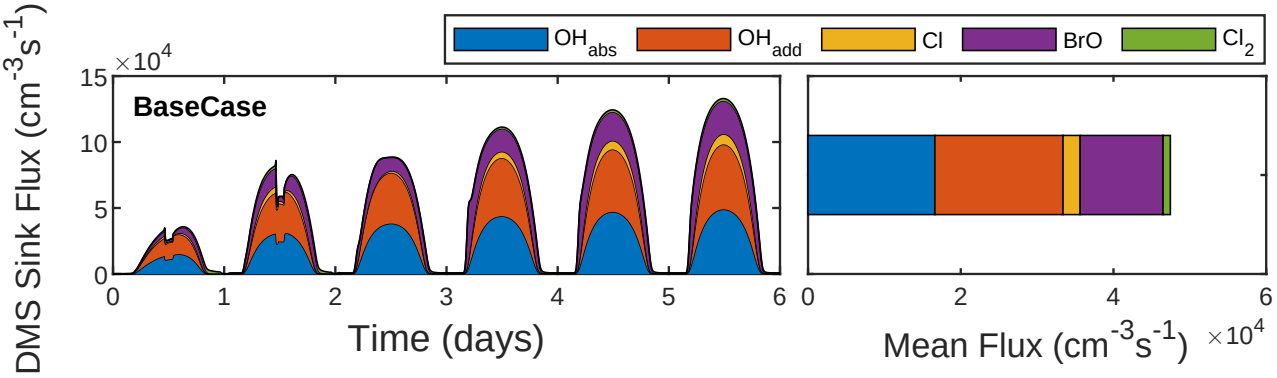

Figure S5. DMS sink flux driven by the reaction with OH (addition), OH (abstraction), Cl, Bro and Cl_2 in the BaseCase Simulation. Reactions that contribute < 1% of the total sink flux are not displayed in the figure.

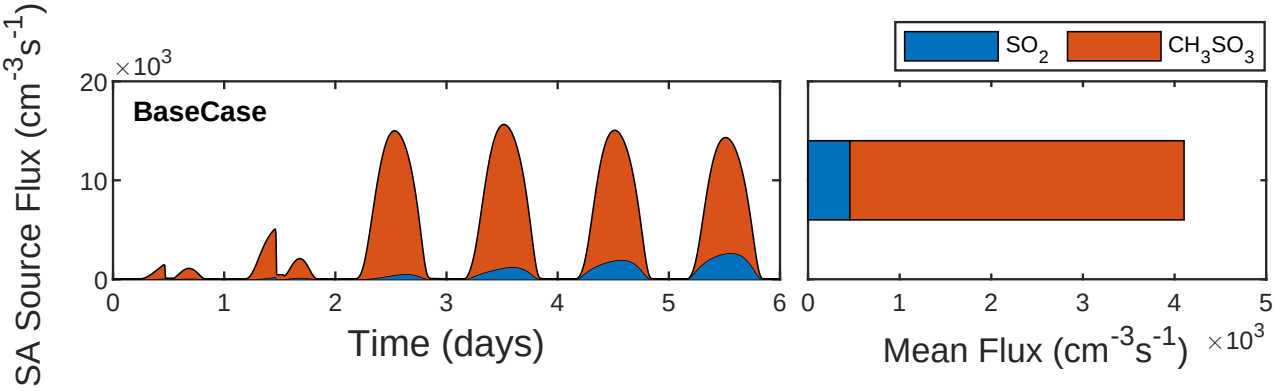

Figure S6. SA source flux from SO_2 and CH_3SO_3 in the BaseCase Simulation.

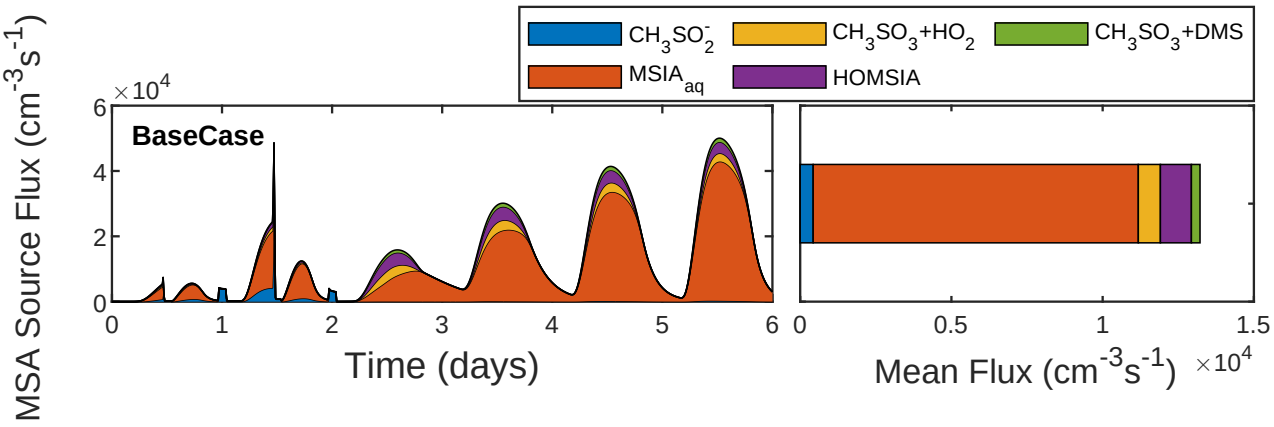

Figure S7. MSA source flux from $CH_3SO_2^-$ and $MSIA_{aq}$ in the aqueous-phase in addition to CH_3SO_3 via HO_2, CH_3SO_3 via DMS and HOMSIA in the gas-phase in the BaseCase Simulation.

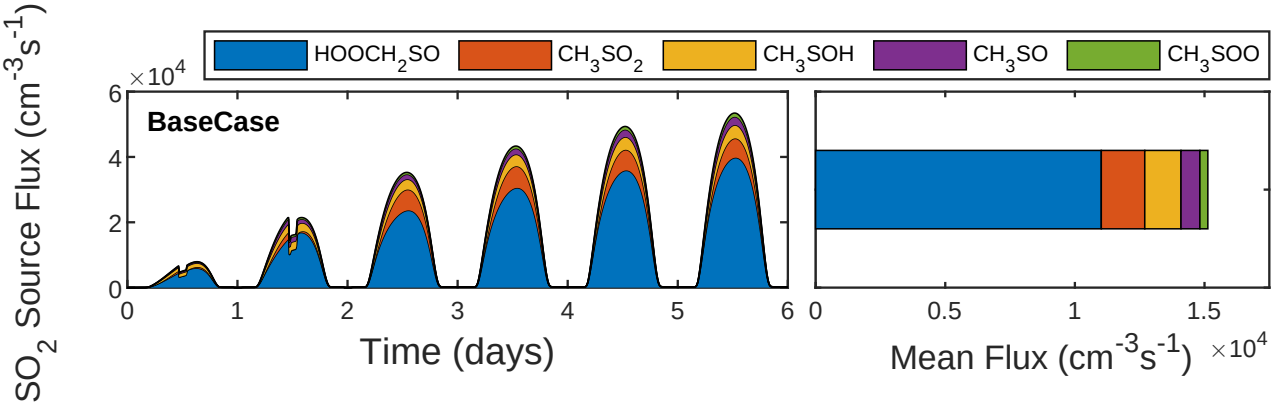

Figure S8. SO_2 source flux from $HOOCH_2SO$, CH_3SO_2, CH_3SOH, CH_3SO and CH_3SOO in the BaseCase Simulation. Reactions that contribute < 1% of the total source flux are not displayed in the figure.

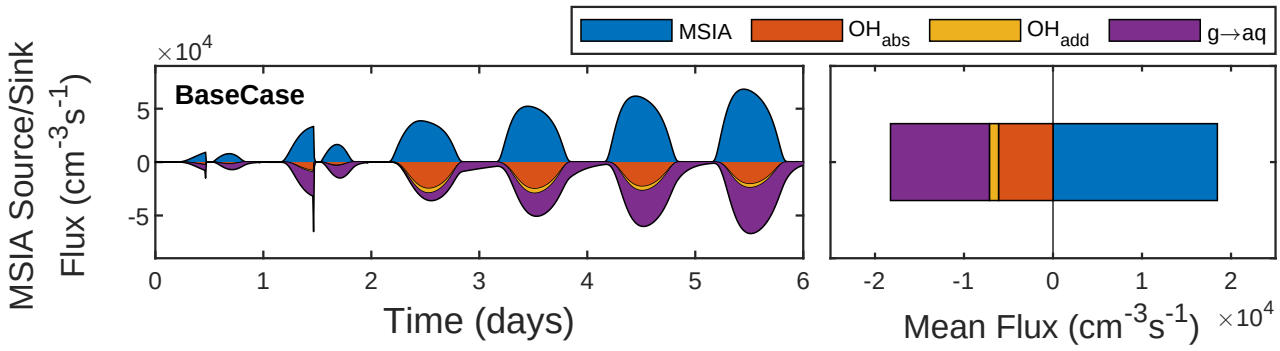

Figure S9. MSIA source/sink flux from DMSO and via reaction with OH (abstraction), OH (addition) and gas-aqueous phase uptake in the BaseCase Simulation. Reactions that contribute < 1% of the total source/sink flux are not displayed in the figure.

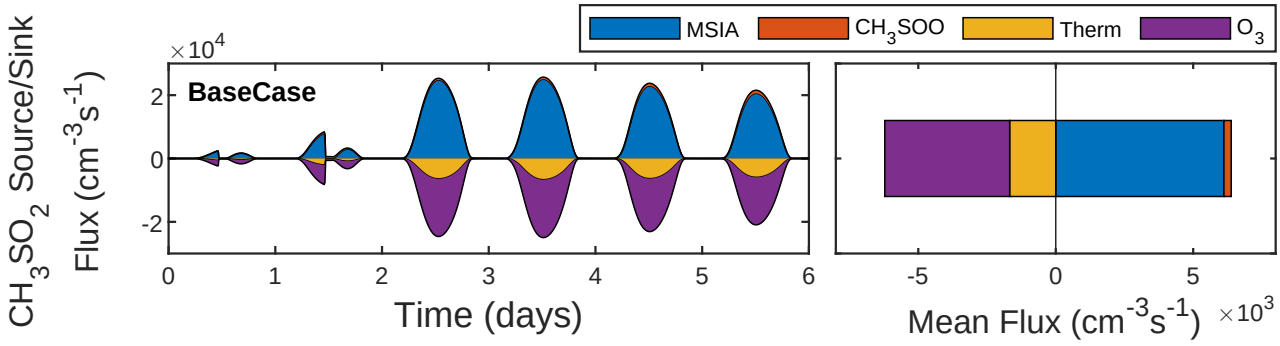

Figure S10. CH_3SO_2 source/sink flux from MSIA, CH_3SOO and via thermal decomposition and reaction with O_3 in the BaseCase Simulation. Reactions that contribute < 1% of the total source/sink flux are not displayed in the figure.

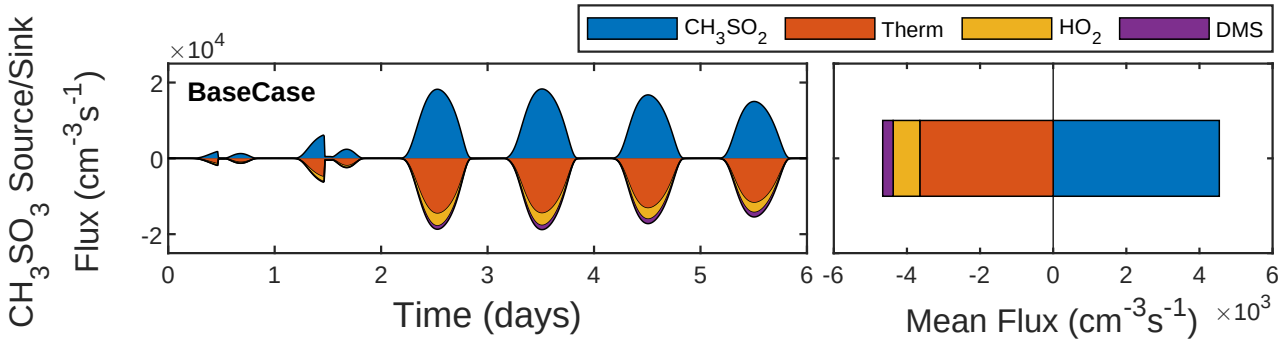

Figure S11. CH_3SO_3 source/sink flux from CH_3SO_2, via thermal decomposition and reaction with HO_2 and DMS in the BaseCase Simulation. Reactions that contribute < 1% of the total source/sink flux are not displayed in the figure.

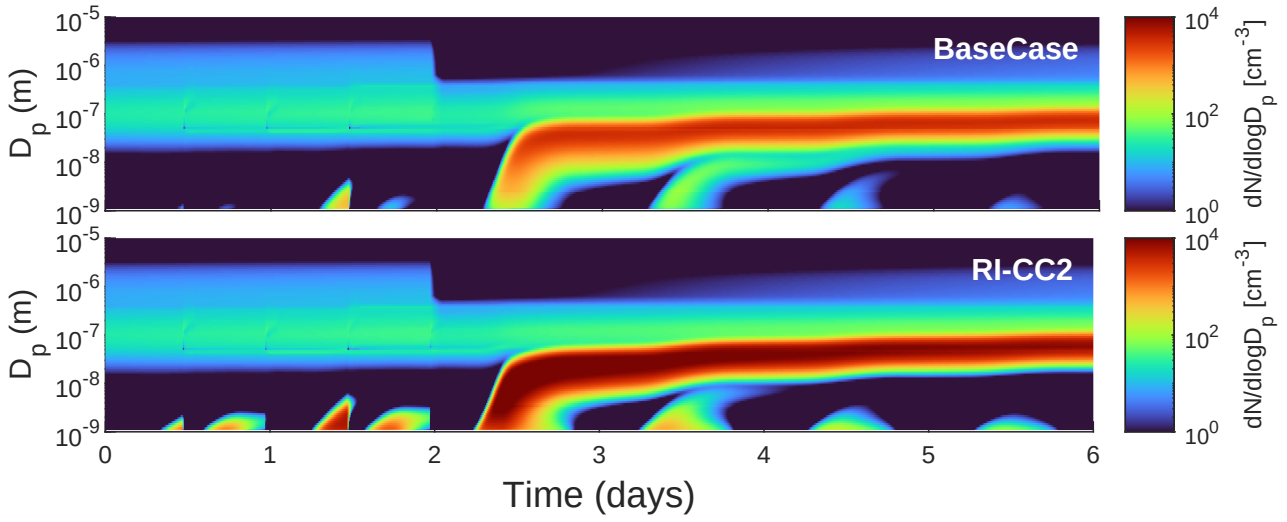

Figure S12. Aerosol particle number size distributions throughout the full simulation period in the BaseCase simulation and a sensitivity run utilizing the RI-CC2 method to calculate the nucleation rate.

S4 Air temperature sensitivity runs

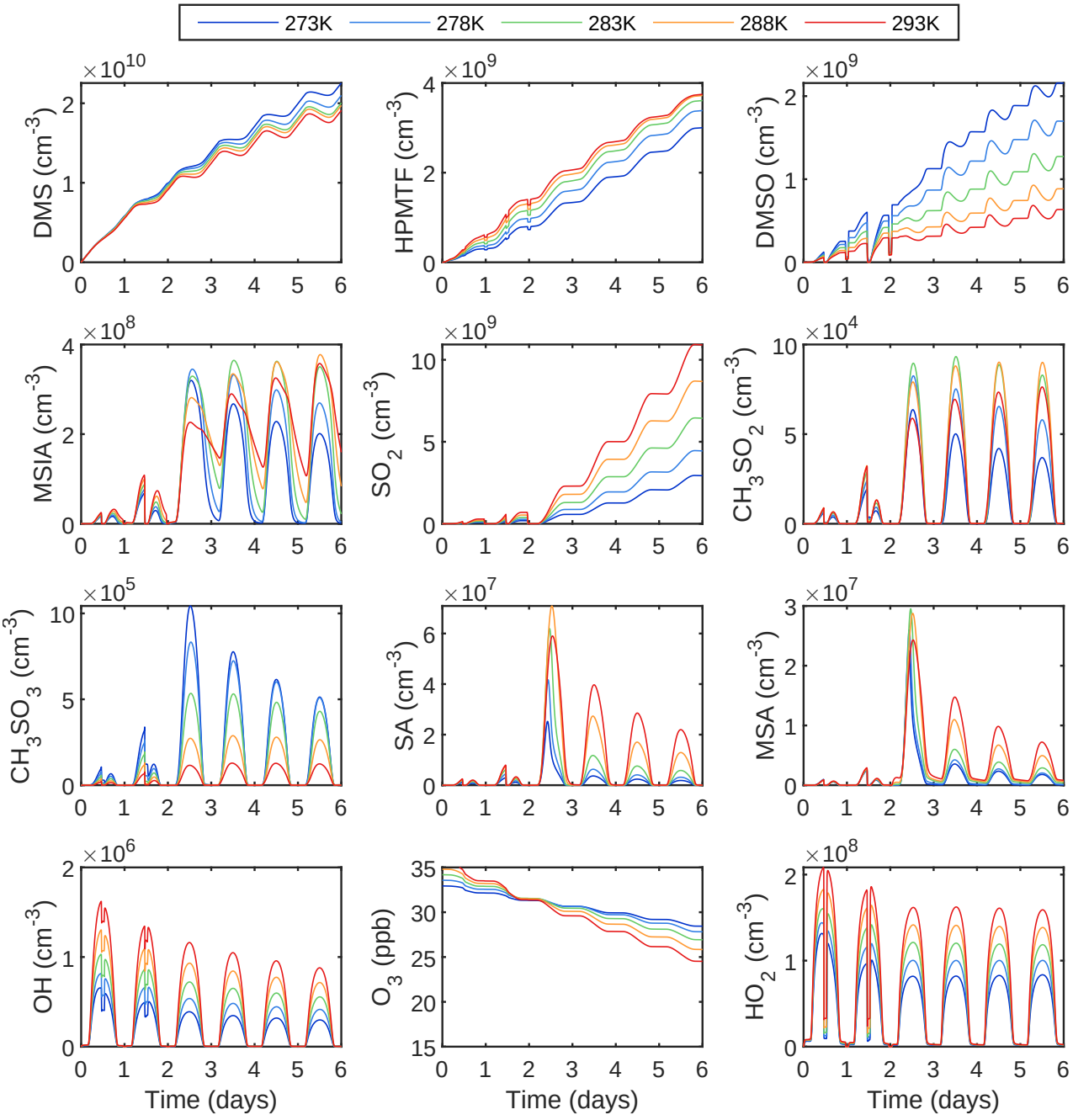

Figure S13. Concentrations of key gas-phase species at varying temperatures ranging from 273K to 293K.

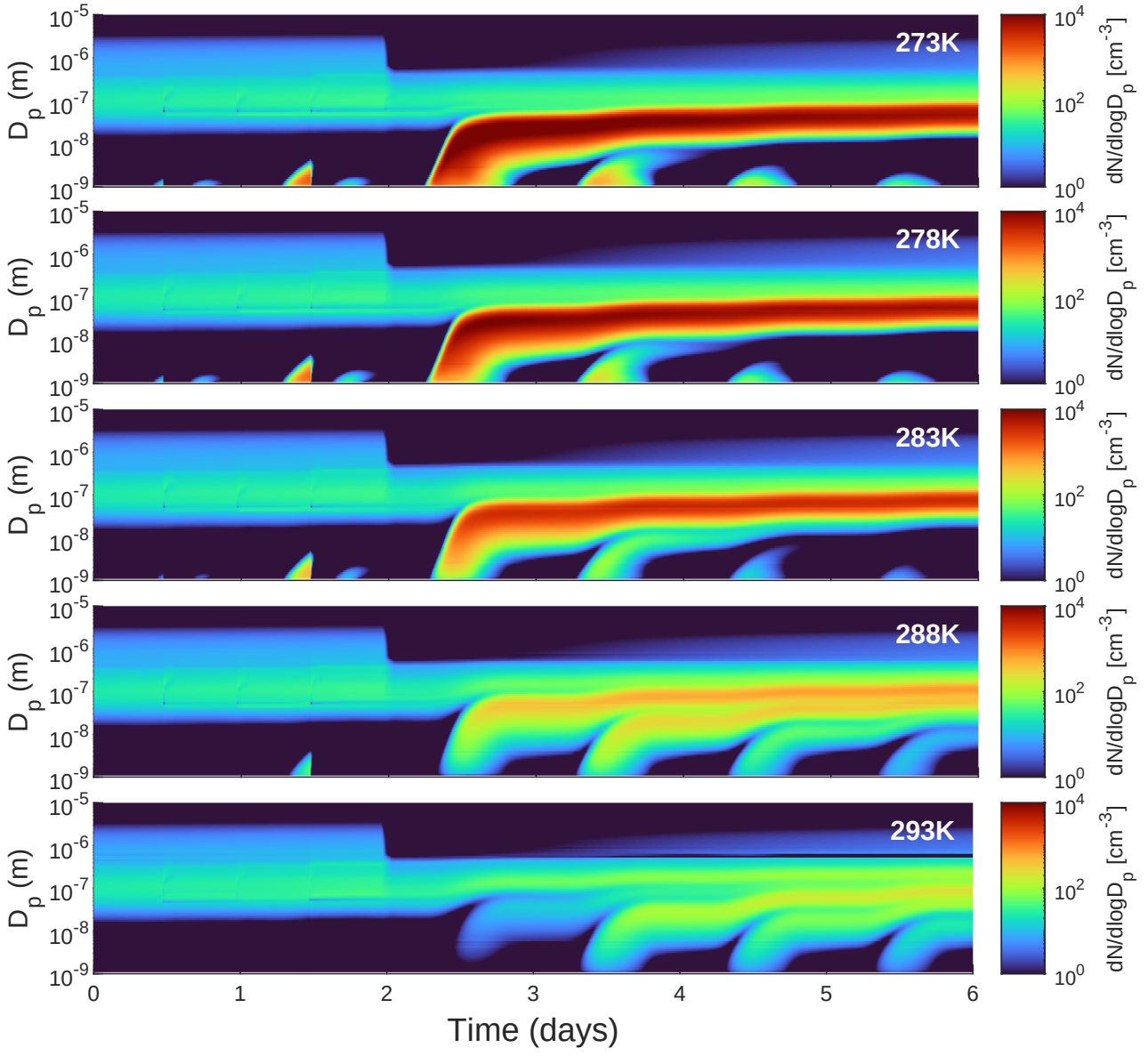

Figure S14. Aerosol particle number size distributions throughout the full simulation period at varying temperatures ranging from 273K to 293K.

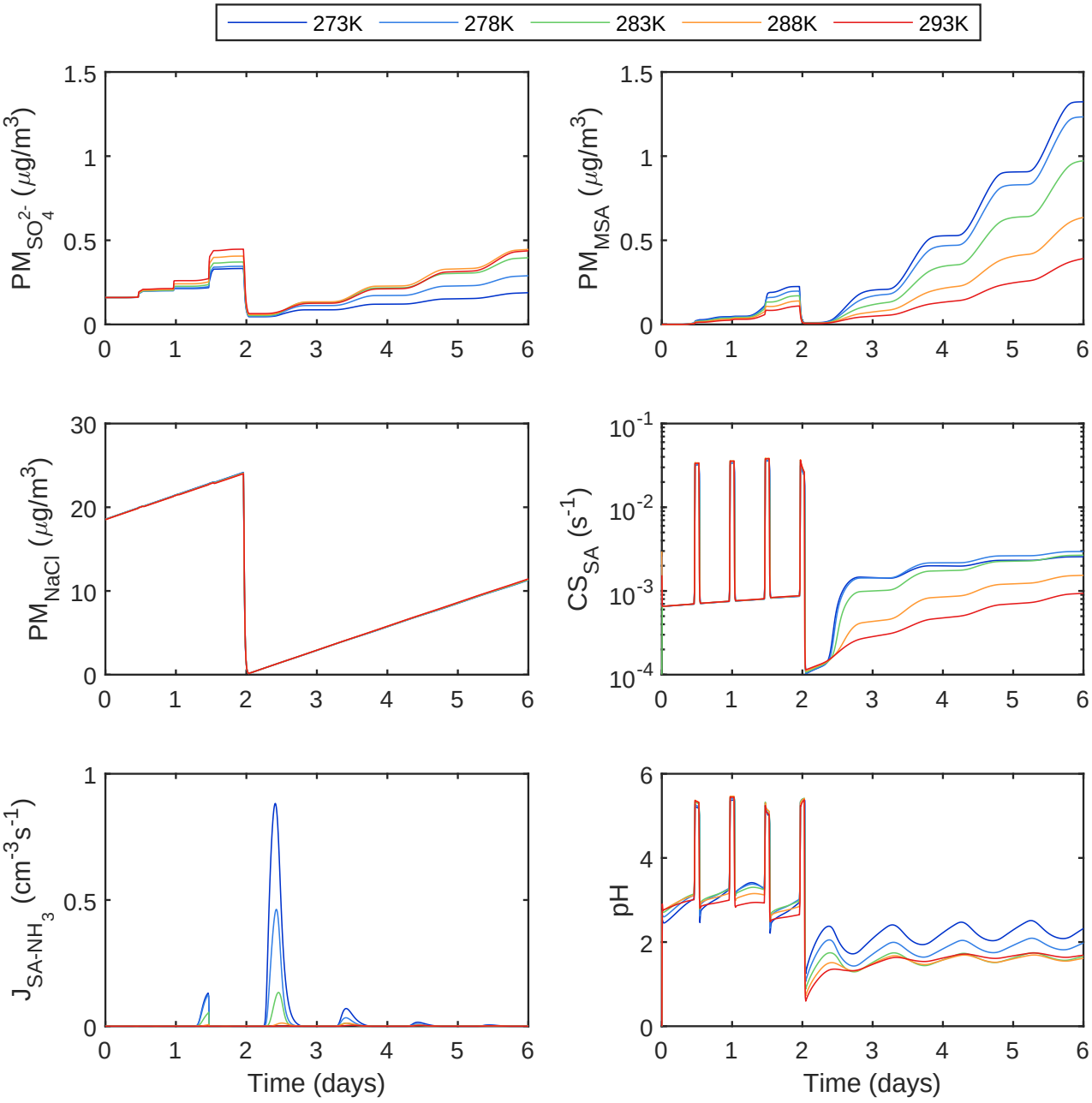

Figure S15. Total SO_4^{2-}, MSA and NaCl PM along with the SA condensation sink, SA-NH_3 driven nucleation rate and bulk pH at varying temperatures ranging from 273K to 293K.

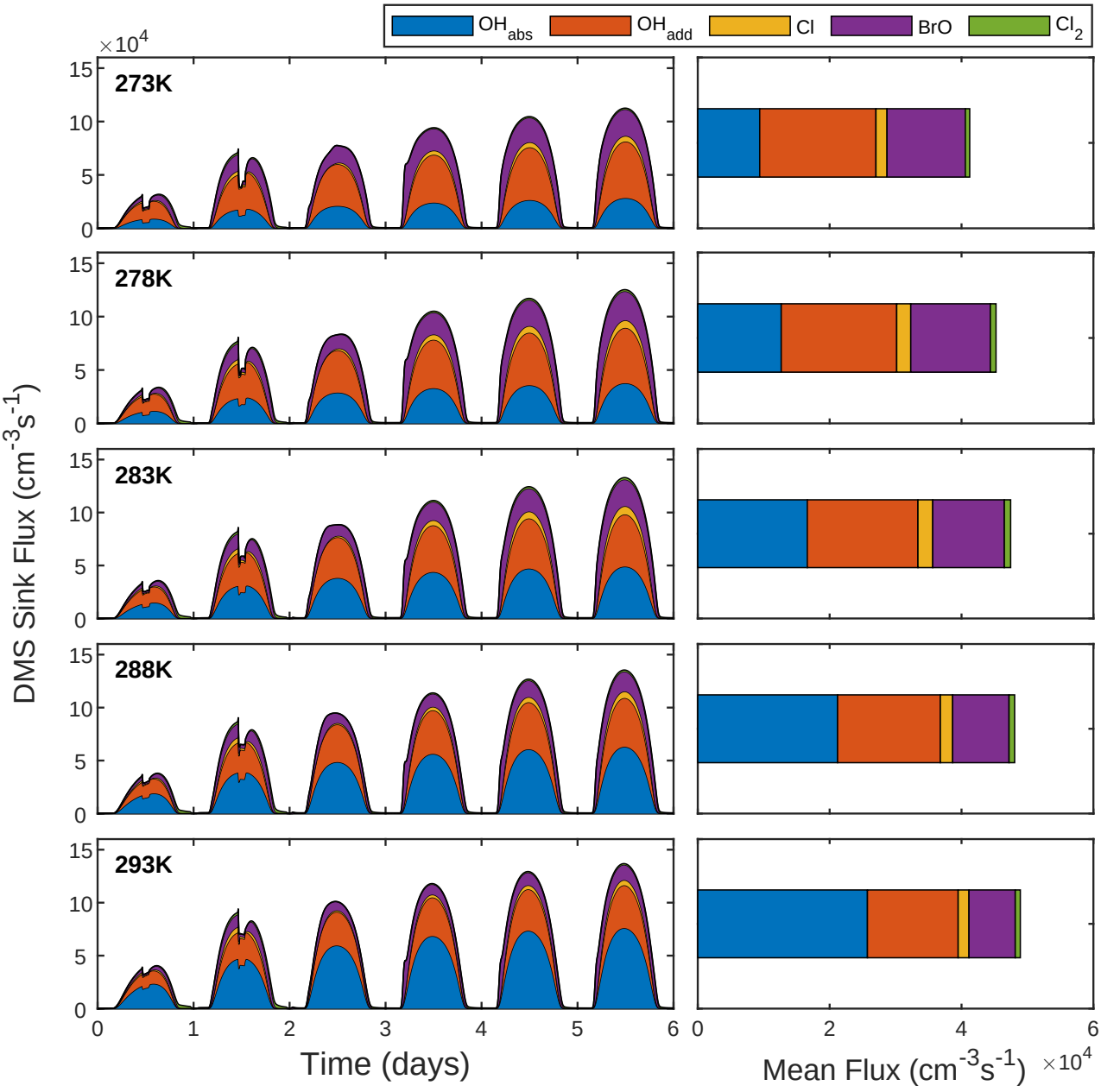

Figure S16. DMS sink flux driven by the reaction with OH (addition), OH (abstraction), Cl, Bro and Cl_2 at varying temperatures ranging from 273K to 293K. Reactions that contribute < 1% of the total sink flux are not displayed in the figure.

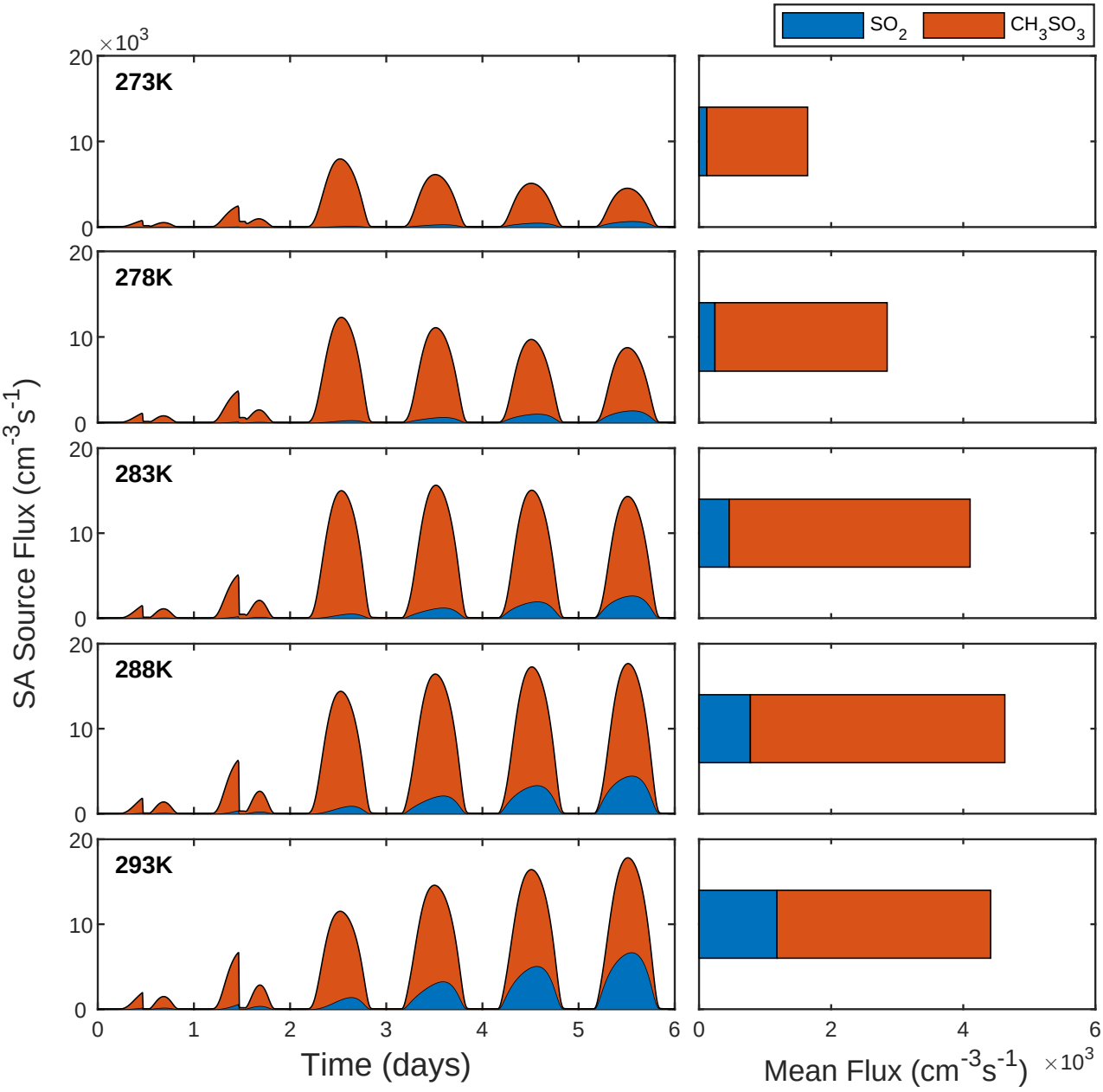

Figure S17. SA source flux from SO_2 and CH_3SO_3 at varying temperatures ranging from 273K to 293K.

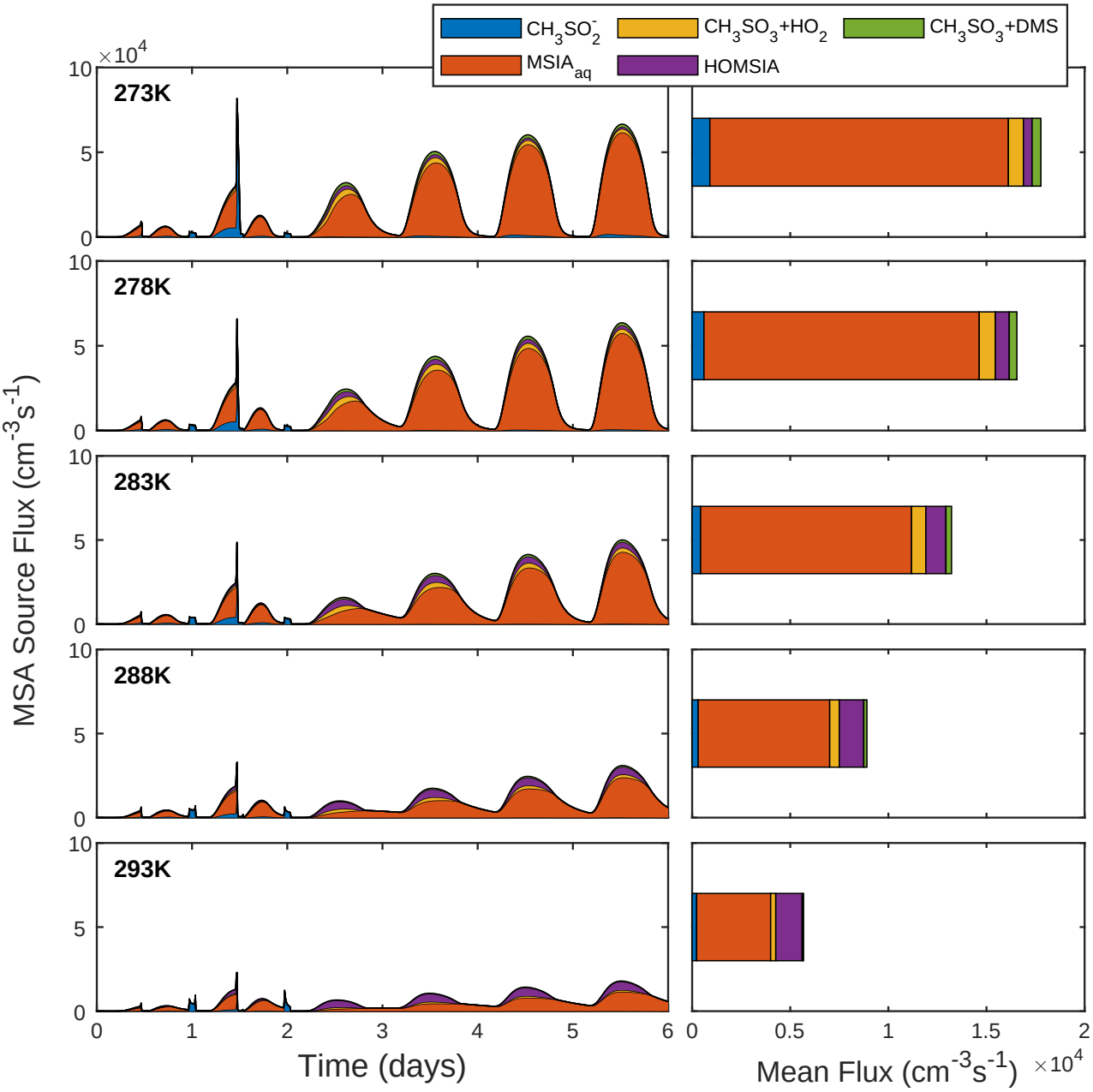

Figure S18. MSA source flux from $CH_3SO_2^-$ and $MSIA_{aq}$ in the aqueous-phase in addition to CH_3SO_3 via HO_2, CH_3SO_3 via DMS and HOMSIA in the gas-phase at varying temperatures ranging from 273K to 293K.

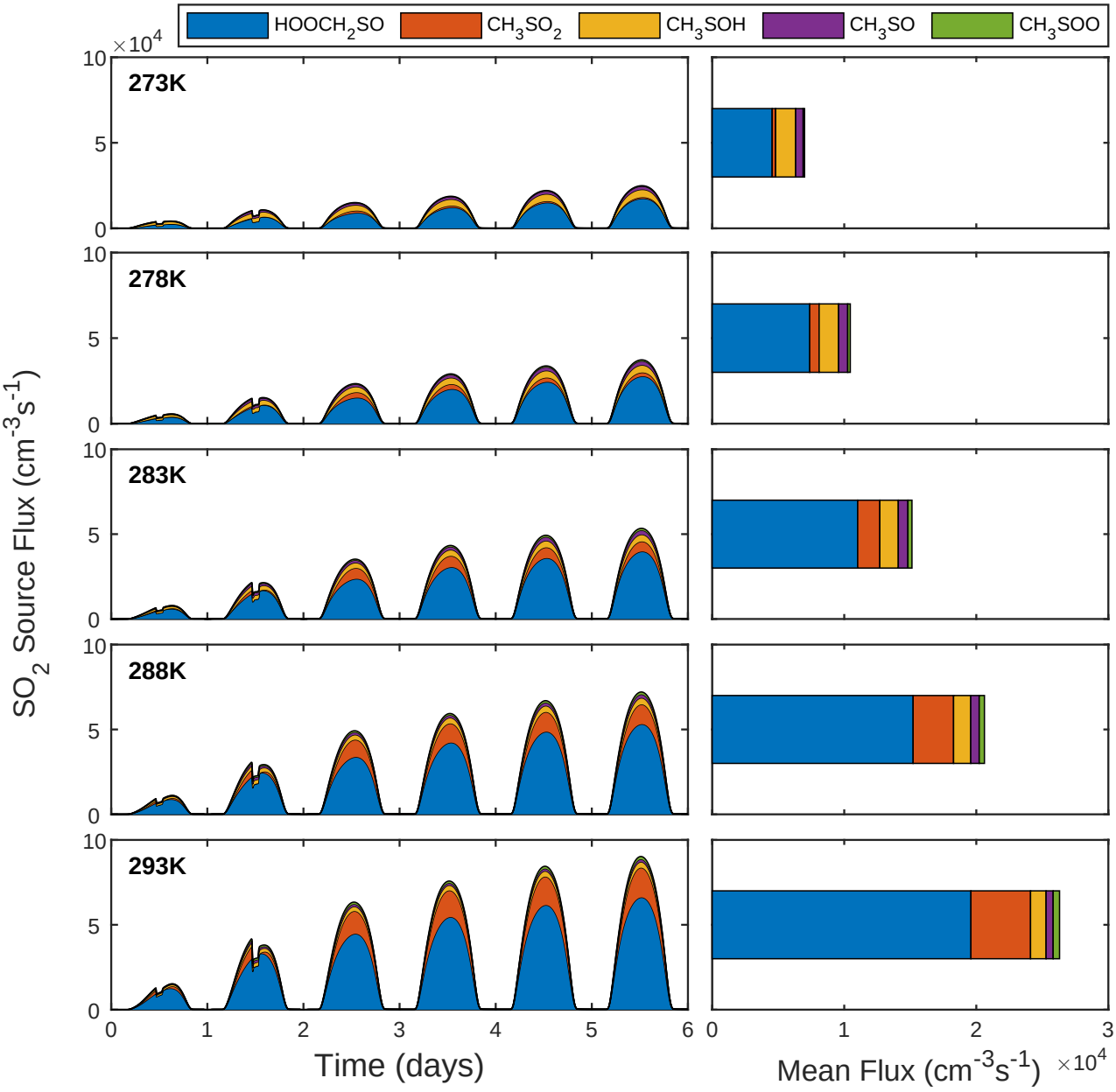

Figure S19. SO_2 source flux from $HOOCH_2SO$, CH_3SO_2, CH_3SOH, CH_3SO and CH_3SOO at varying temperatures ranging from 273K to 293K. Reactions that contribute < 1% of the total source flux are not displayed in the figure.

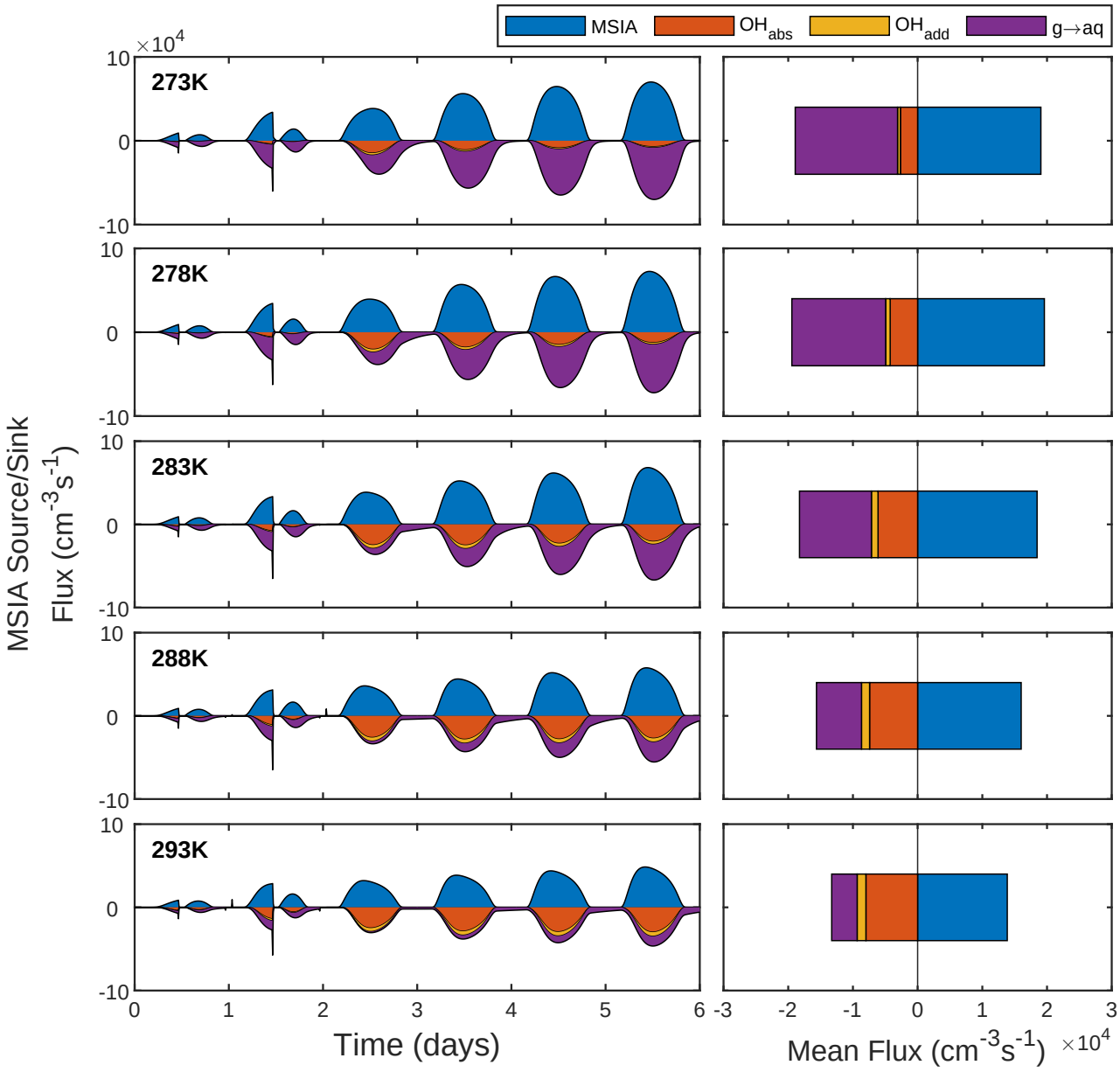

Figure S20. MSIA source/sink flux from DMSO and via reaction with OH (abstraction), OH (addition) and gas-aqueous phase uptake at varying temperatures ranging from 273K to 293K. Reactions that contribute < 1% of the total source/sink flux are not displayed in the figure.

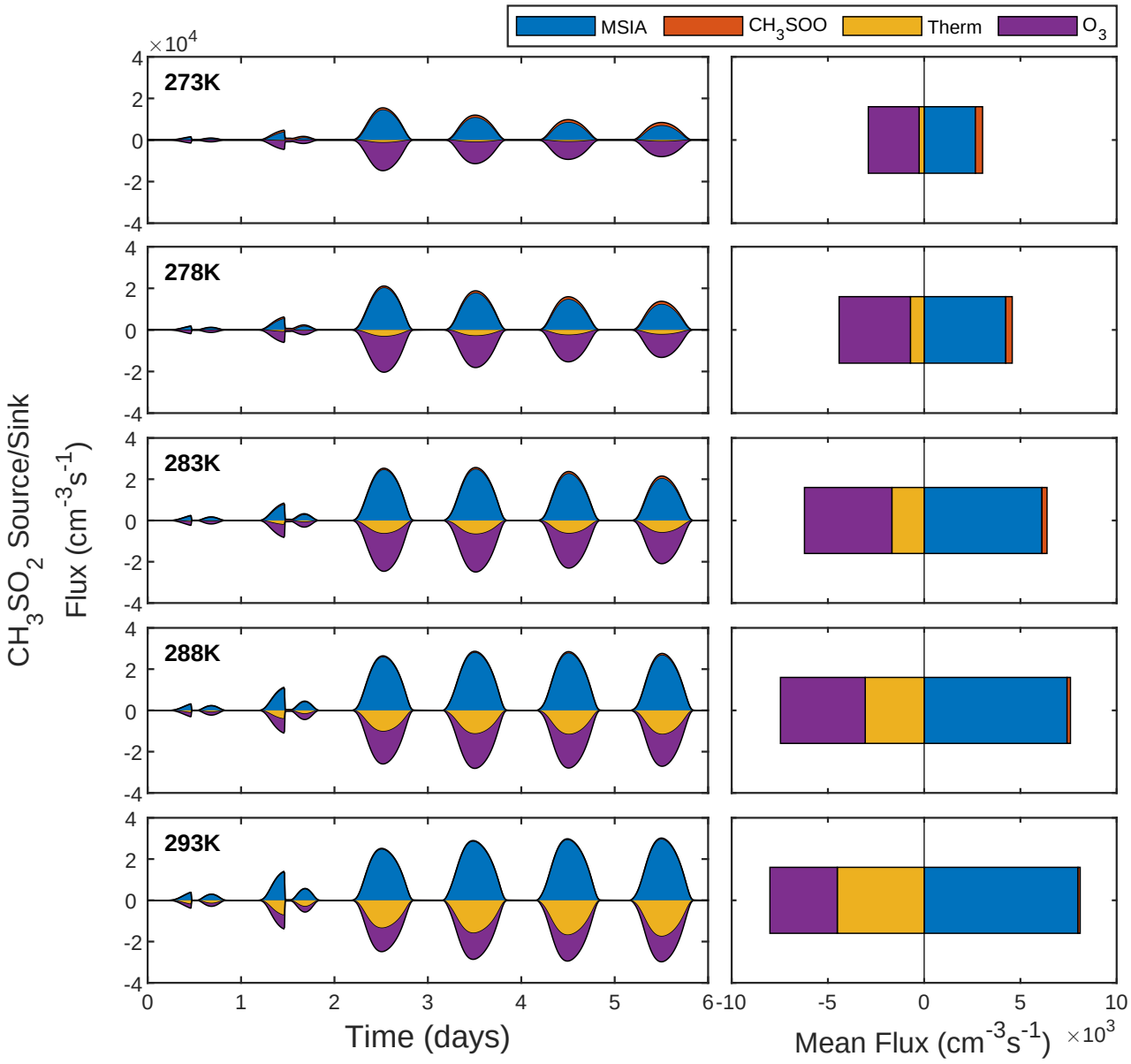

Figure S21. CH_3SO_2 source/sink flux from MSIA, CH_3SOO and via thermal decomposition and reaction with O_3 at varying temperatures ranging from 273K to 293K. Reactions that contribute < 1% of the total source/sink flux are not displayed in the figure.

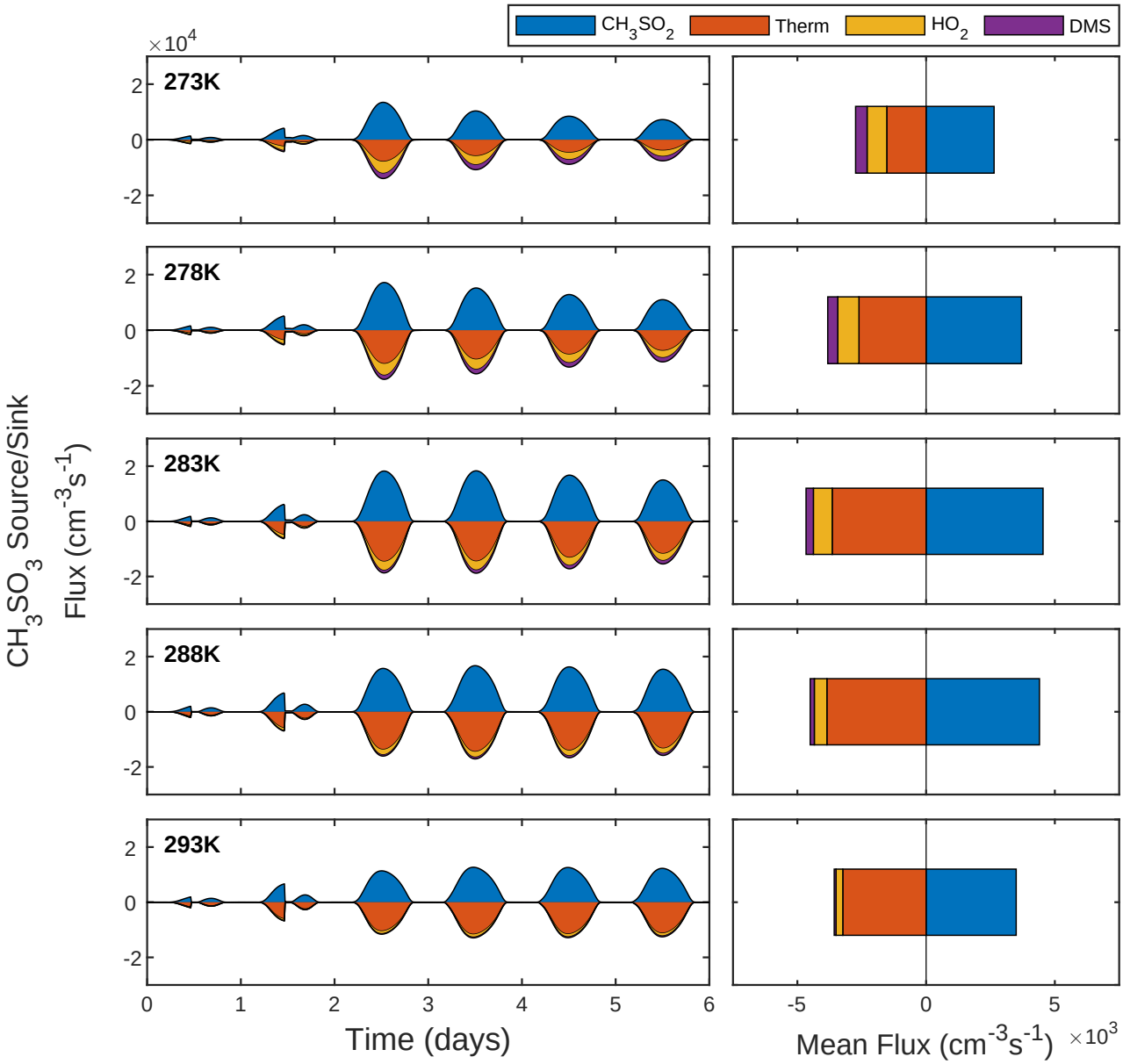

Figure S22. CH_3SO_3 source/sink flux from CH_3SO_2, via thermal decomposition and reaction with HO_2 and DMS at varying temperatures ranging from 273K to 293K. Reactions that contribute < 1% of the total source/sink flux are not displayed in the figure.

S5 Wind-speed sensitivity runs

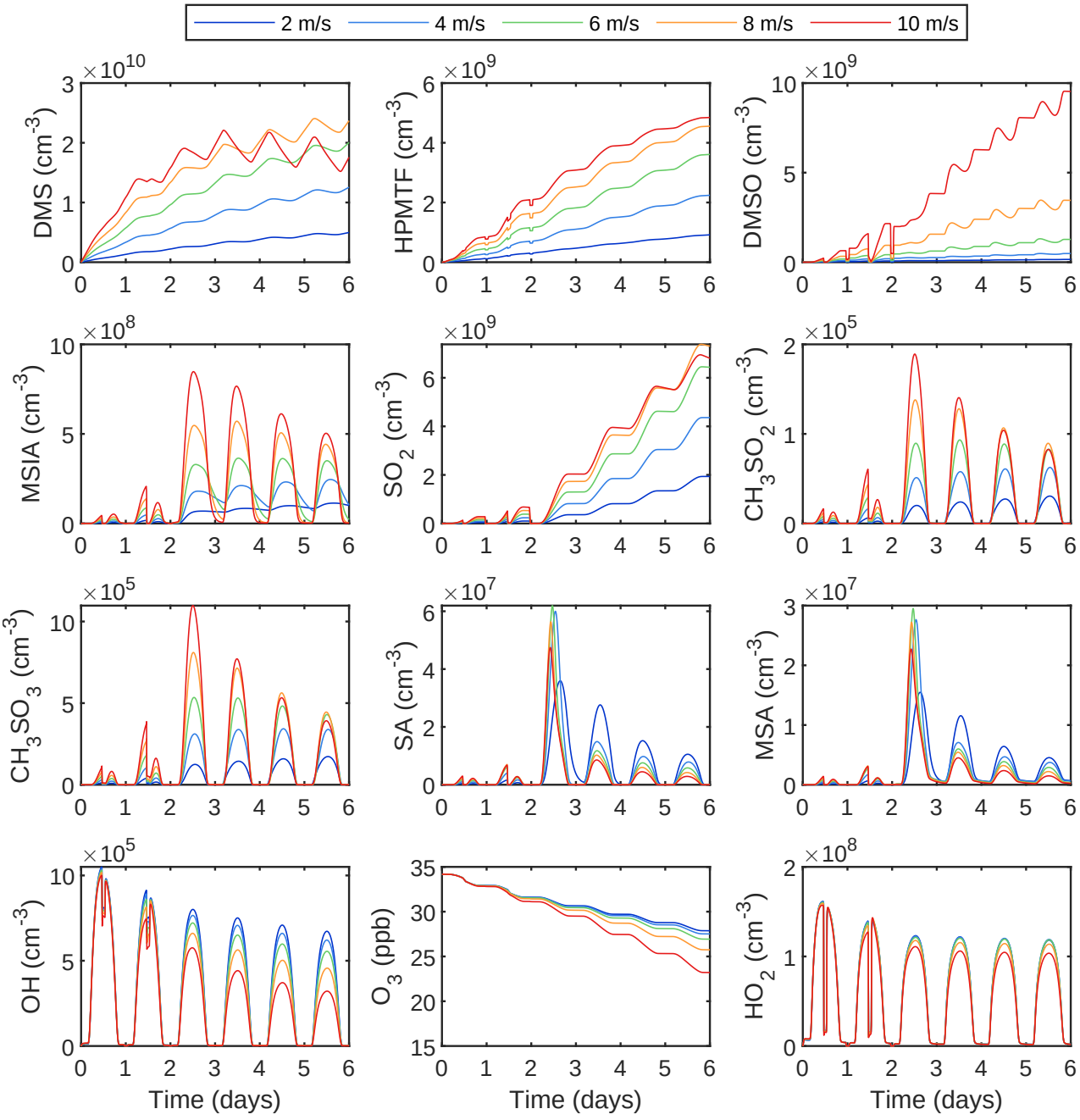

Figure S23. Concentrations of key gas-phase species at varying wind-speeds ranging from 2 $\mathrm{m/s}$ to 10 $\mathrm{m/s}$.

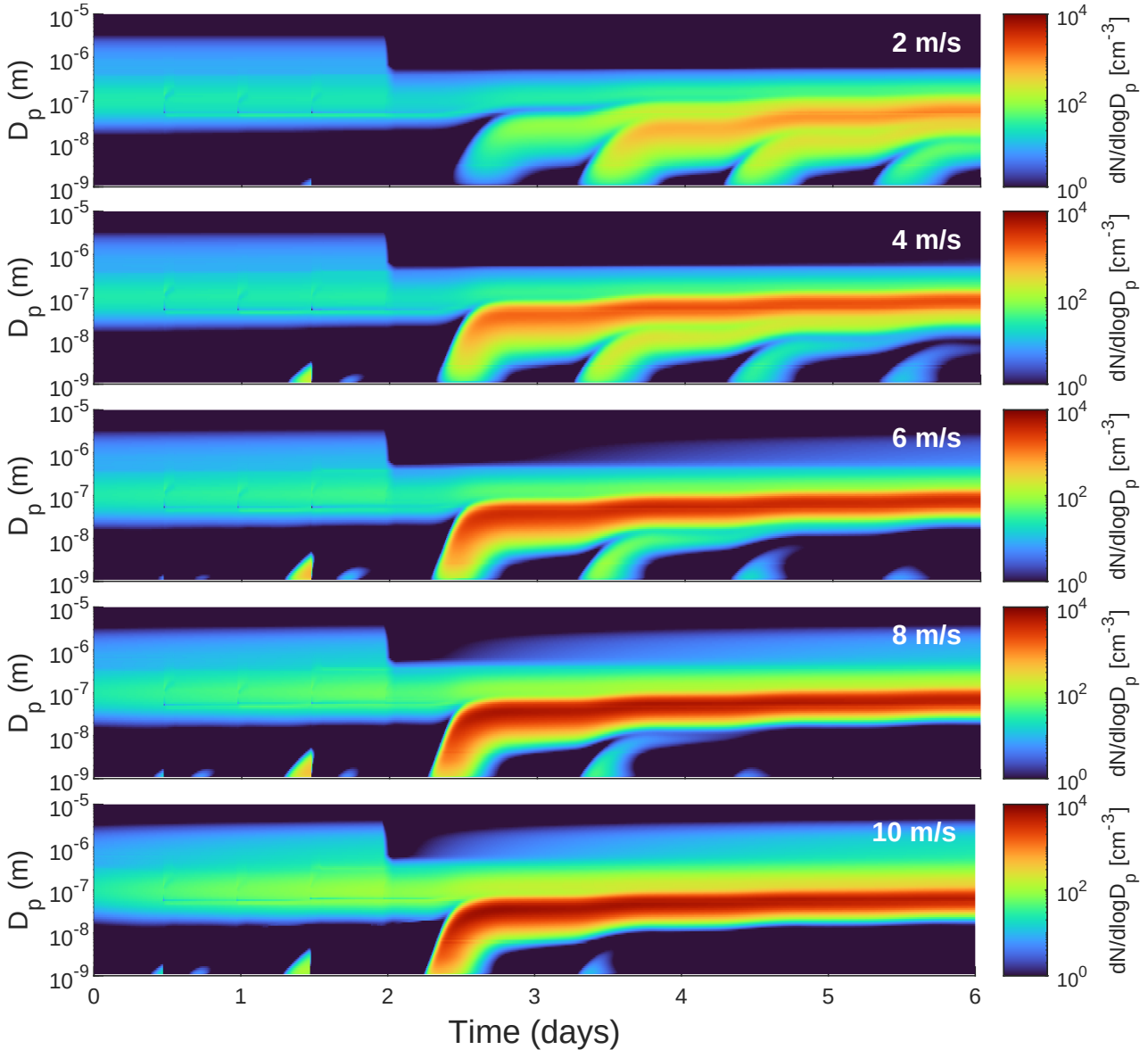

Figure S24. Aerosol particle number size distributions throughout the full simulation period at varying wind-speeds ranging from 2 $\mathrm{m/s}$ to 10 $\mathrm{m/s}$.

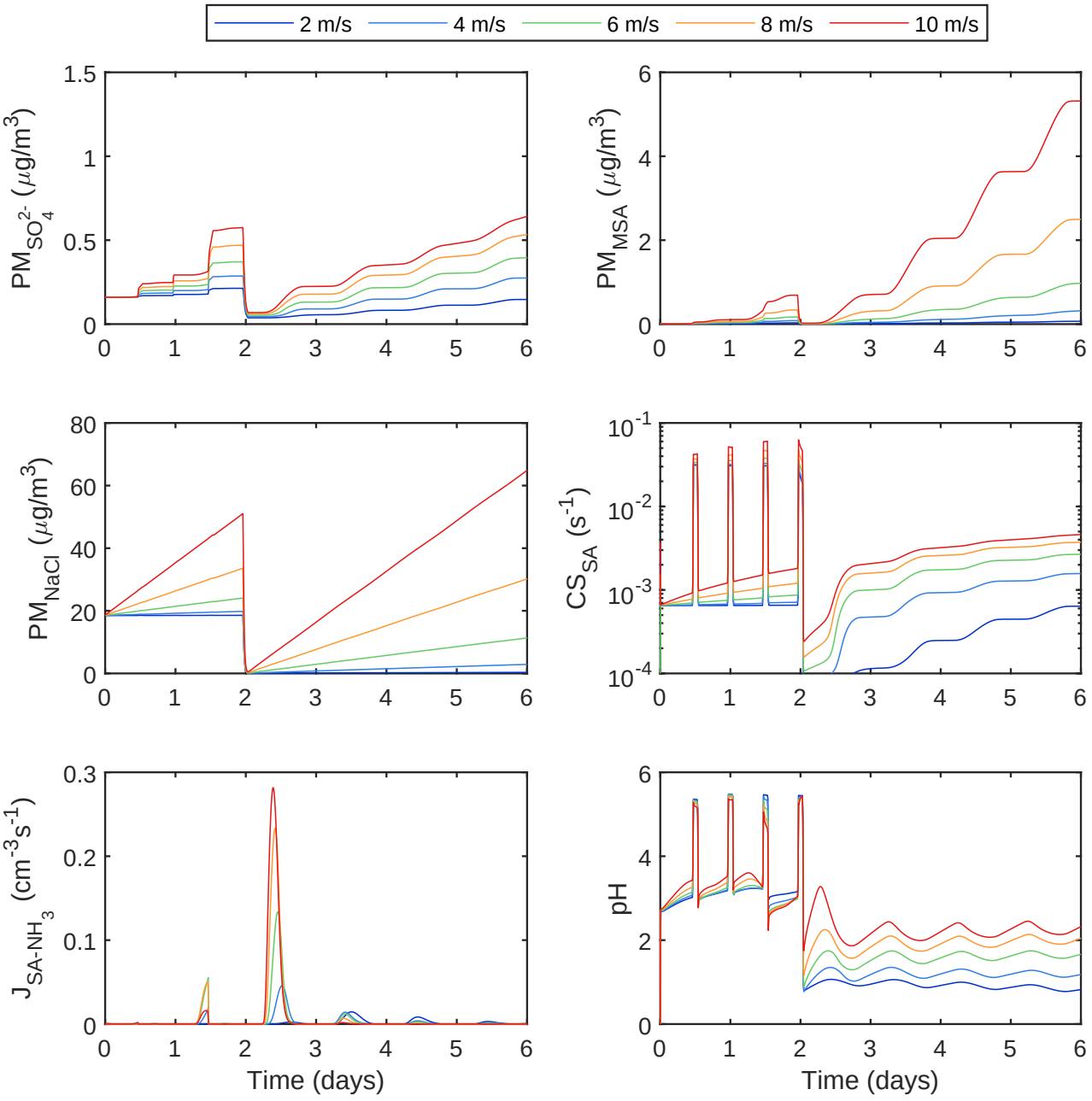

Figure S25. Total SO_4^{2-}, MSA and NaCl PM along with the SA condensation sink, SA-NH_3 driven nucleation rate and bulk pH at varying wind-speeds ranging from 2 m/s to 10 m/s.

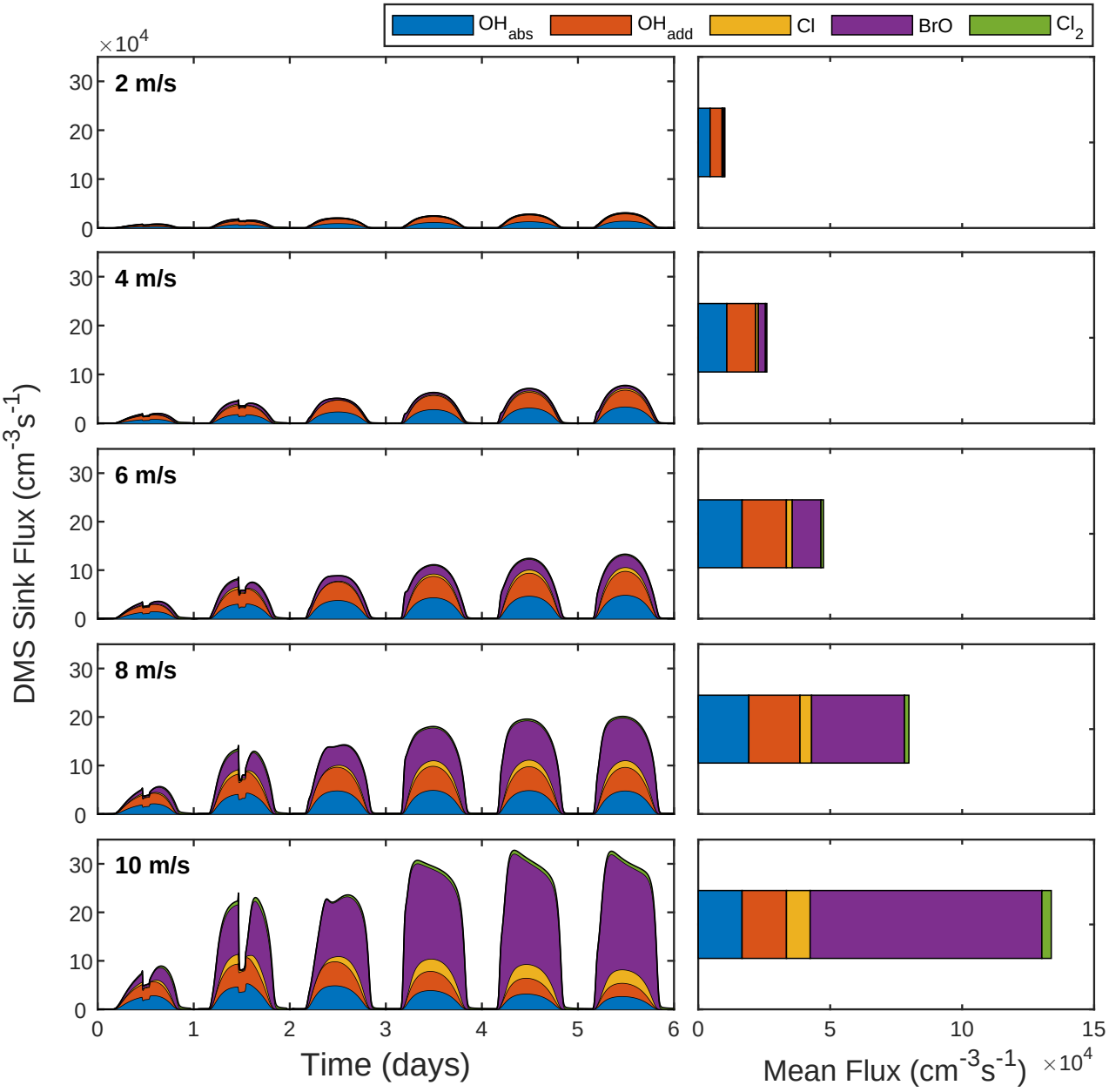

Figure S26. DMS sink flux driven by the reaction with OH (addition), OH (abstraction), Cl, Bro and Cl_2 at varying wind-speeds ranging from 2 $\mathrm{m/s}$ to 10 $\mathrm{m/s}$. Reactions that contribute < 1% of the total sink flux are not displayed in the figure.

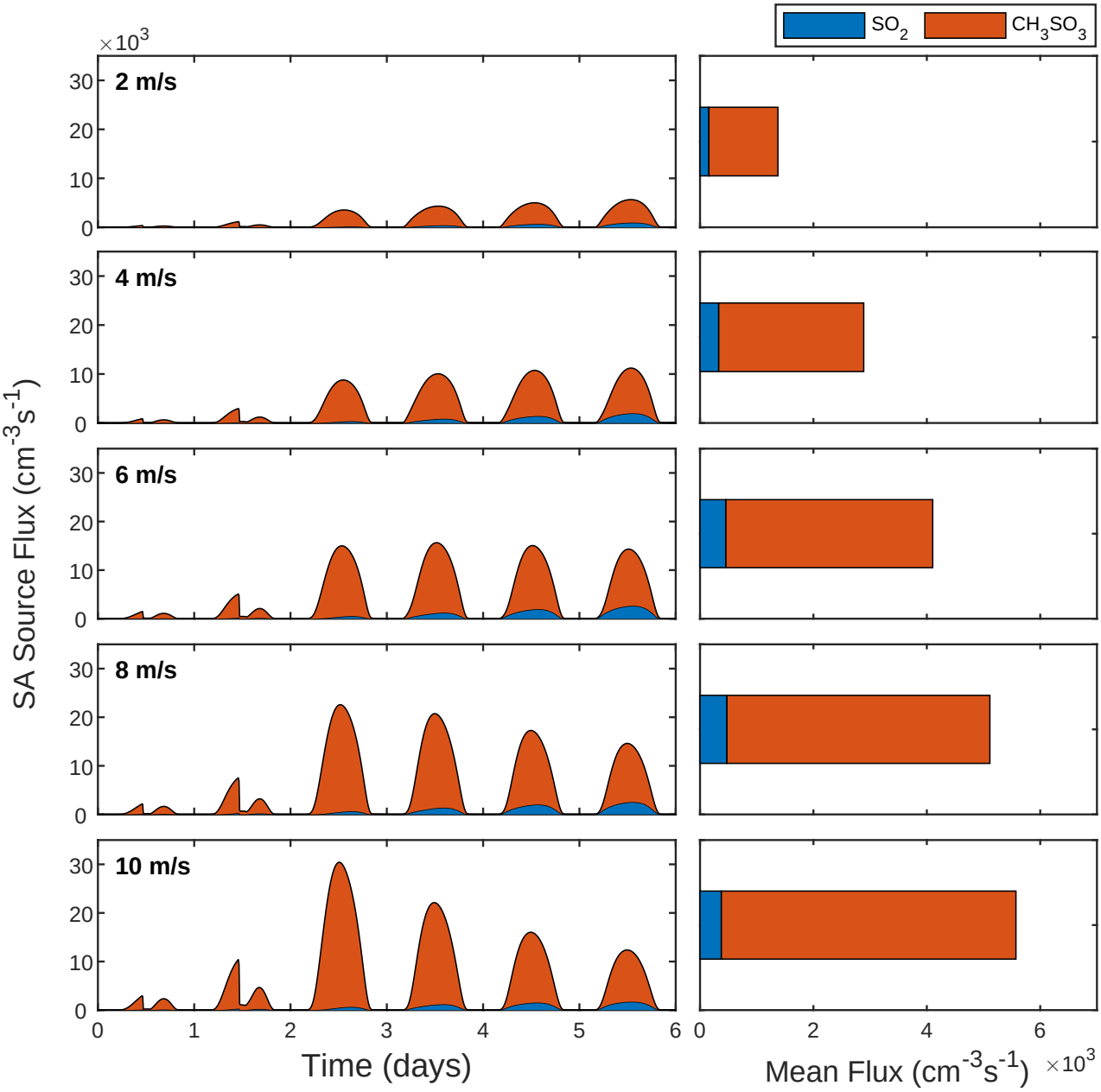

Figure S27. SA source flux from SO_2 and CH_3SO_3 at varying wind-speeds ranging from 2 m/s to 10 m/s.

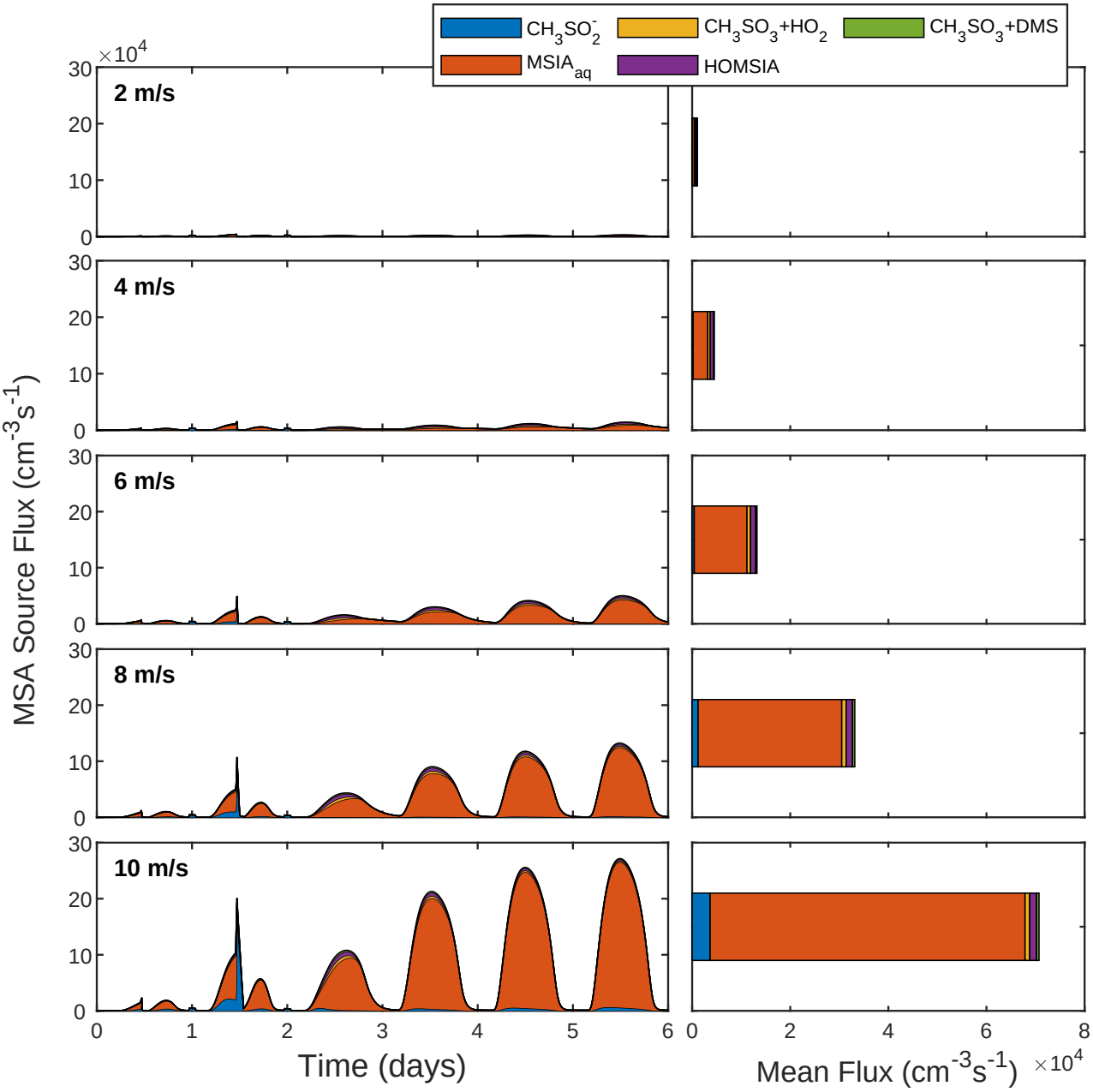

Figure S28. MSA source flux from $CH_3SO_2^-$ and $MSIA_{aq}$ in the aqueous-phase in addition to CH_3SO_3 via HO_2, CH_3SO_3 via DMS and HOMSIA in the gas-phase at varying wind-speeds ranging from 2 m/s to 10 m/s.

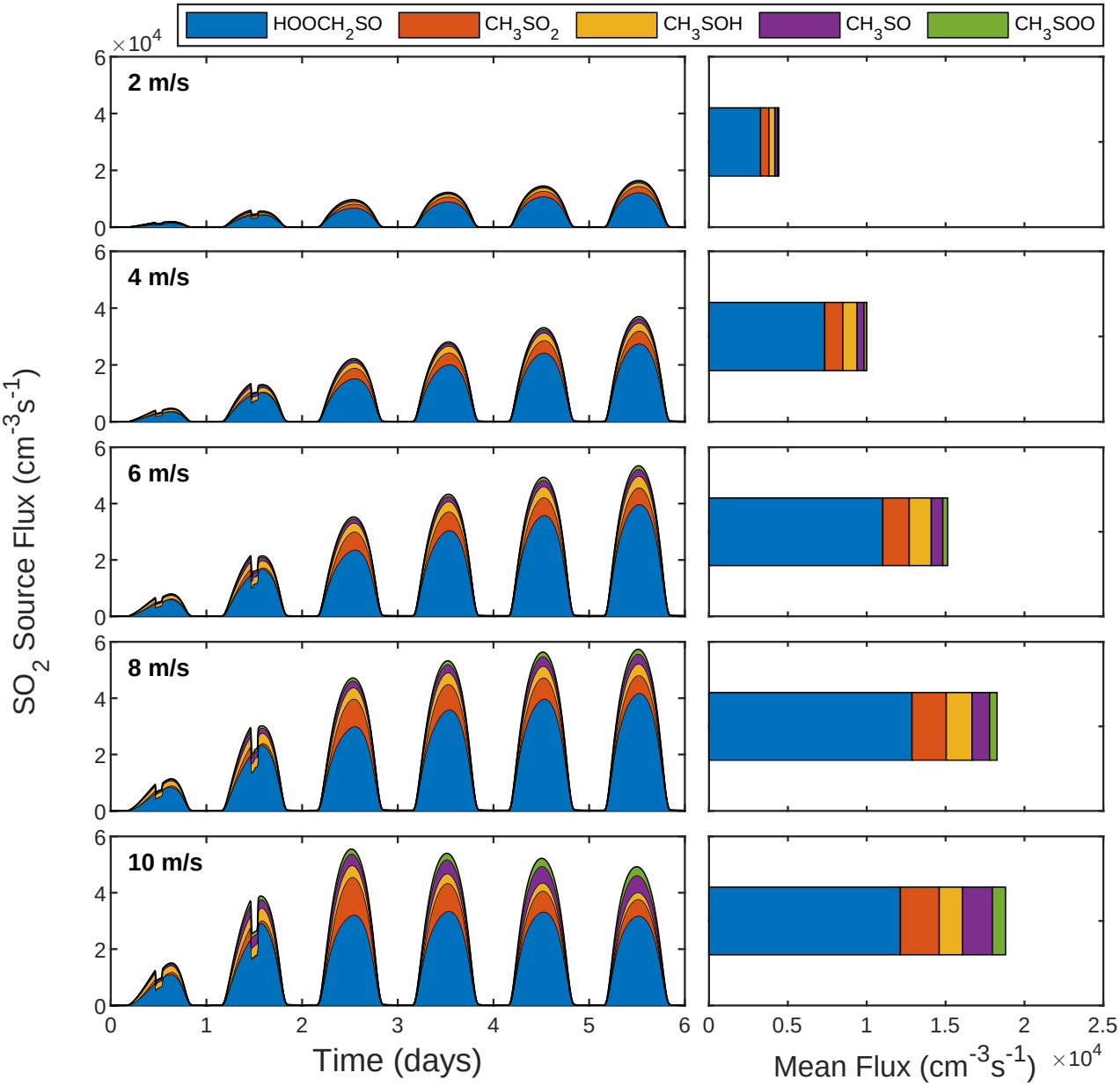

Figure S29. SO_2 source flux from $HOOCH_2SO$, CH_3SO_2, CH_3SOH, CH_3SO and CH_3SOO at varying wind-speeds ranging from 2 m/s to 10 m/s. Reactions that contribute < 1% of the total source flux are not displayed in the figure.

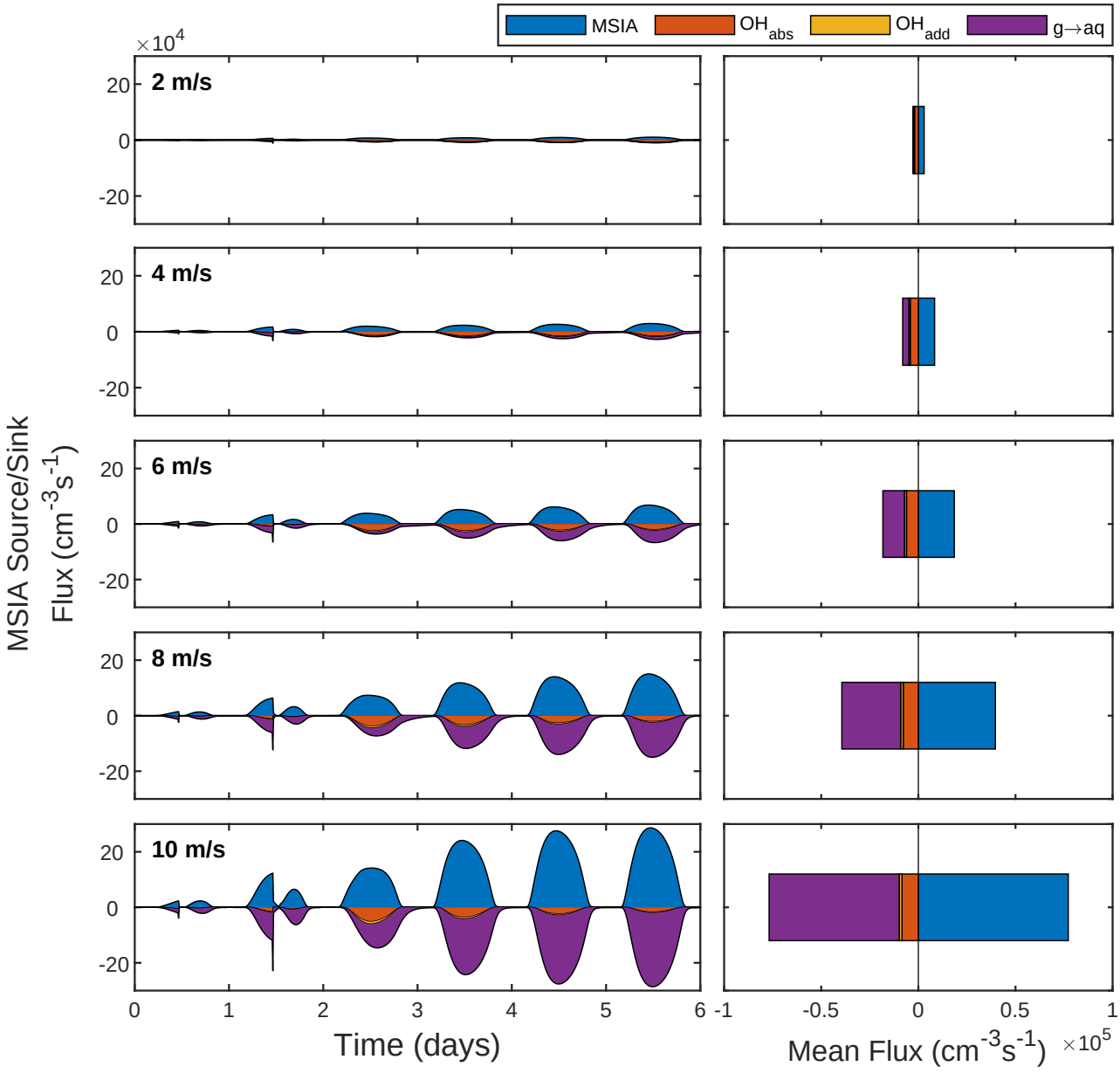

Figure S30. MSIA source/sink flux from DMSO and via reaction with OH (abstraction), OH (addition) and gas-aqueous phase uptake at varying wind-speeds ranging from 2 $\mathrm{m/s}$ to 10 $\mathrm{m/s}$. Reactions that contribute < 1% of the total source/sink flux are not displayed in the figure.

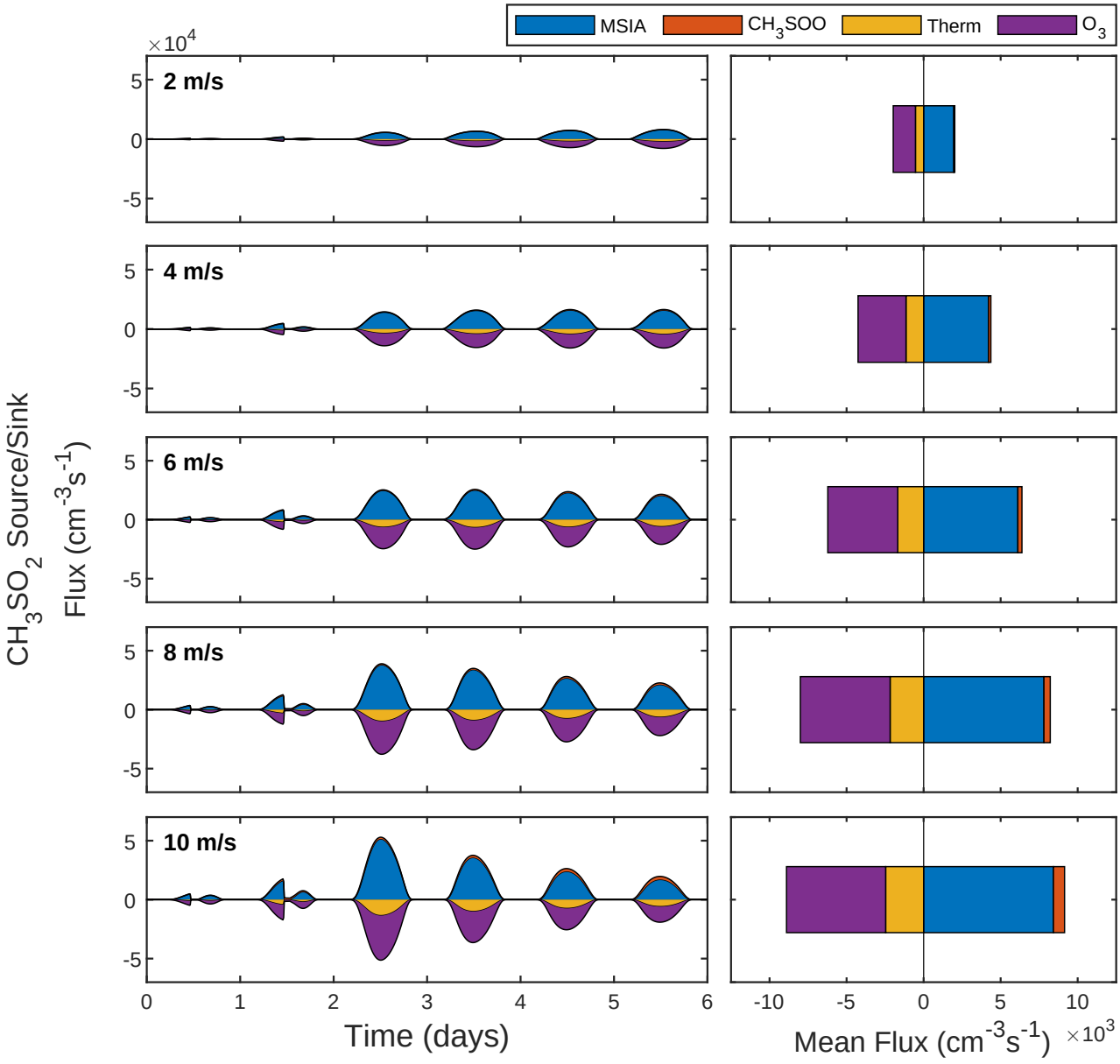

Figure S31. CH_3SO_2 source/sink flux from MSIA, CH_3SOO and via thermal decomposition and reaction with O_3 at varying wind-speeds ranging from 2 $\mathrm{m/s}$ to 10 $\mathrm{m/s}$. Reactions that contribute < 1% of the total source/sink flux are not displayed in the figure.

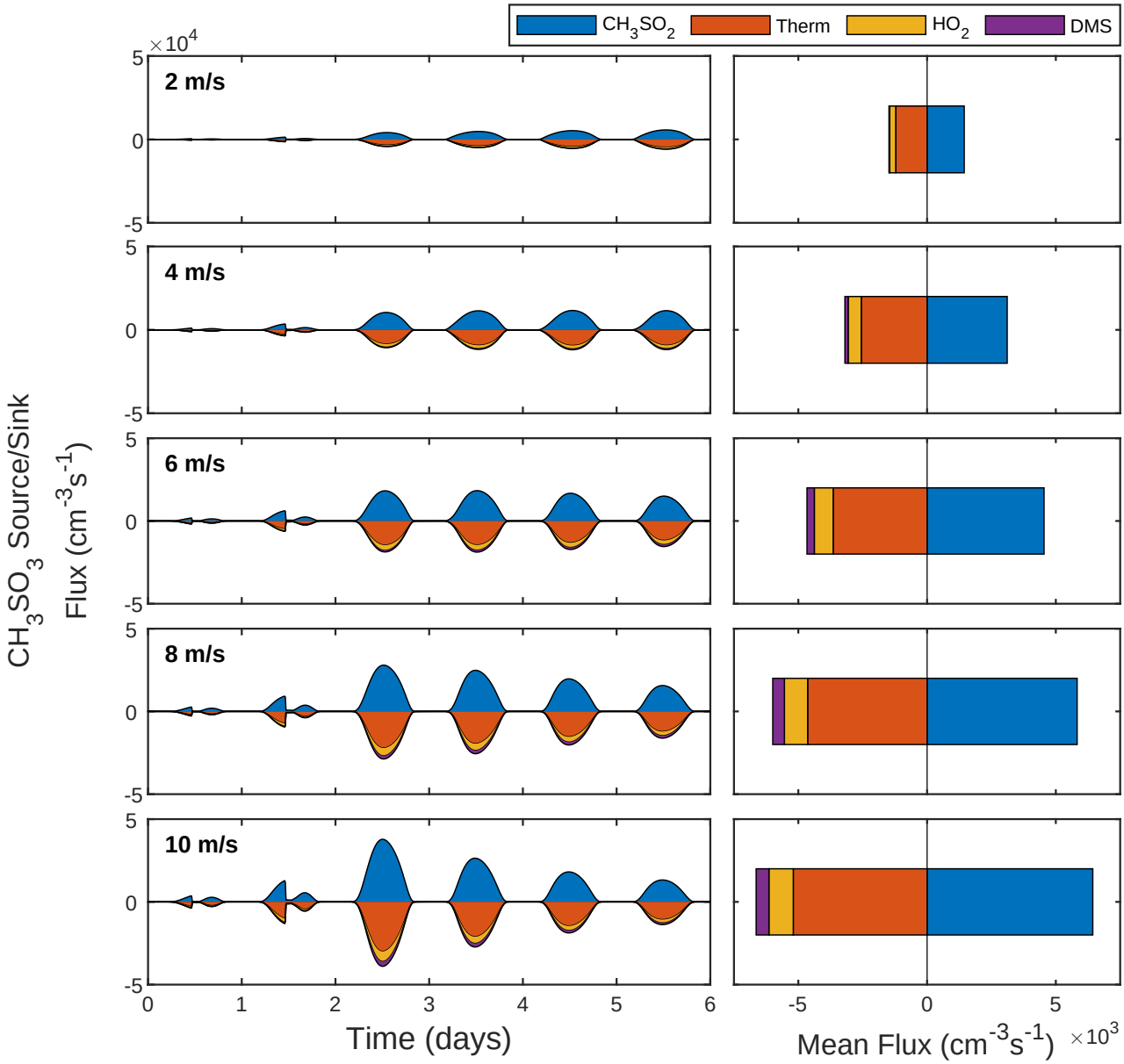

Figure S32. CH_3SO_3 source/sink flux from CH_3SO_2, via thermal decomposition and reaction with HO_2 and DMS at varying wind-speeds ranging from 2 $\mathrm{m/s}$ to 10 $\mathrm{m/s}$. Reactions that contribute < 1% of the total source/sink flux are not displayed in the figure.

S6 Precipitation sensitivity runs

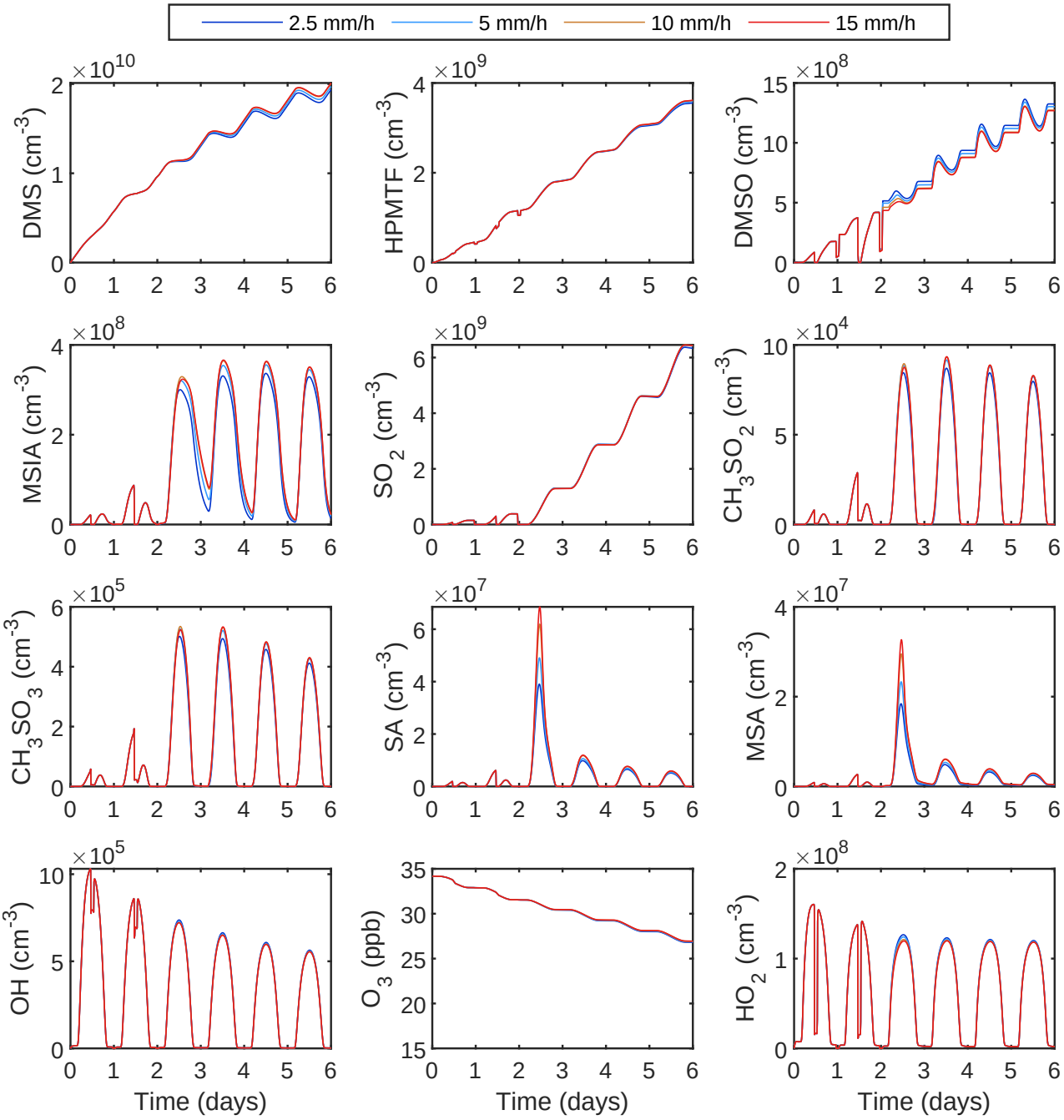

Figure S33. Concentrations of key gas-phase species at varying rates of precipitation ranging from 2.5 mm/h to 15 mm/h.

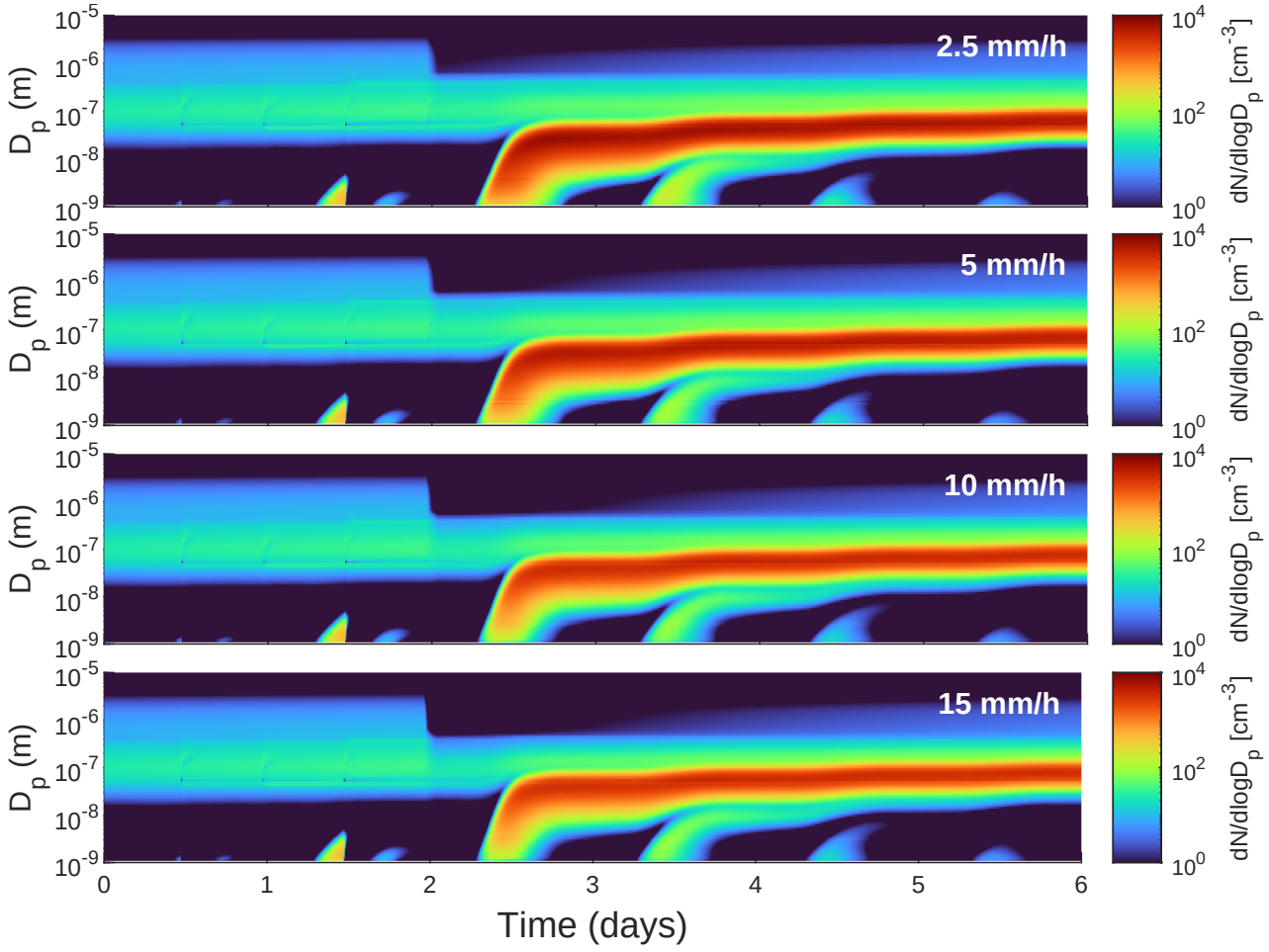

Figure S34. Aerosol particle number size distributions throughout the full simulation period at varying rates of precipitation ranging from 2.5 mm/h to 15 mm/h.

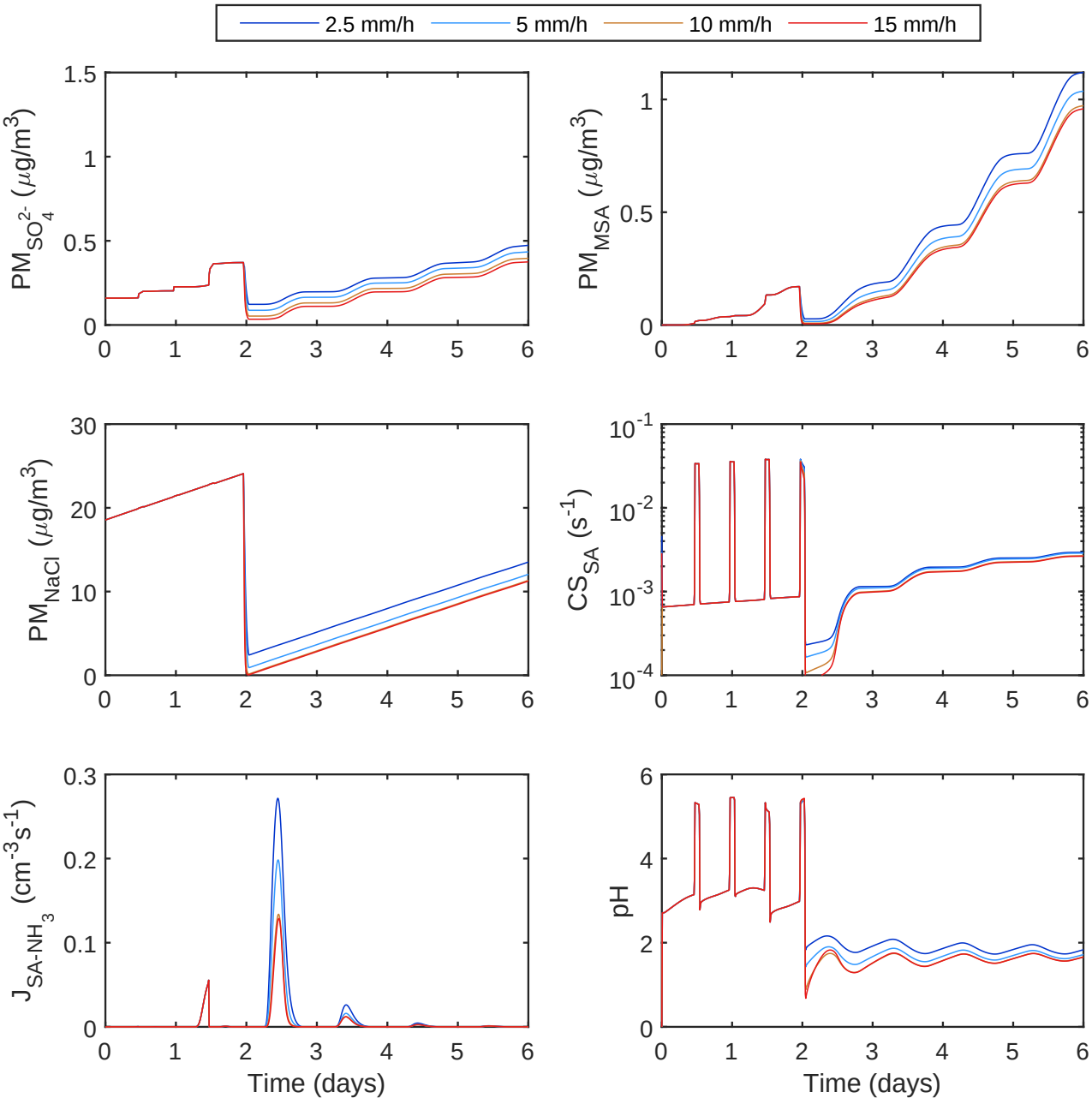

Figure S35. Total SO_4^{2-}, MSA and NaCl PM along with the SA condensation sink, SA-NH_3 driven nucleation rate and bulk pH at varying rates of precipitation ranging from 2.5 $\mathrm{mm/h}$ to 15 $\mathrm{mm/h}$.

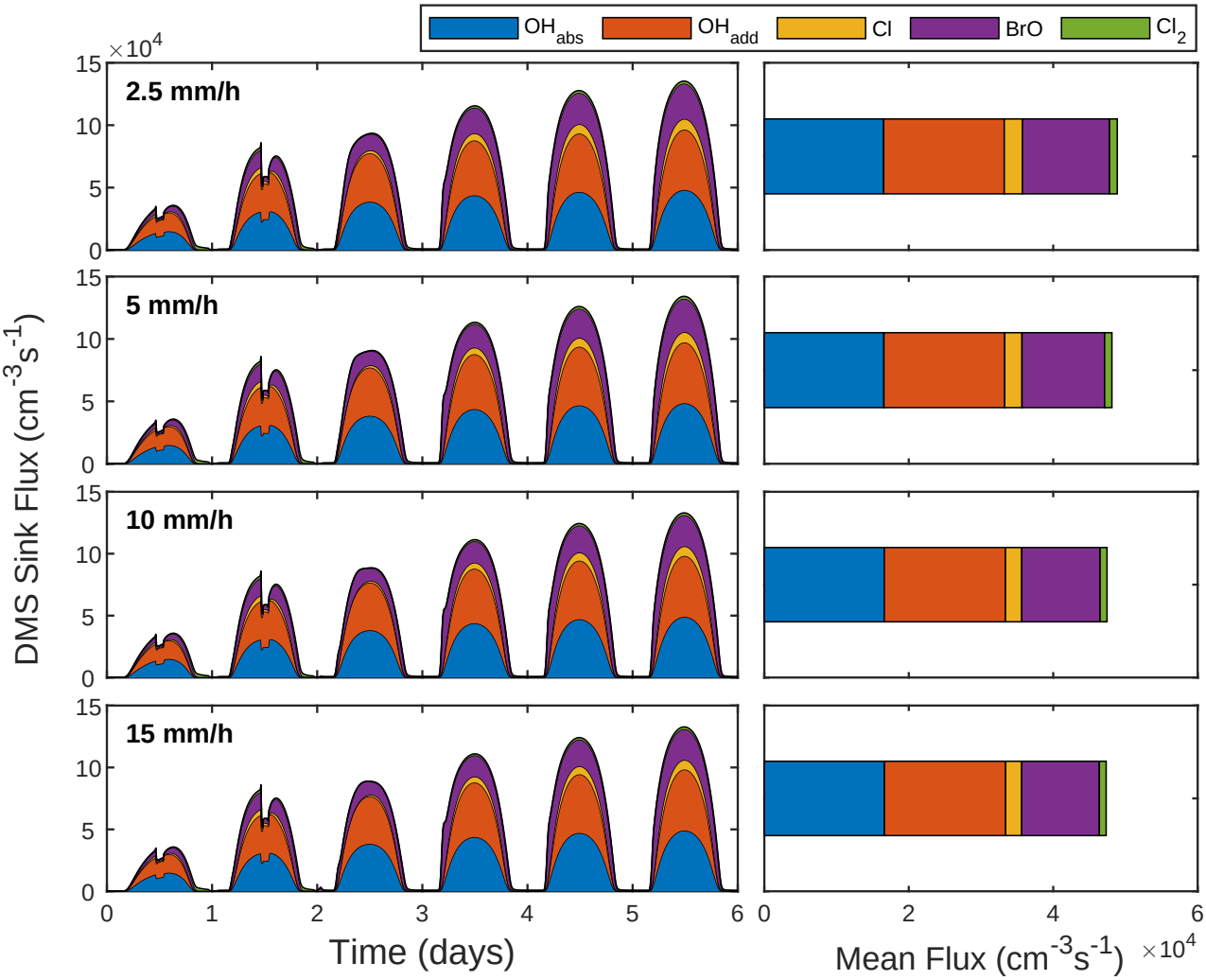

Figure S36. DMS sink flux driven by the reaction with OH (addition), OH (abstraction), Cl, Bro and Cl_2 at varying rates of precipitation ranging from 2.5 $\mathrm{mm/h}$ to 15 $\mathrm{mm/h}$. Reactions that contribute < 1% of the total sink flux are not displayed in the figure.

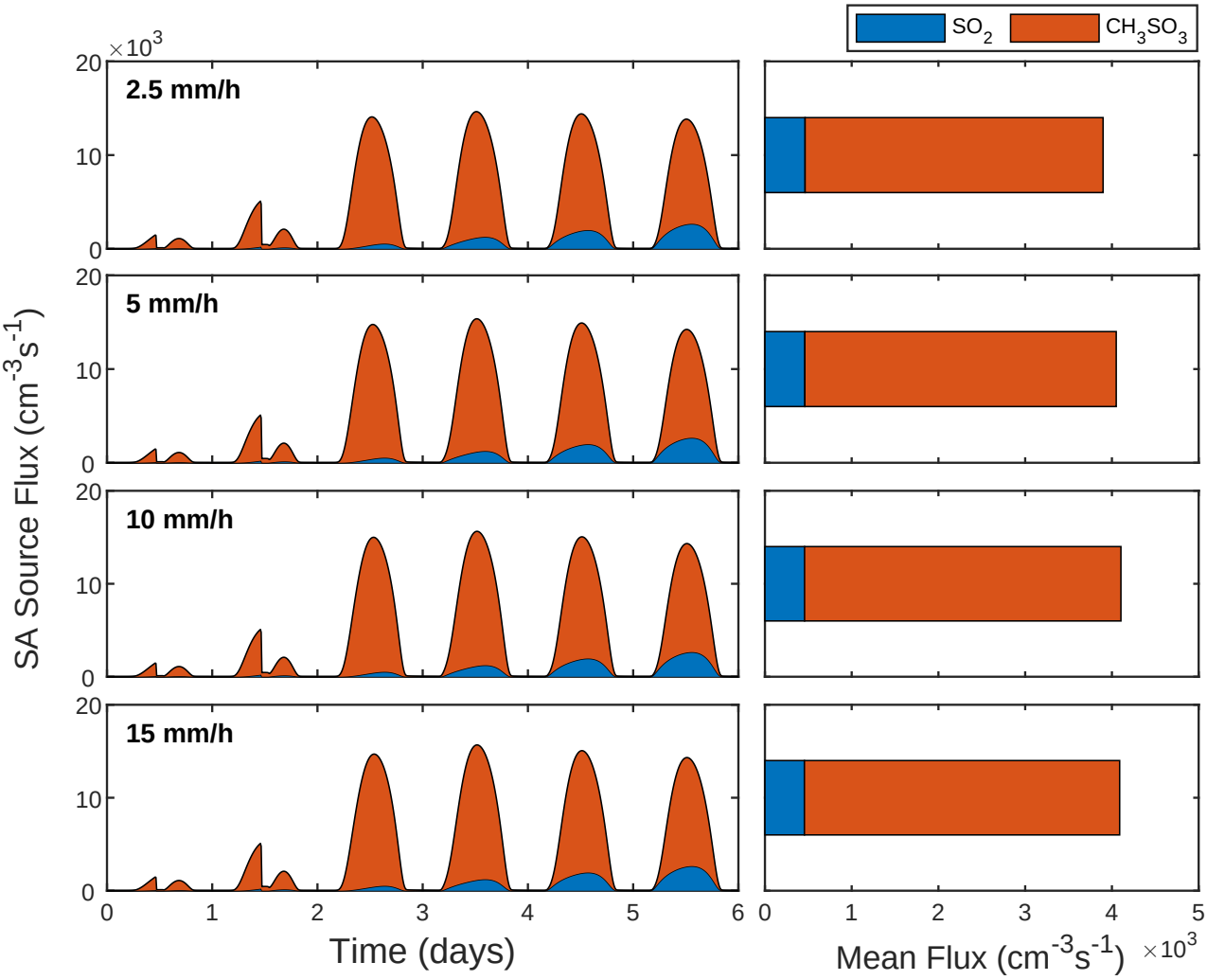

Figure S37. SA source flux from SO_2 and CH_3SO_3 at varying rates of precipitation ranging from 2.5 mm/h to 15 mm/h.

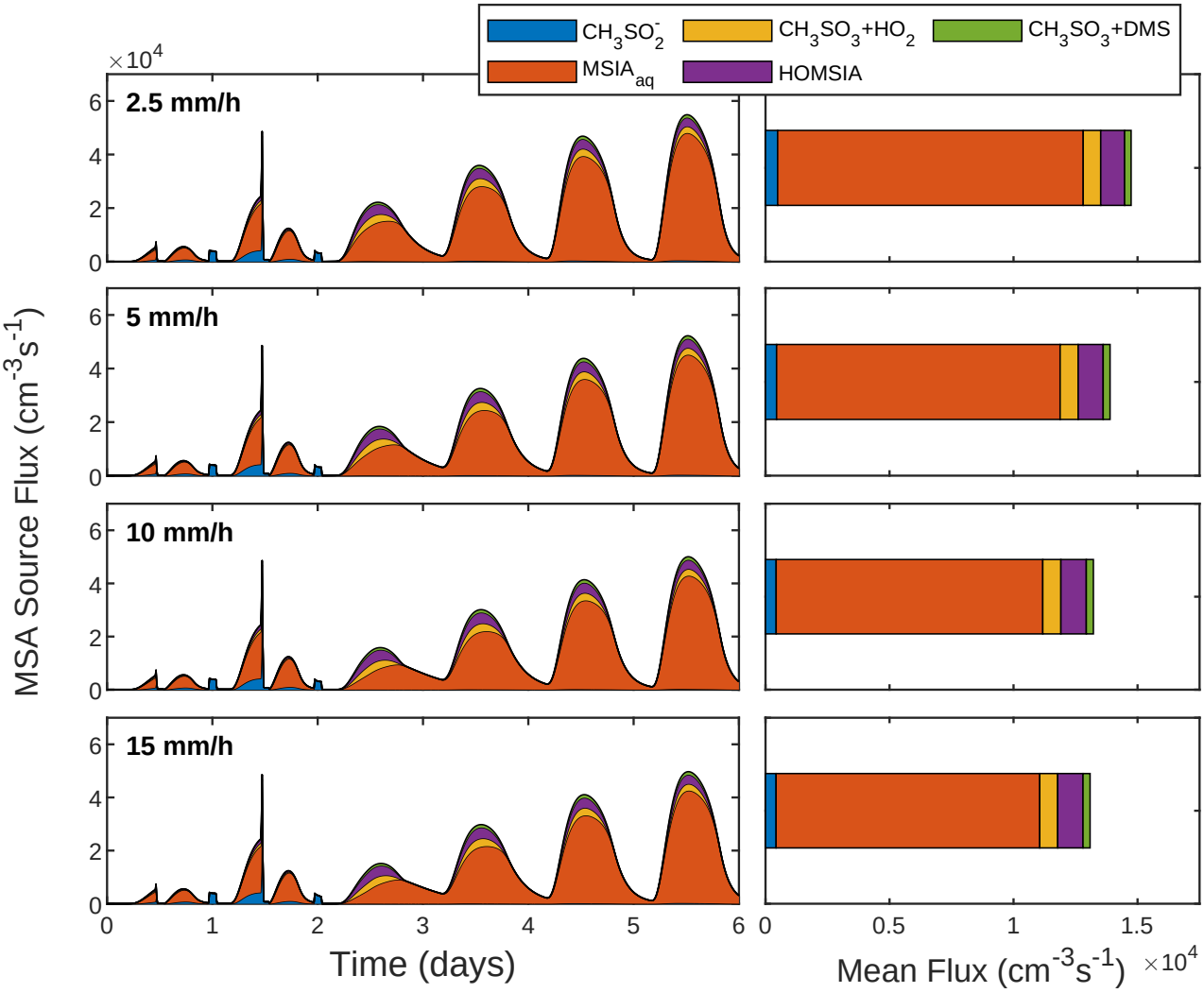

Figure S38. MSA source flux from $CH_3SO_2^-$ and $MSIA_{aq}$ in the aqueous-phase in addition to CH_3SO_3 via HO_2, CH_3SO_3 via DMS and HOMSIA in the gas-phase at varying rates of precipitation ranging from 2.5 mm/h to 15 mm/h.

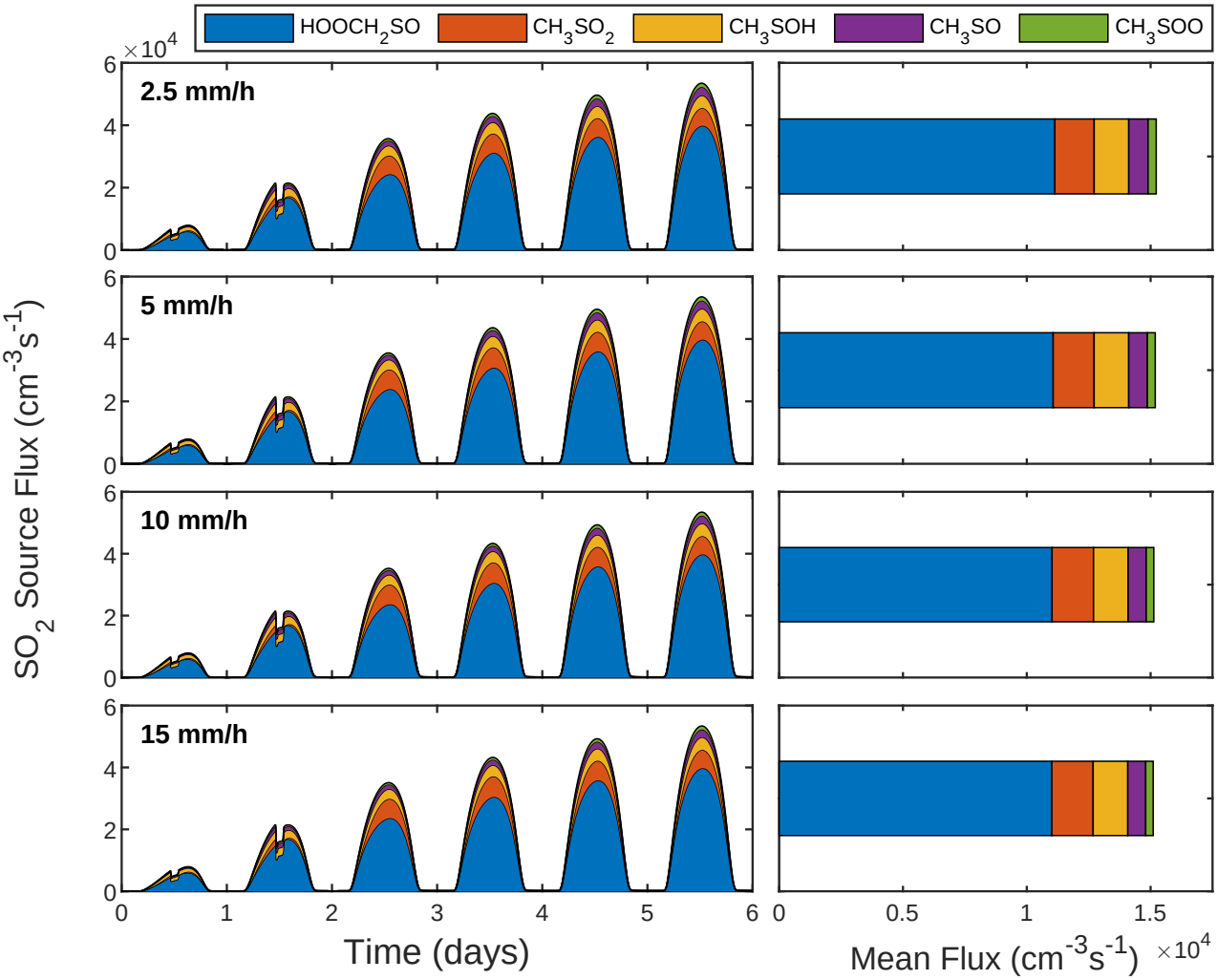

Figure S39. SO_2 source flux from $HOOCH_2SO$, CH_3SO_2, CH_3SOH, CH_3SO and CH_3SOO at varying rates of precipitation ranging from 2.5 mm/h to 15 mm/h. Reactions that contribute < 1% of the total source flux are not displayed in the figure.

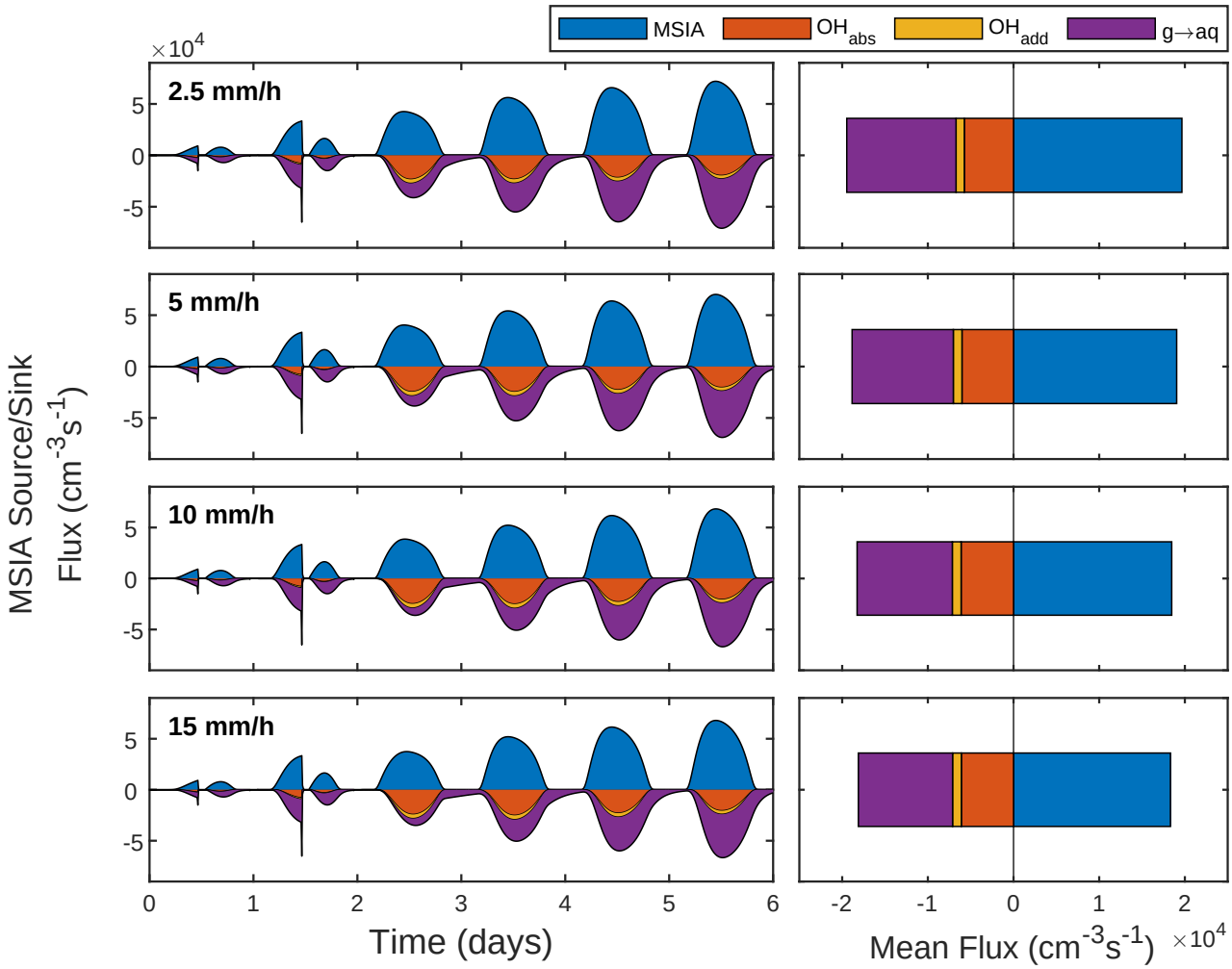

Figure S40. MSIA source/sink flux from DMSO and via reaction with OH (abstraction), OH (addition) and gas-aqueous phase uptake at varying rates of precipitation ranging from 2.5 $\mathrm{mm/h}$ to 15 $\mathrm{mm/h}$. Reactions that contribute < 1% of the total source/sink flux are not displayed in the figure.

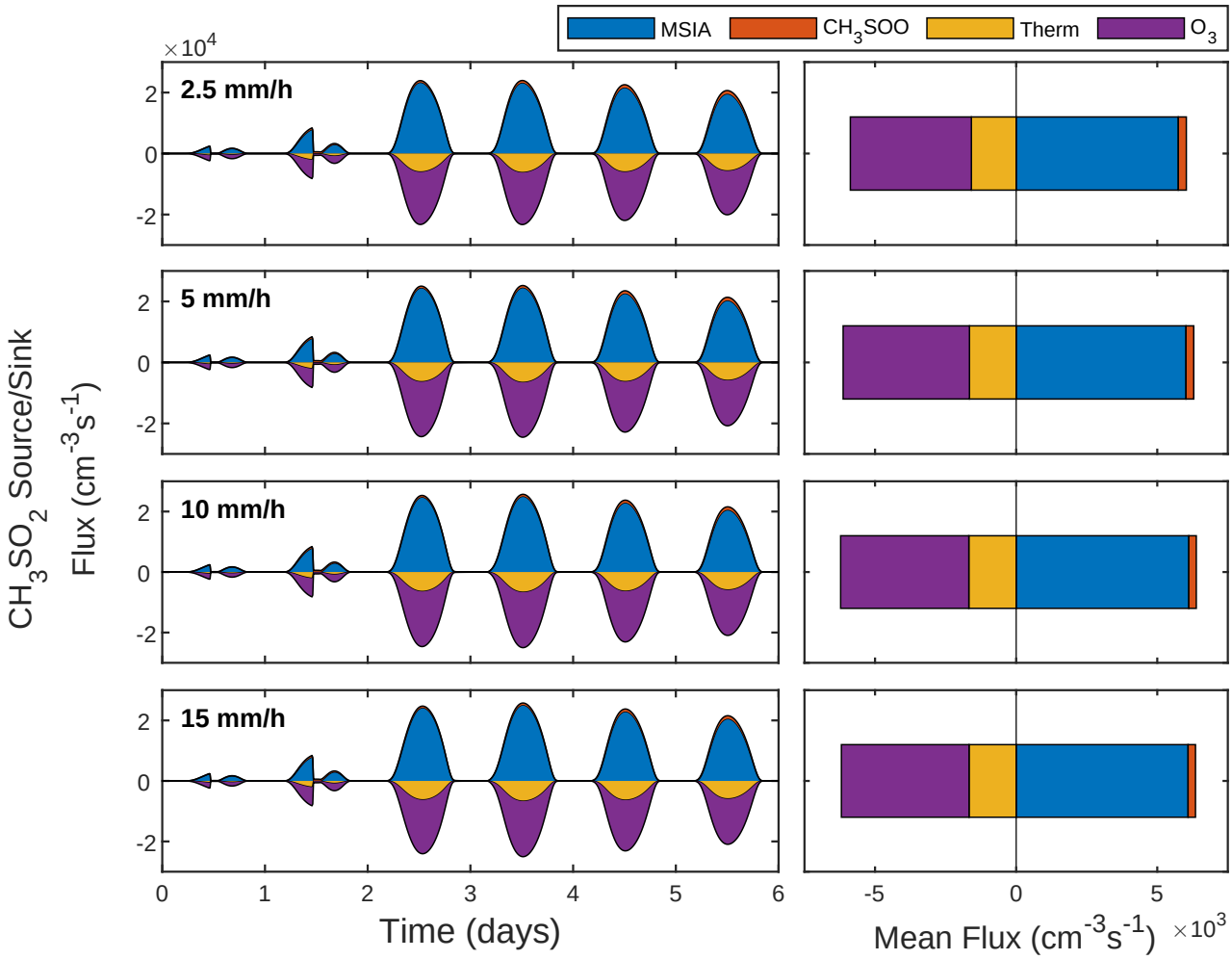

Figure S41. CH_3SO_2 source/sink flux from MSIA, CH_3SOO and via thermal decomposition and reaction with O_3 at varying rates of precipitation ranging from 2.5 $\mathrm{mm/h}$ to 15 $\mathrm{mm/h}$. Reactions that contribute < 1% of the total source/sink flux are not displayed in the figure.

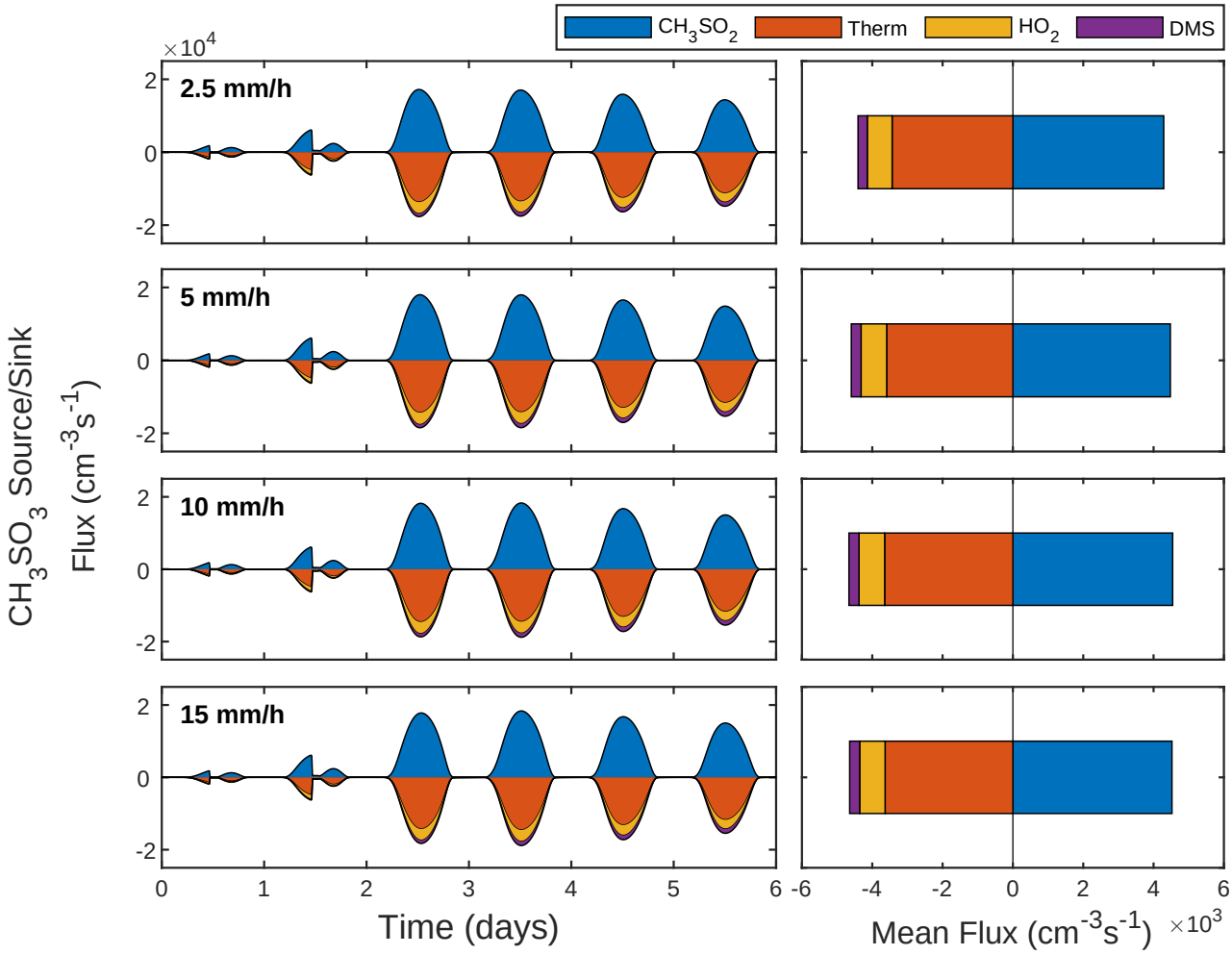

Figure S42. CH_3SO_3 source/sink flux from CH_3SO_2, via thermal decomposition and reaction with HO_2 and DMS at varying rates of precipitation ranging from 2.5 $\mathrm{mm/h}$ to 15 $\mathrm{mm/h}$. Reactions that contribute < 1% of the total source/sink flux are not displayed in the figure.

S7 Sea surface temperature sensitivity runs

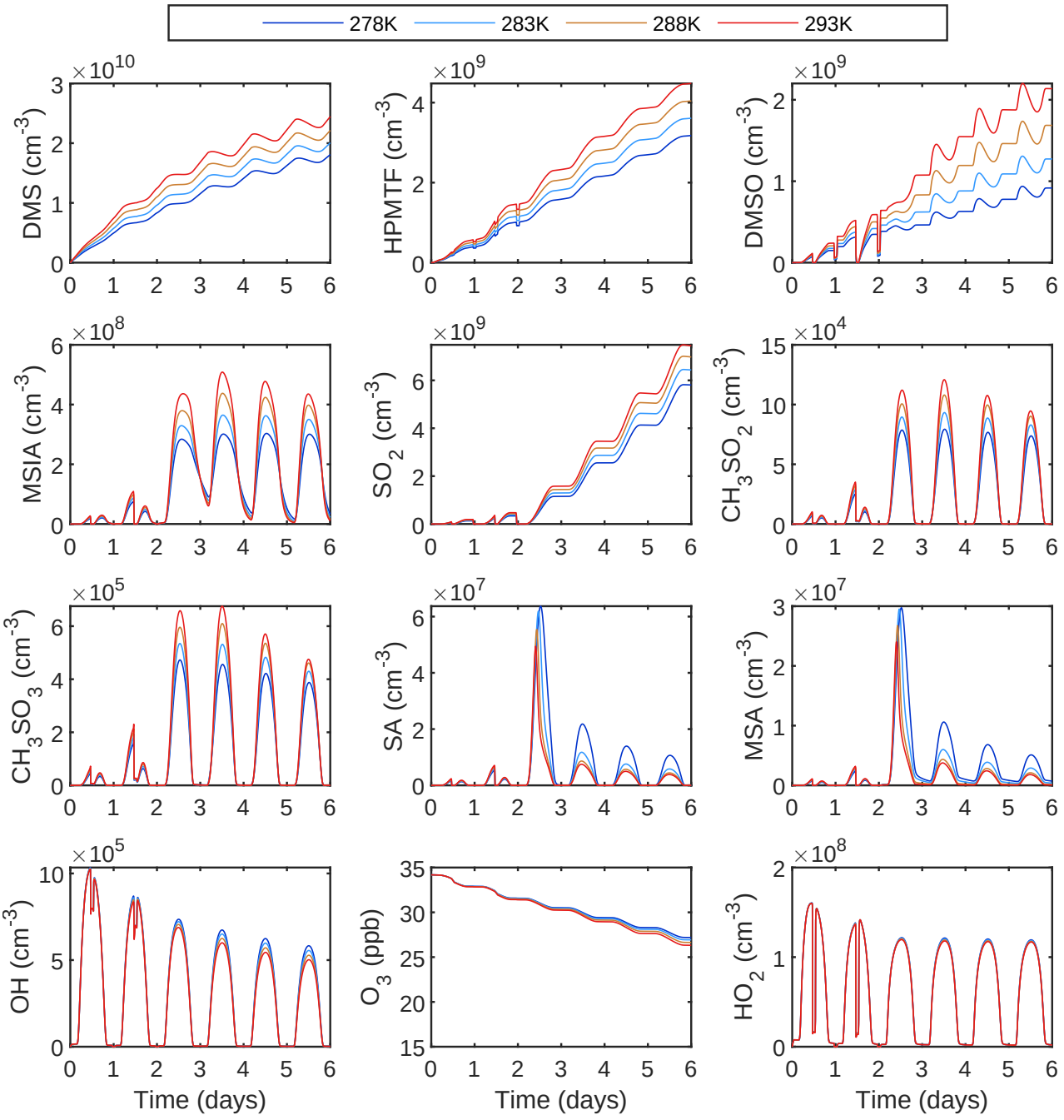

Figure S43. Concentrations of key gas-phase species at varying sea surface temperatures ranging from 278 K to 293 K.

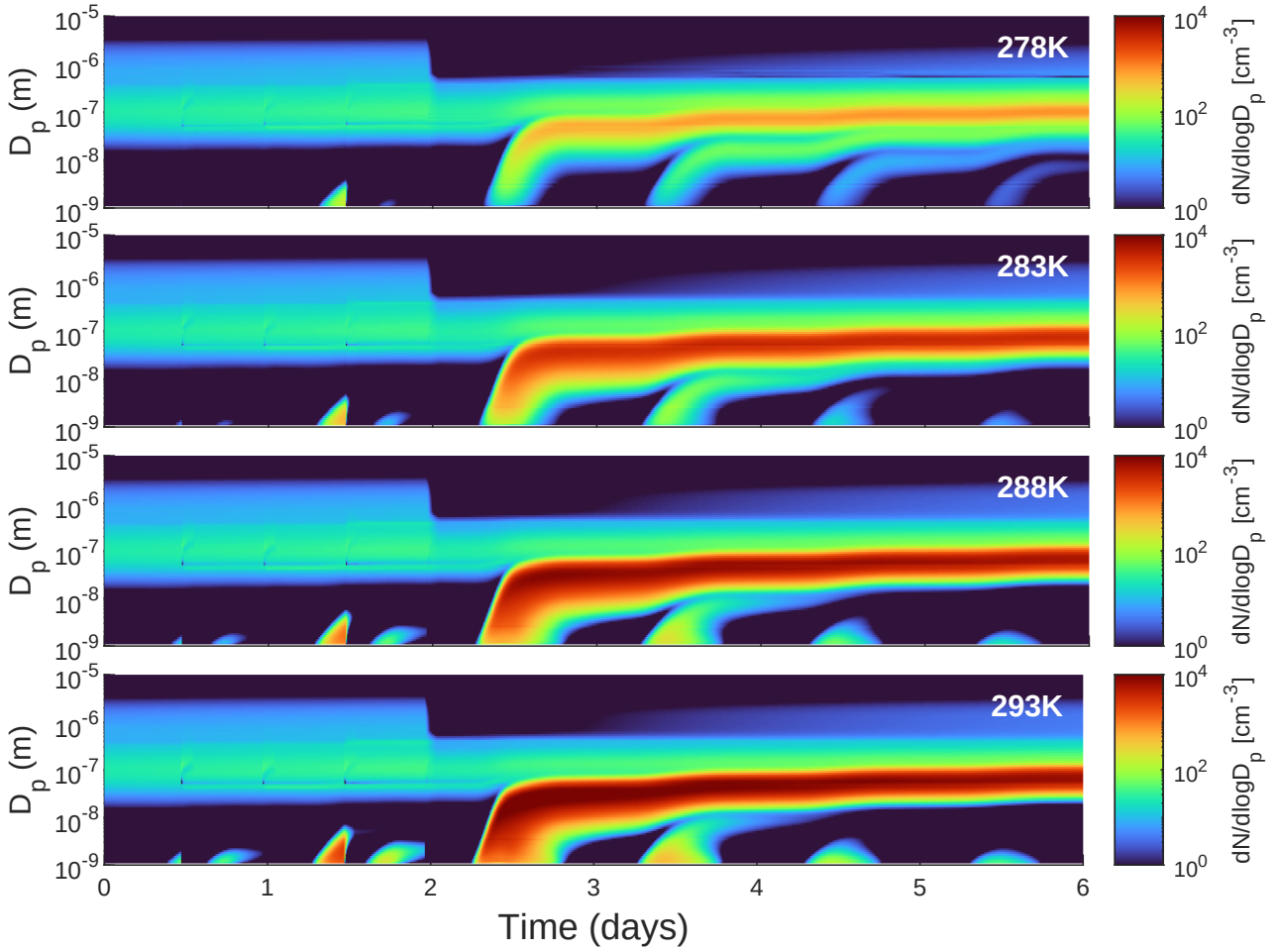

Figure S44. Aerosol particle number size distributions throughout the full simulation period at varying sea surface temperatures ranging from 278 K to 293 K.

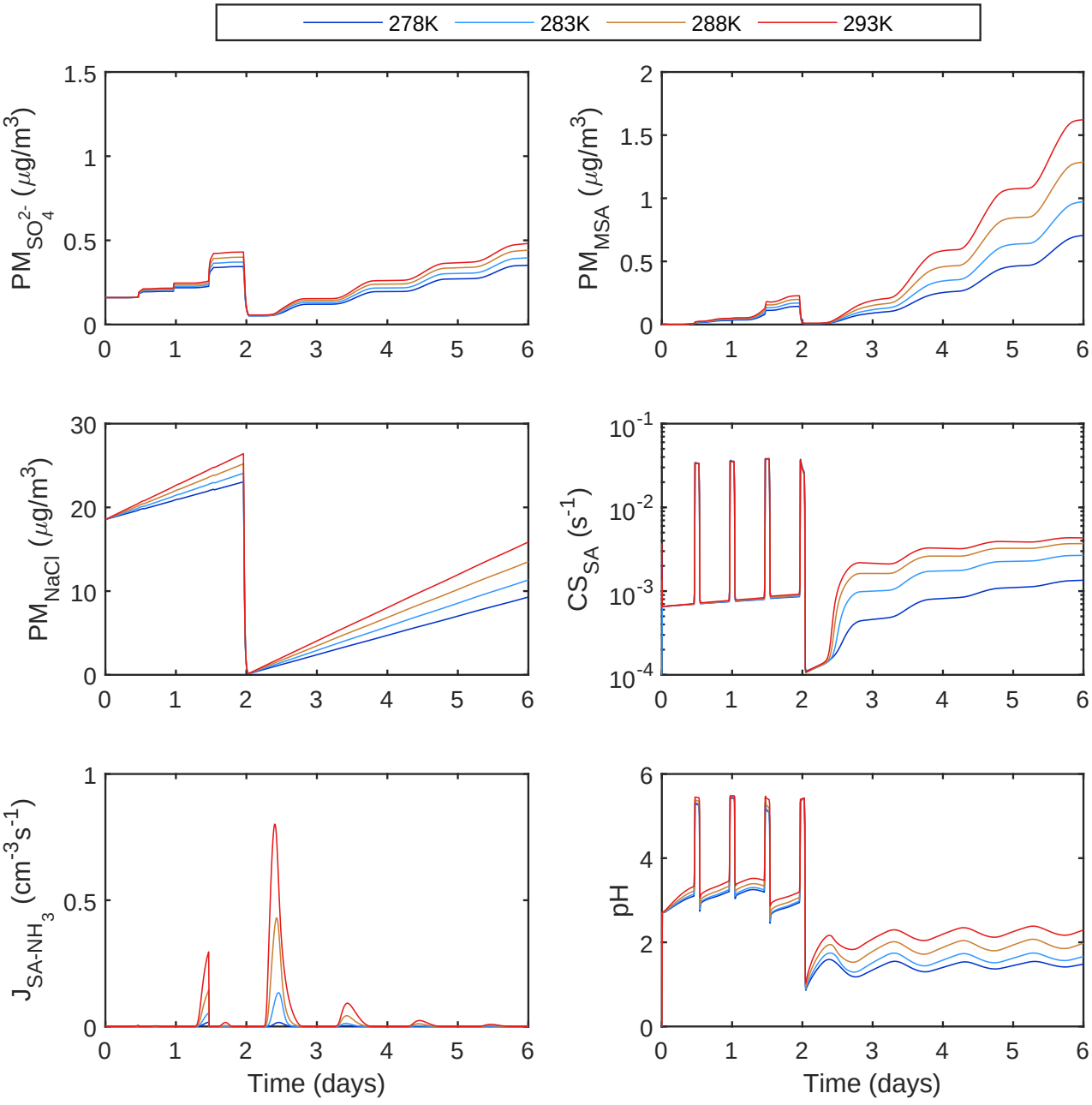

Figure S45. Total SO_4^{2-}, MSA and NaCl PM along with the SA condensation sink, SA-NH_3 driven nucleation rate and bulk pH at varying sea surface temperatures ranging from 278 K to 293 K.

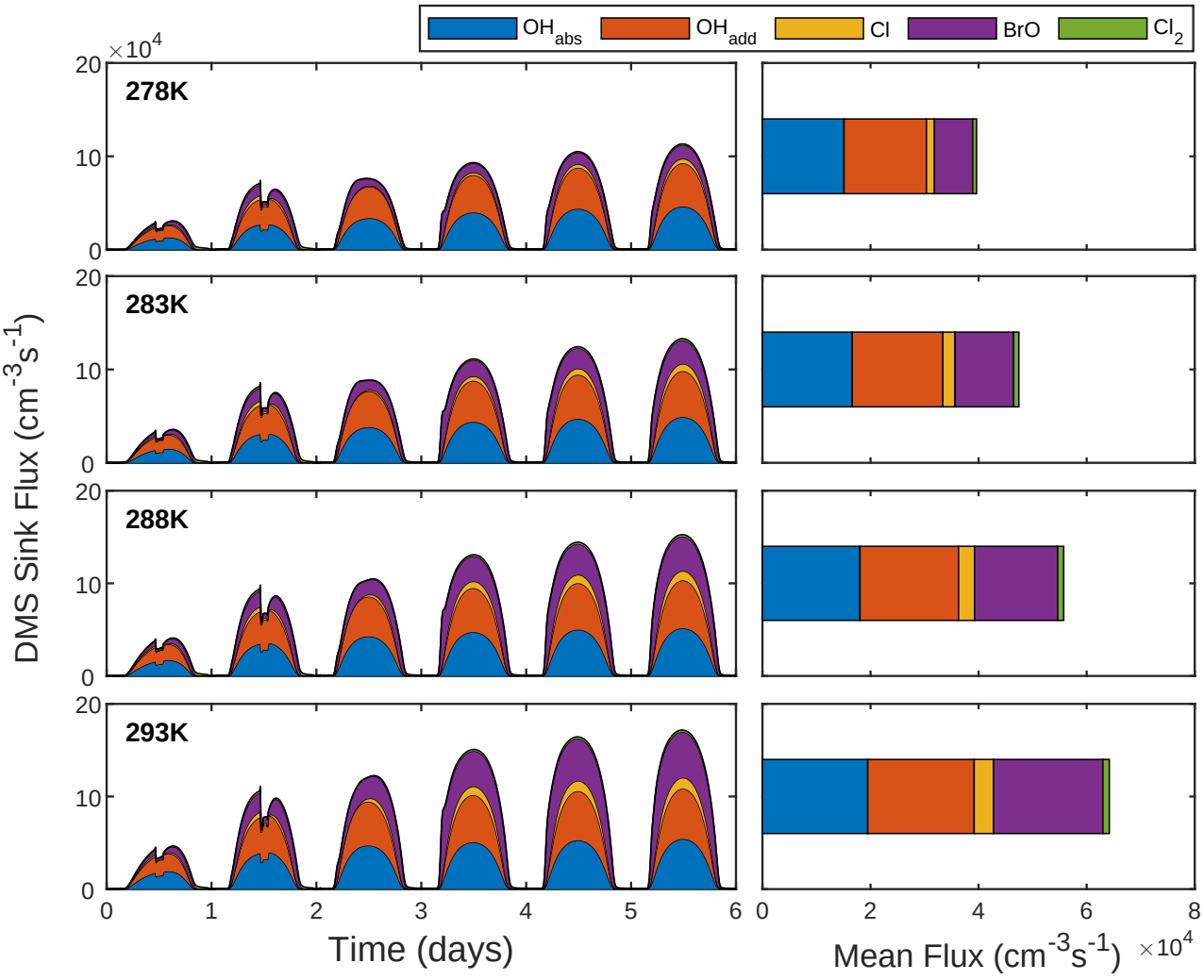

Figure S46. DMS sink flux driven by the reaction with OH (addition), OH (abstraction), Cl, Bro and Cl_2 at varying sea surface temperatures ranging from 278 K to 293 K. Reactions that contribute < 1% of the total sink flux are not displayed in the figure.

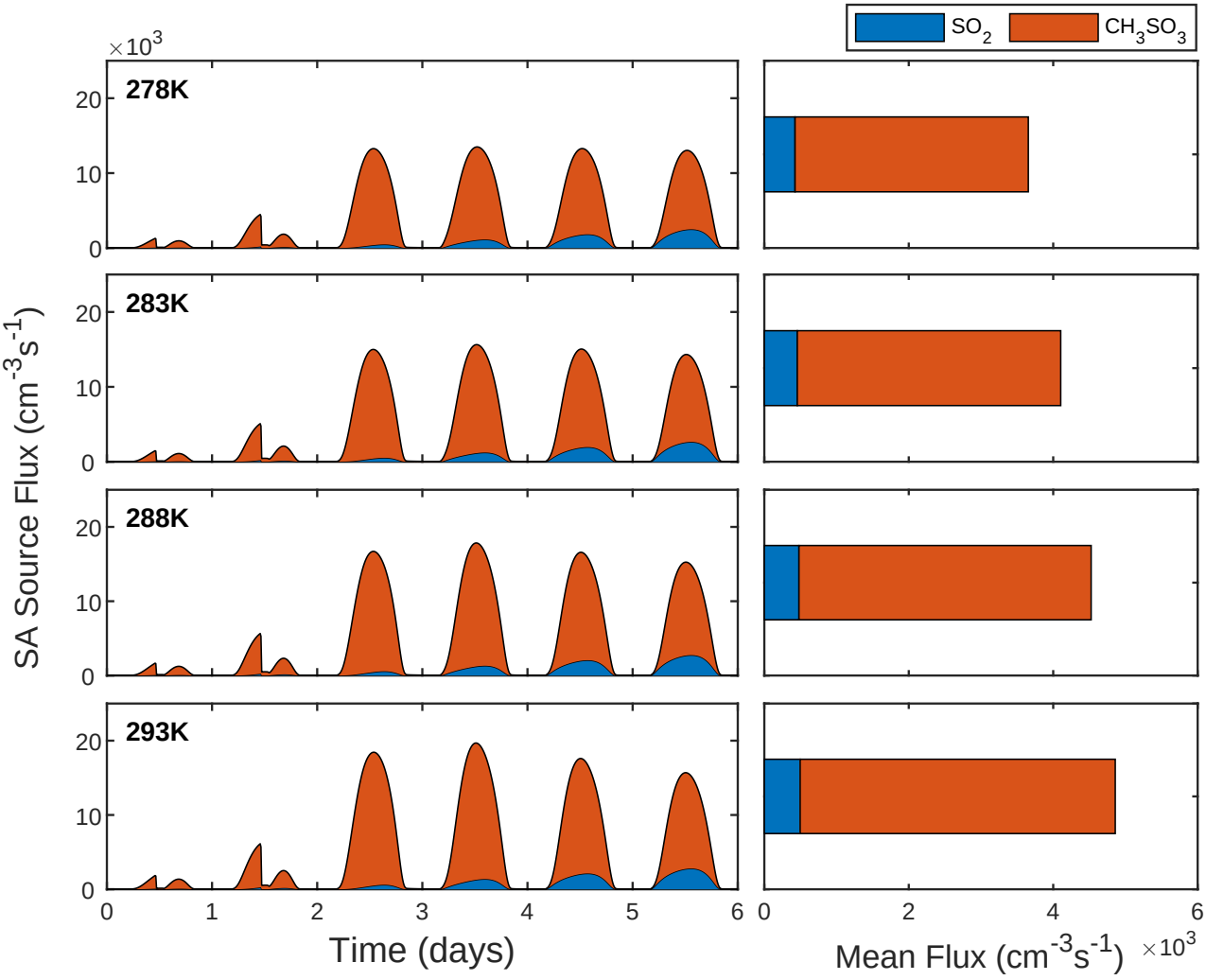

Figure S47. SA source flux from SO_2 and CH_3SO_3 at varying sea surface temperatures ranging from 278 K to 293 K

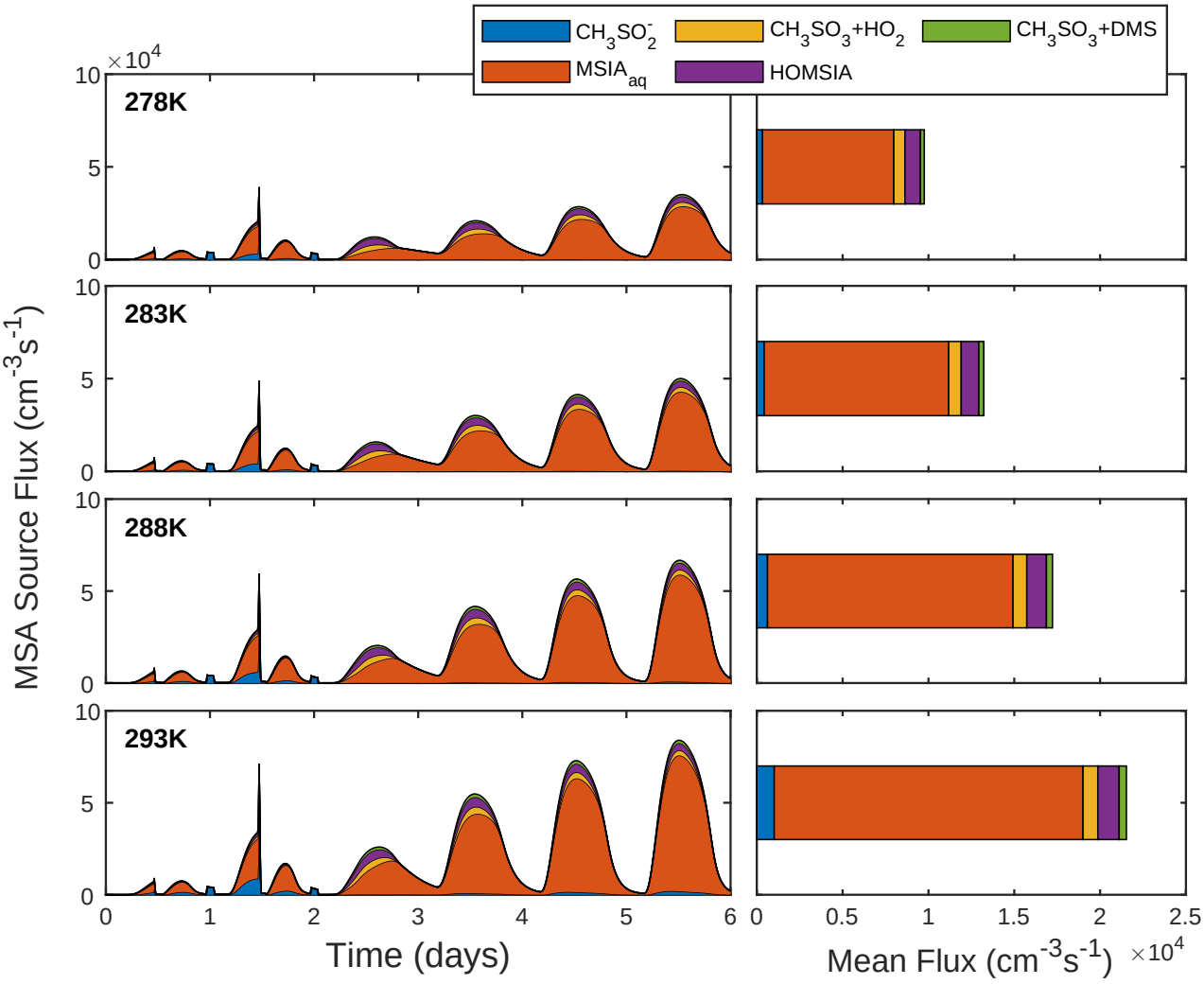

Figure S48. MSA source flux from $CH_3SO_2^-$ and $MSIA_{aq}$ in the aqueous-phase in addition to CH_3SO_3 via HO_2, CH_3SO_3 via DMS and HOMSIA in the gas-phase at varying sea surface temperatures ranging from 278 K to 293 K.

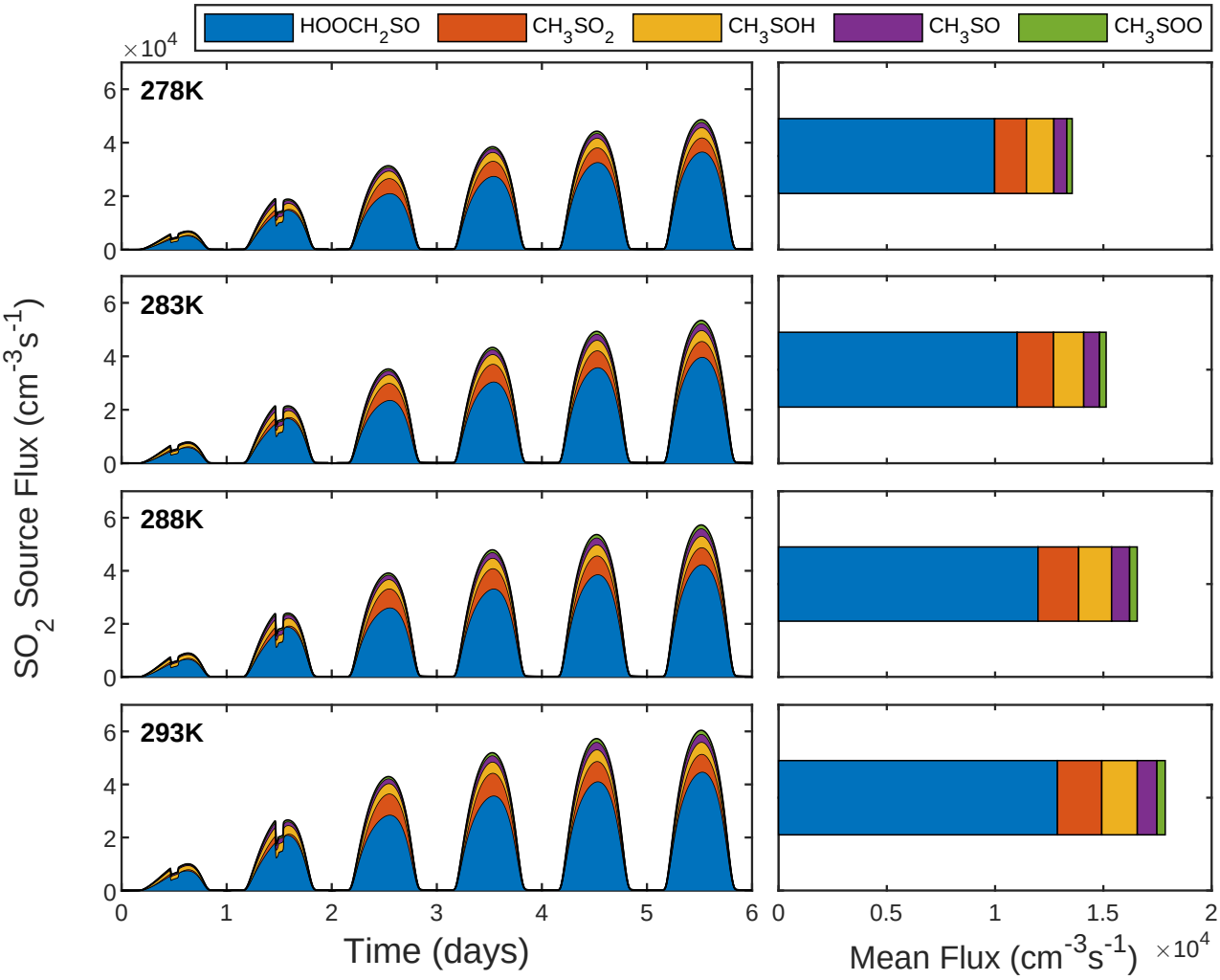

Figure S49. SO_2 source flux from $HOOCH_2SO$, CH_3SO_2, CH_3SOH, CH_3SO and CH_3SOO at varying sea surface temperatures ranging from 278 K to 293 K. Reactions that contribute < 1% of the total source flux are not displayed in the figure.

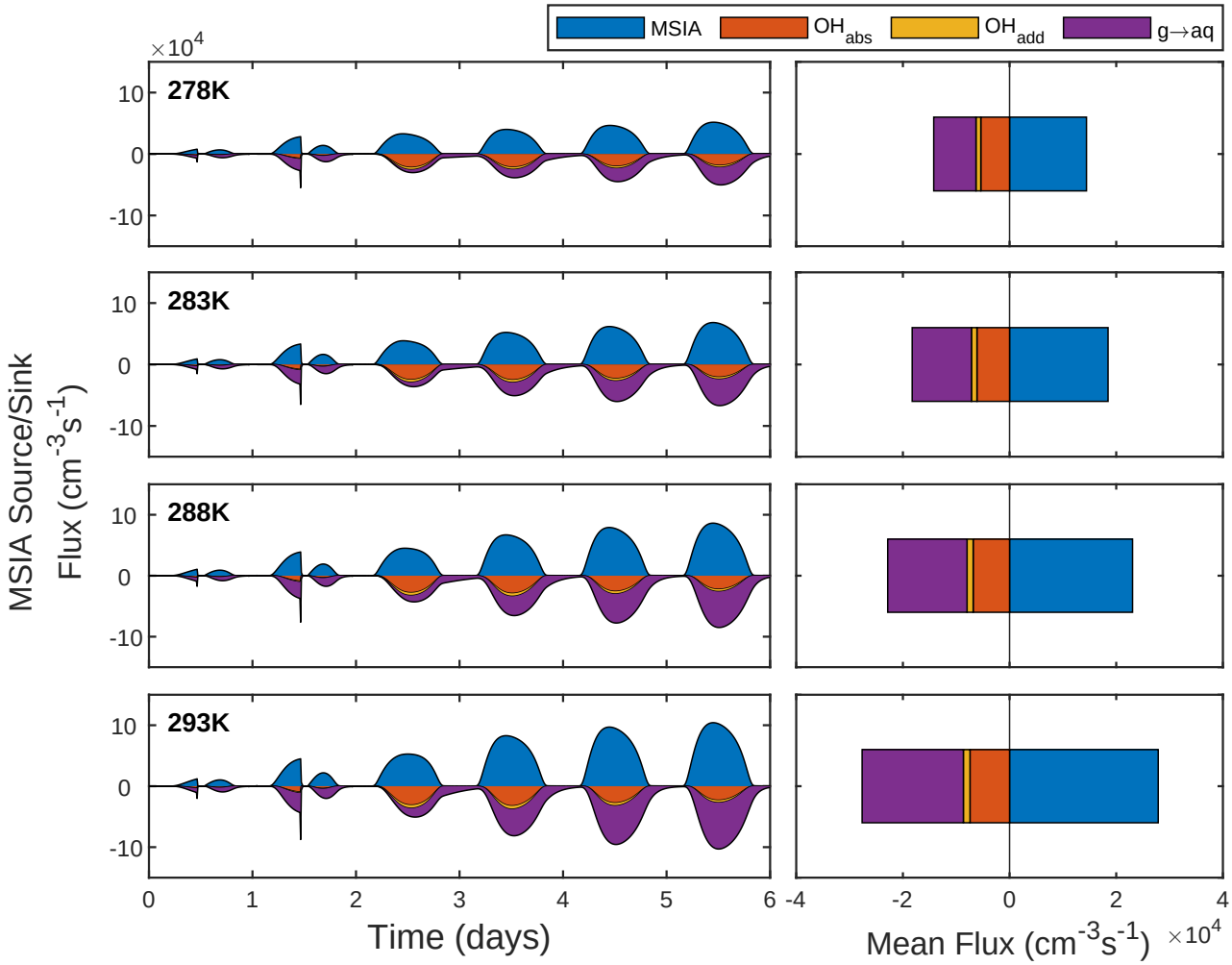

Figure S50. MSIA source/sink flux from DMSO and via reaction with OH (abstraction), OH (addition) and gas-aqueous phase uptake at varying sea surface temperatures ranging from 278 K to 293 K. Reactions that contribute < 1% of the total source/sink flux are not displayed in the figure.

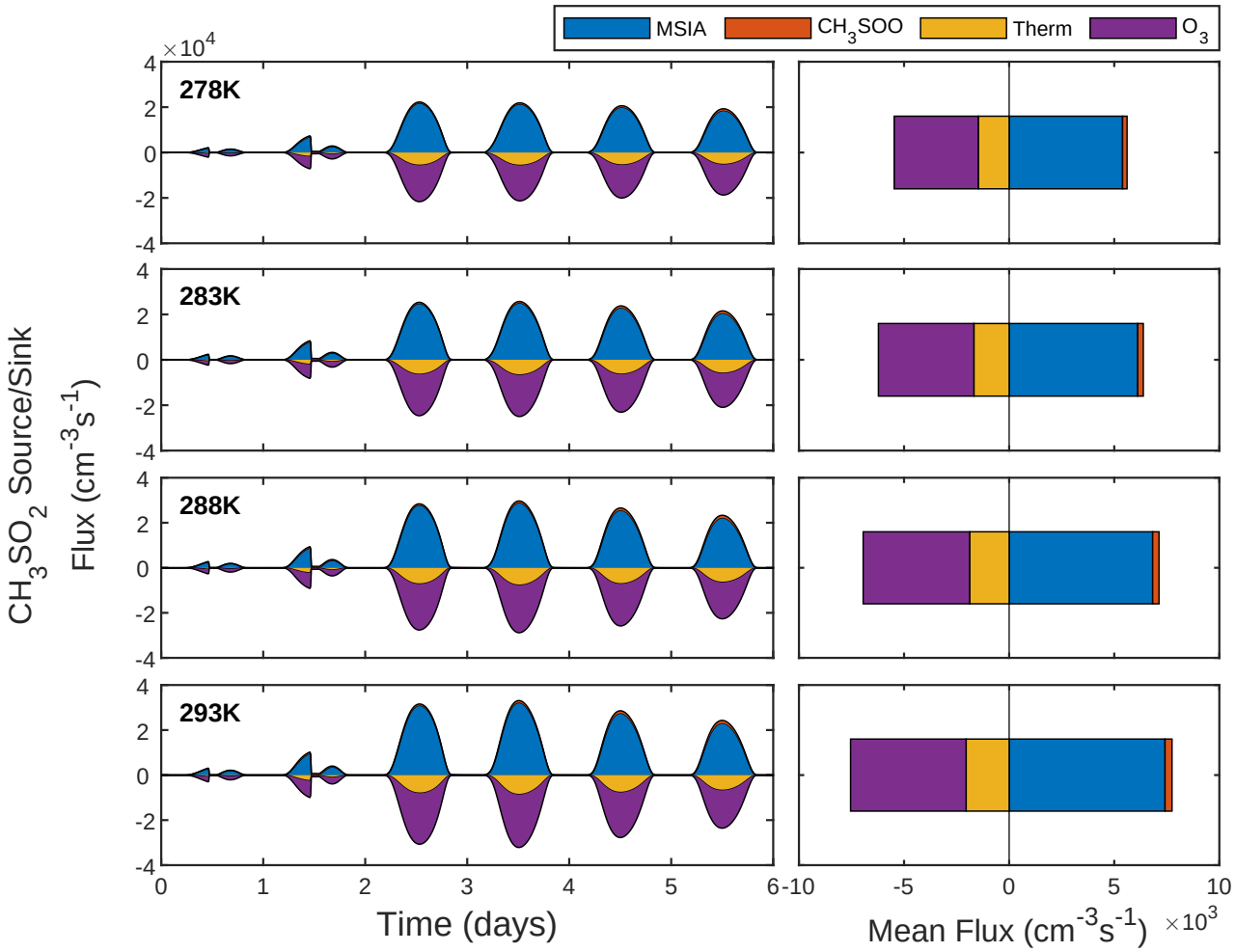

Figure S51. CH_3SO_2 source/sink flux from MSIA, CH_3SOO and via thermal decomposition and reaction with O_3 at varying sea surface temperatures ranging from 278 K to 293 K. Reactions that contribute < 1% of the total source/sink flux are not displayed in the figure.

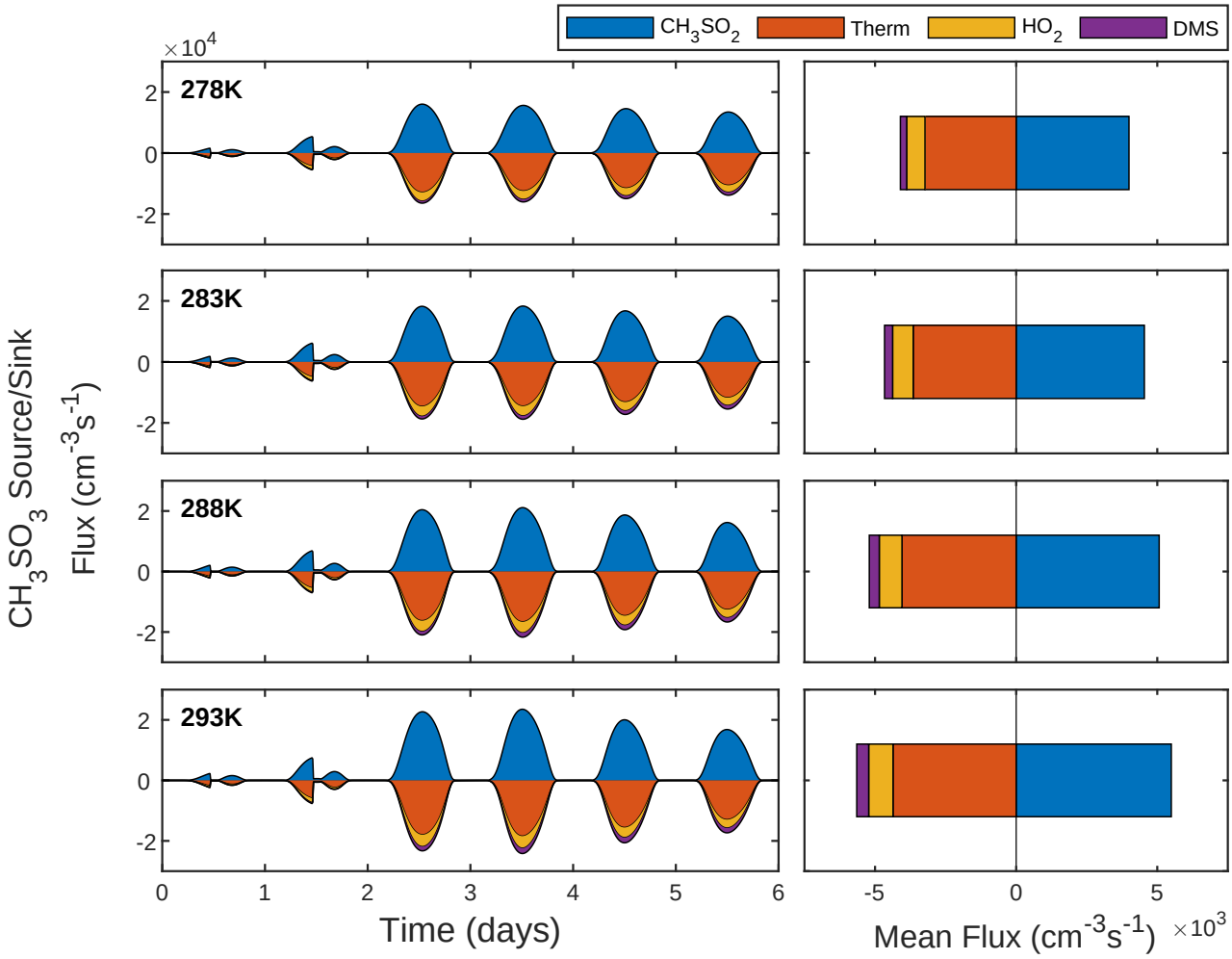

Figure S52. CH_3SO_3 source/sink flux from CH_3SO_2, via thermal decomposition and reaction with HO_2 and DMS at varying sea surface temperatures ranging from 278 K to 293 K. Reactions that contribute < 1% of the total source/sink flux are not displayed in the figure.

S8 DMS sea surface concentration sensitivity runs

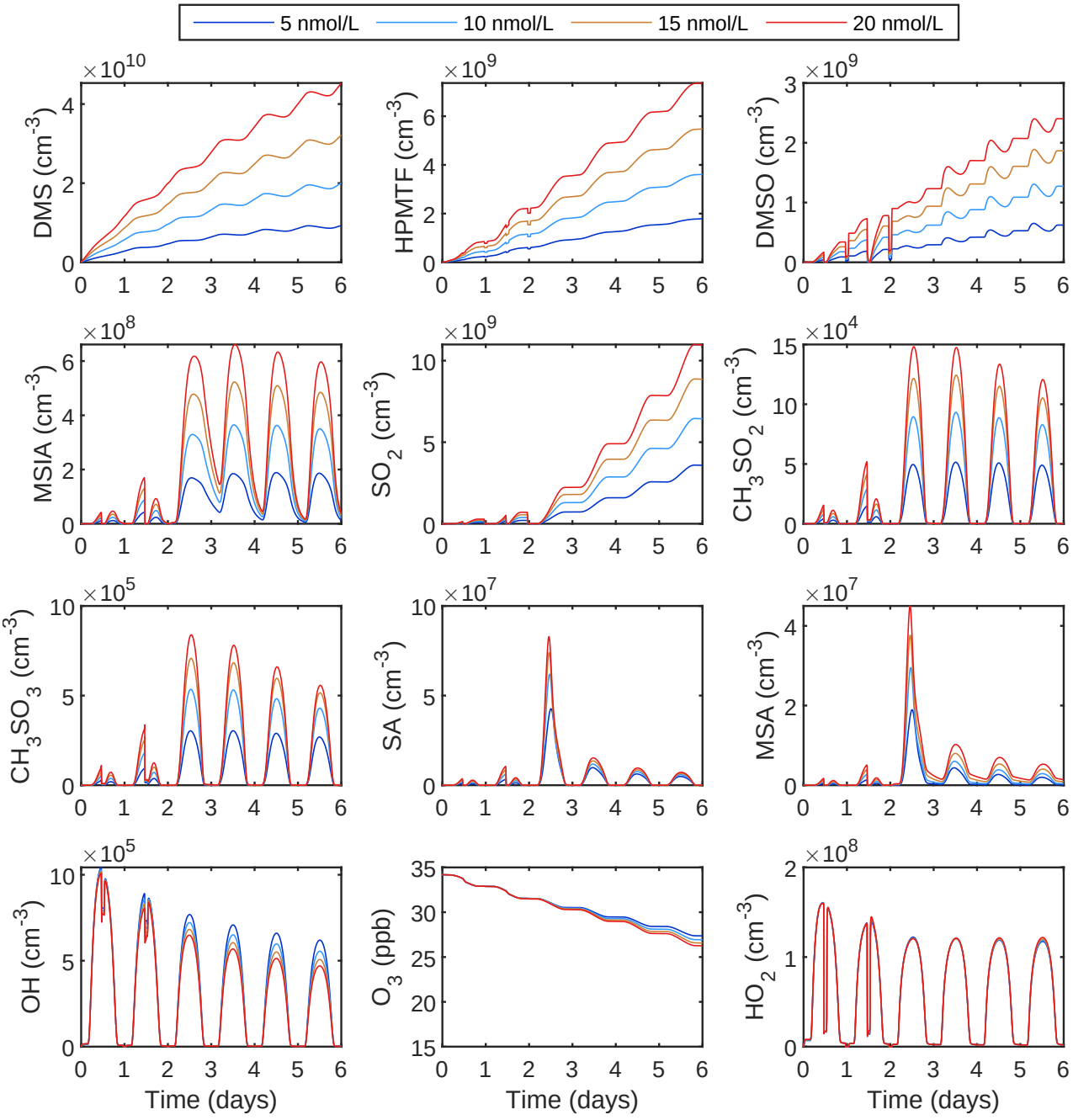

Figure S53. Concentrations of key gas-phase species at varying DMS sea surface concentrations ranging from 5 nM to 20 nM.

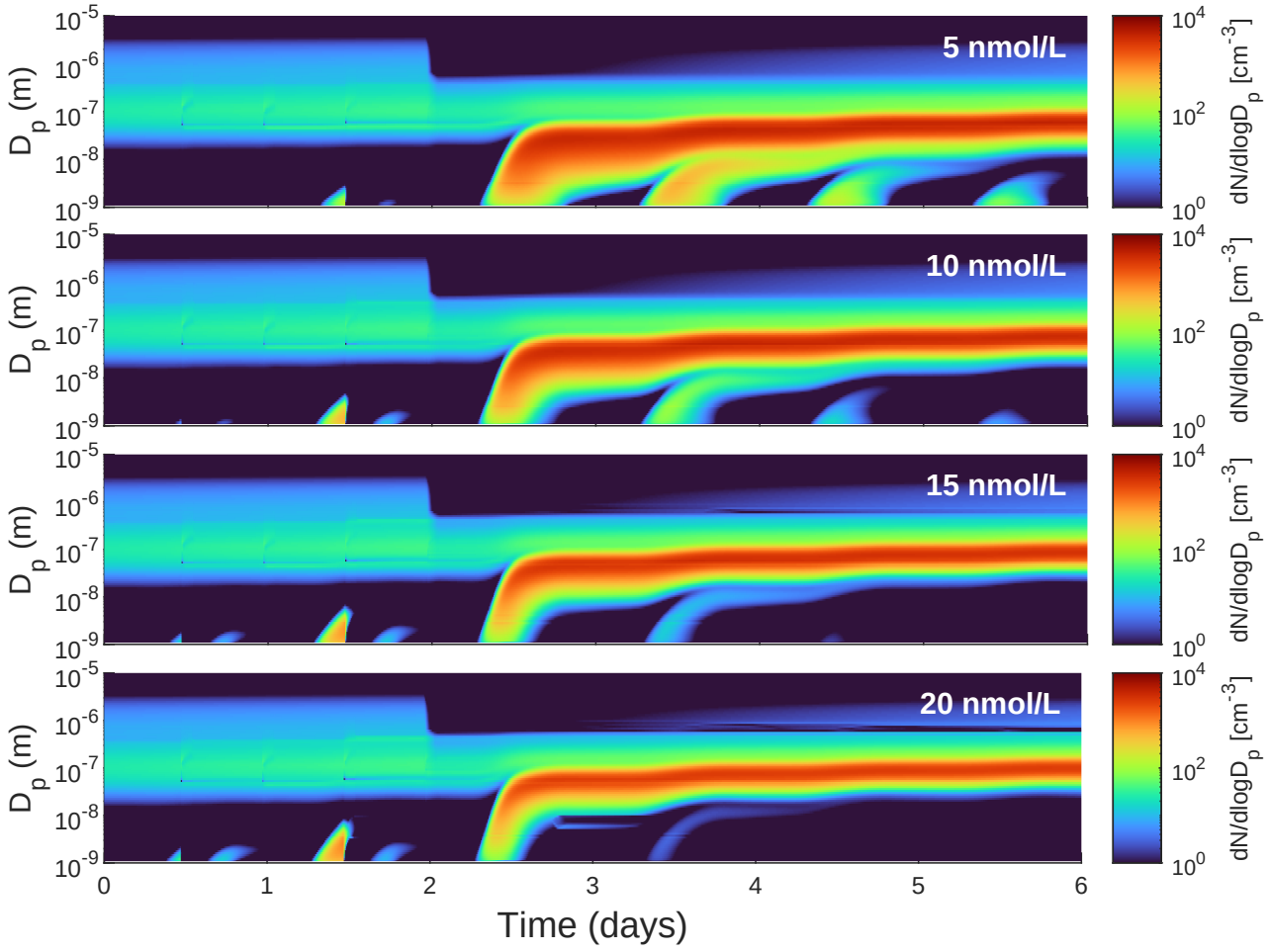

Figure S54. Aerosol particle number size distributions throughout the full simulation period at varying DMS sea surface concentrations ranging from 5 nM to 20 nM.

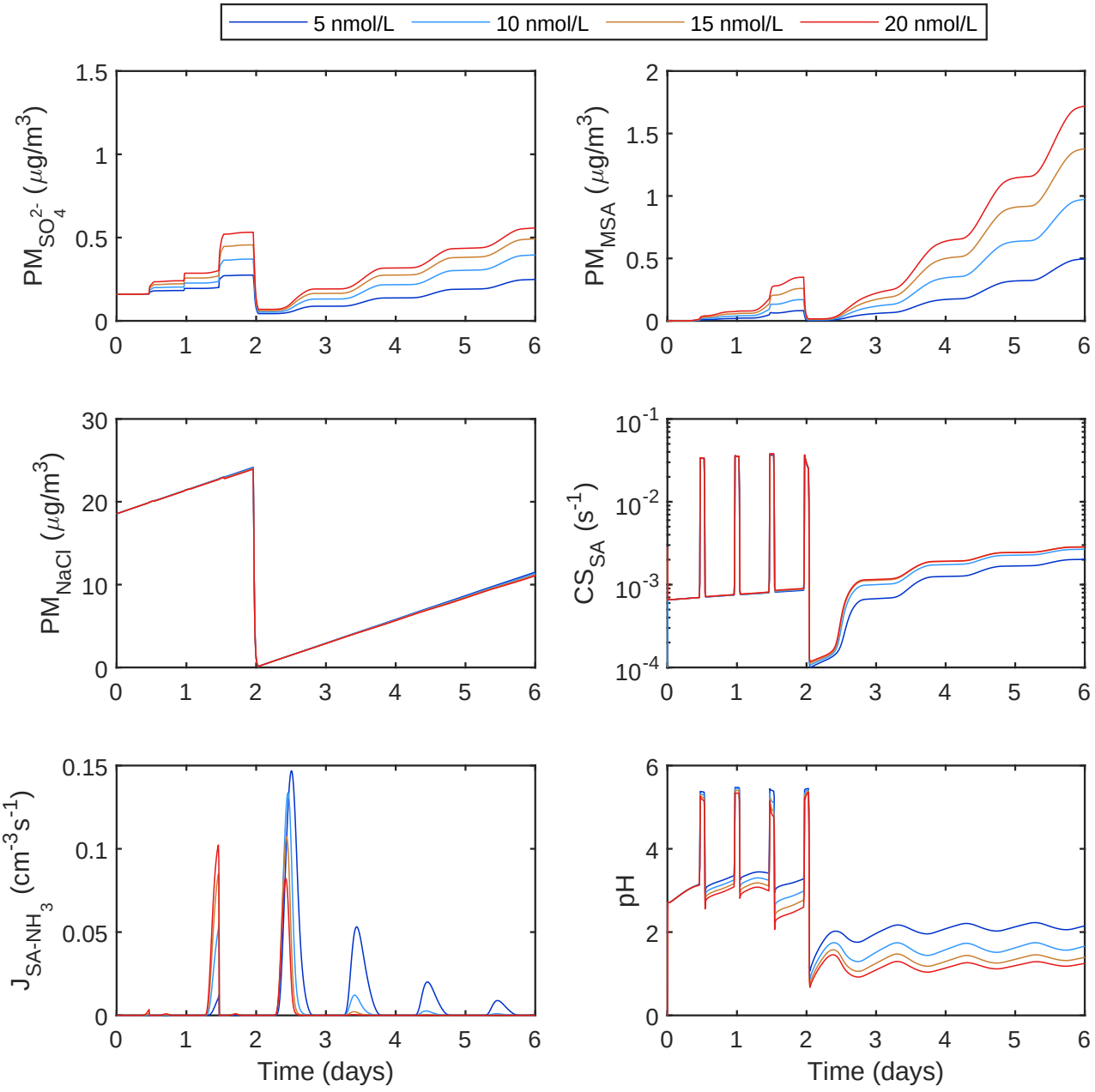

Figure S55. Total SO_4^{2-}, MSA and NaCl PM along with the SA condensation sink, SA-NH_3 driven nucleation rate and bulk pH at varying DMS sea surface concentrations ranging from 5 nM to 20 nM.

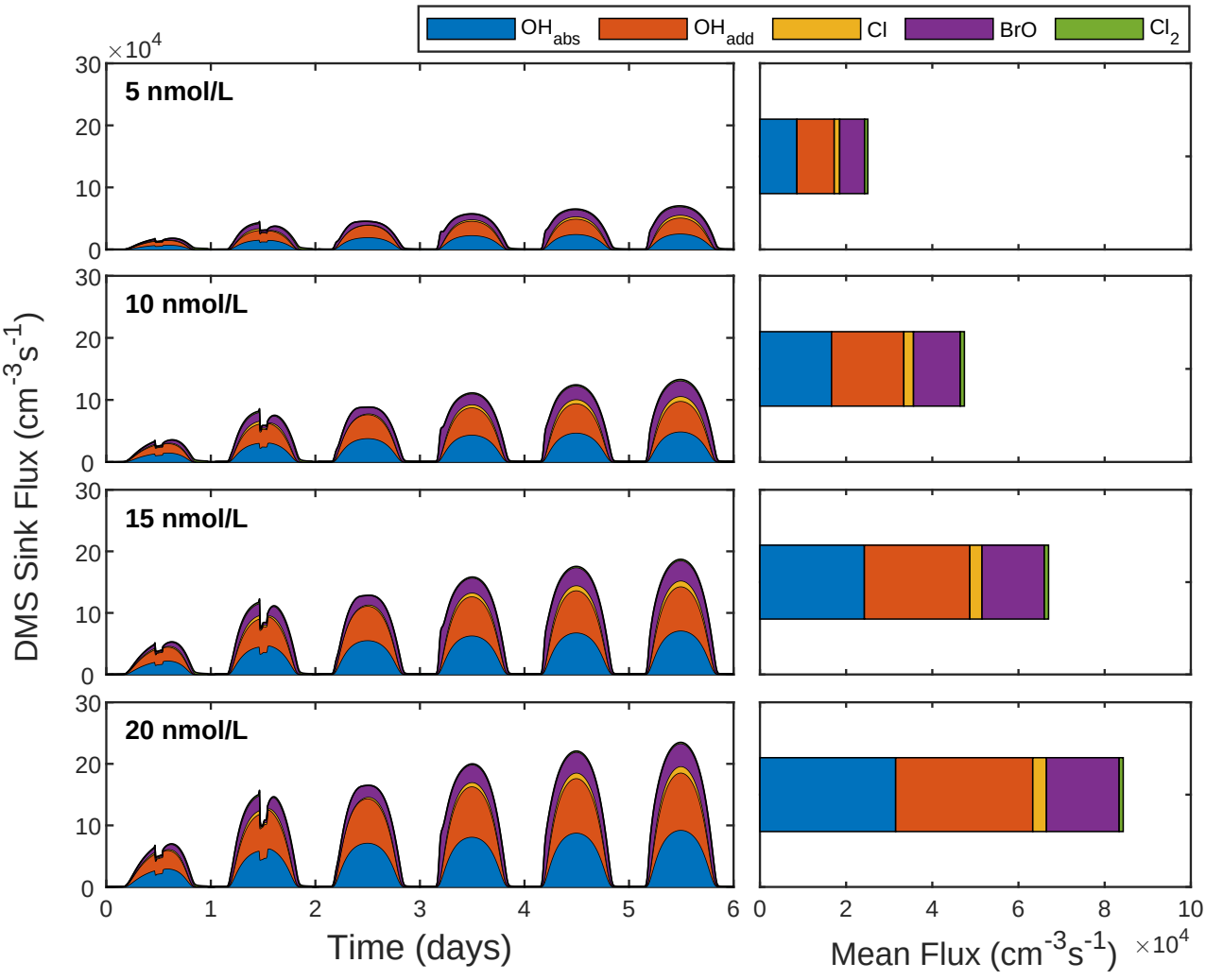

Figure S56. DMS sink flux driven by the reaction with OH (addition), OH (abstraction), Cl, Bro and Cl_2 at varying DMS sea surface concentrations ranging from 5 nM to 20 nM. Reactions that contribute < 1% of the total sink flux are not displayed in the figure.

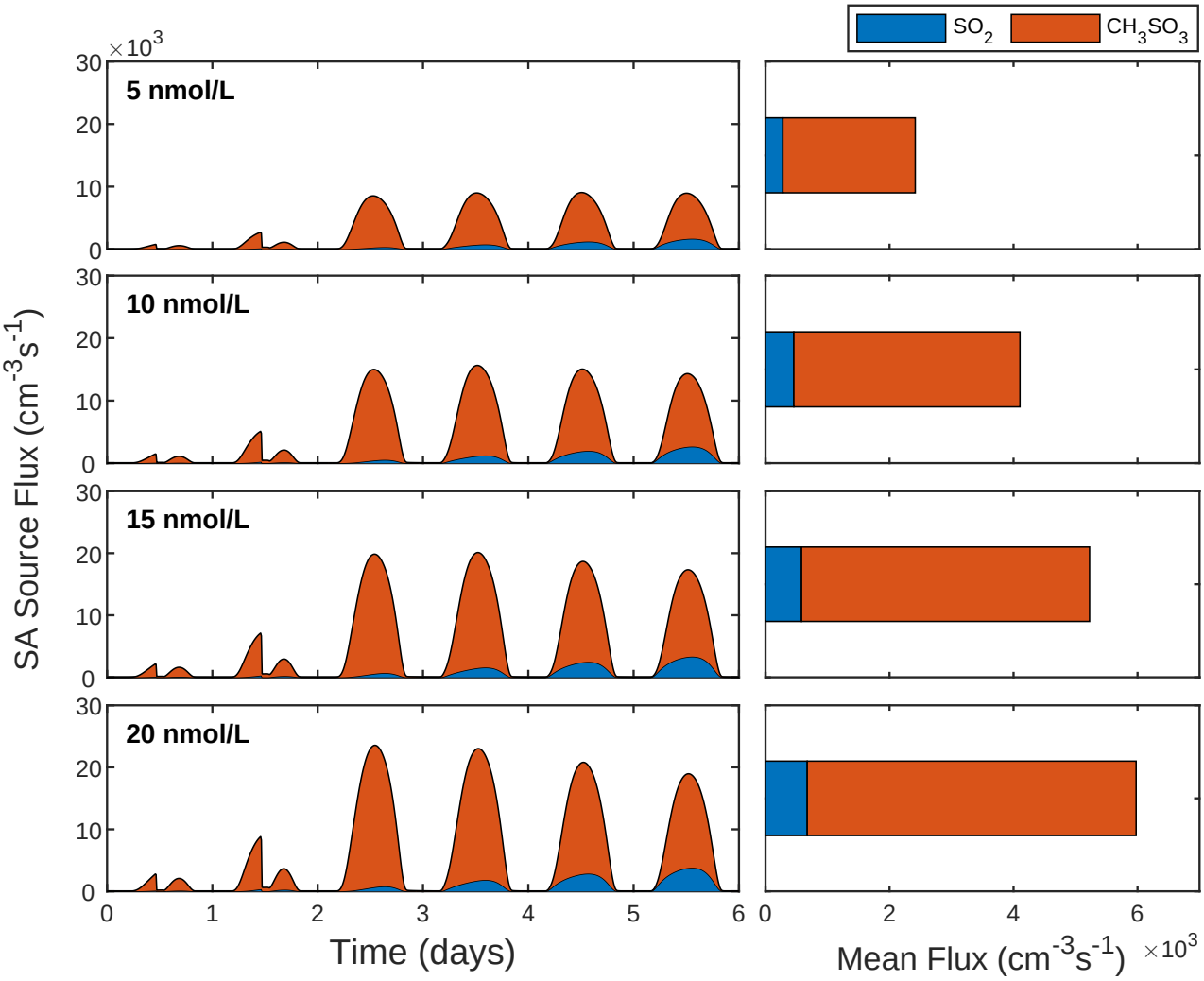

Figure S57. SA source flux from SO_2 and CH_3SO_3 at varying DMS sea surface concentrations ranging from 5 nM to 20 nM.

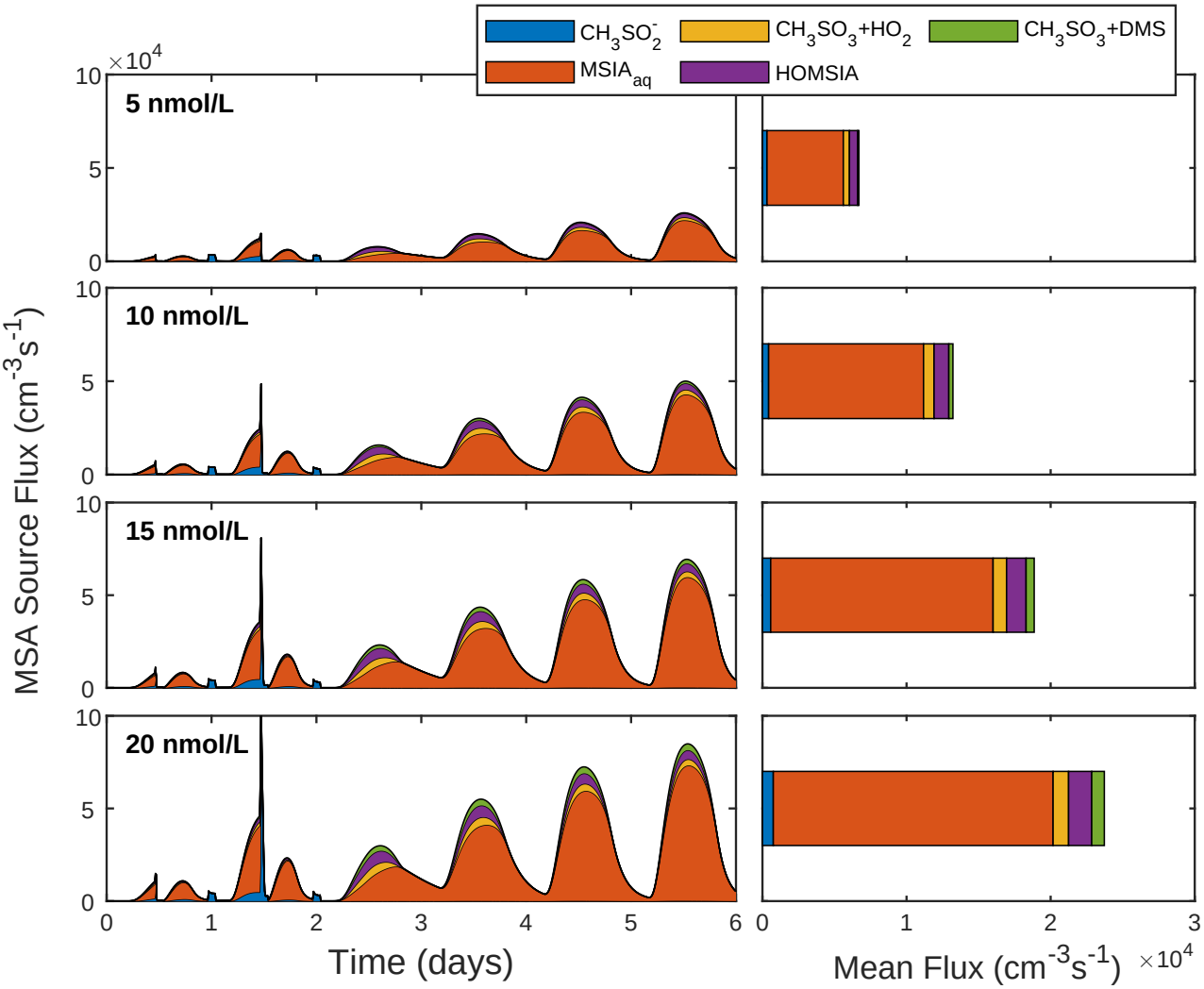

Figure S58. MSA source flux from $CH_3SO_2^-$ and $MSIA_{aq}$ in the aqueous-phase in addition to CH_3SO_3 via HO_2, CH_3SO_3 via DMS and HOMSIA in the gas-phase at varying DMS sea surface concentrations ranging from 5 nM to 20 nM.

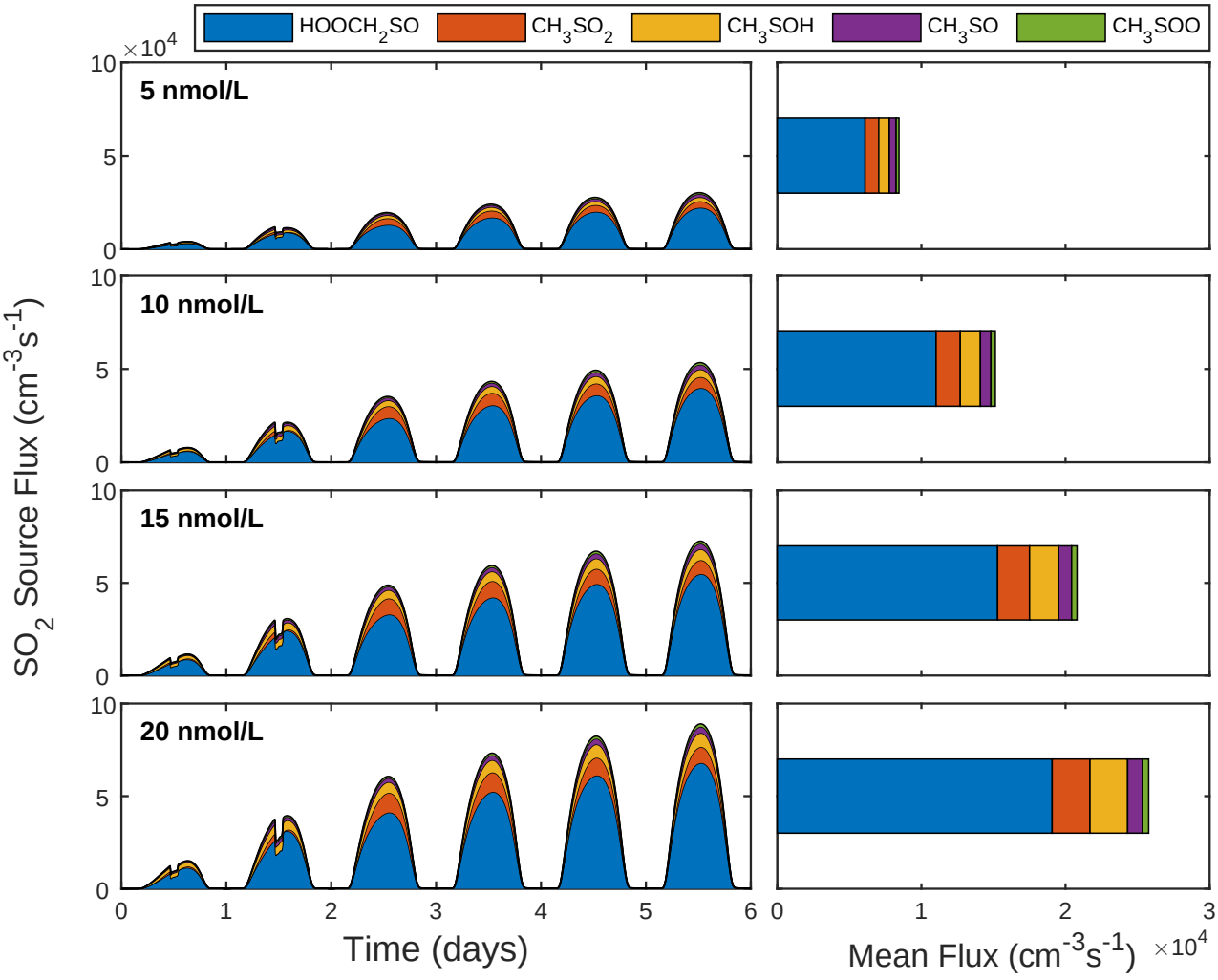

Figure S59. SO_2 source flux from $HOOCH_2SO$, CH_3SO_2, CH_3SOH, CH_3SO and CH_3SOO at varying DMS sea surface concentrations ranging from 5 nM to 20 nM. Reactions that contribute < 1% of the total source flux are not displayed in the figure.

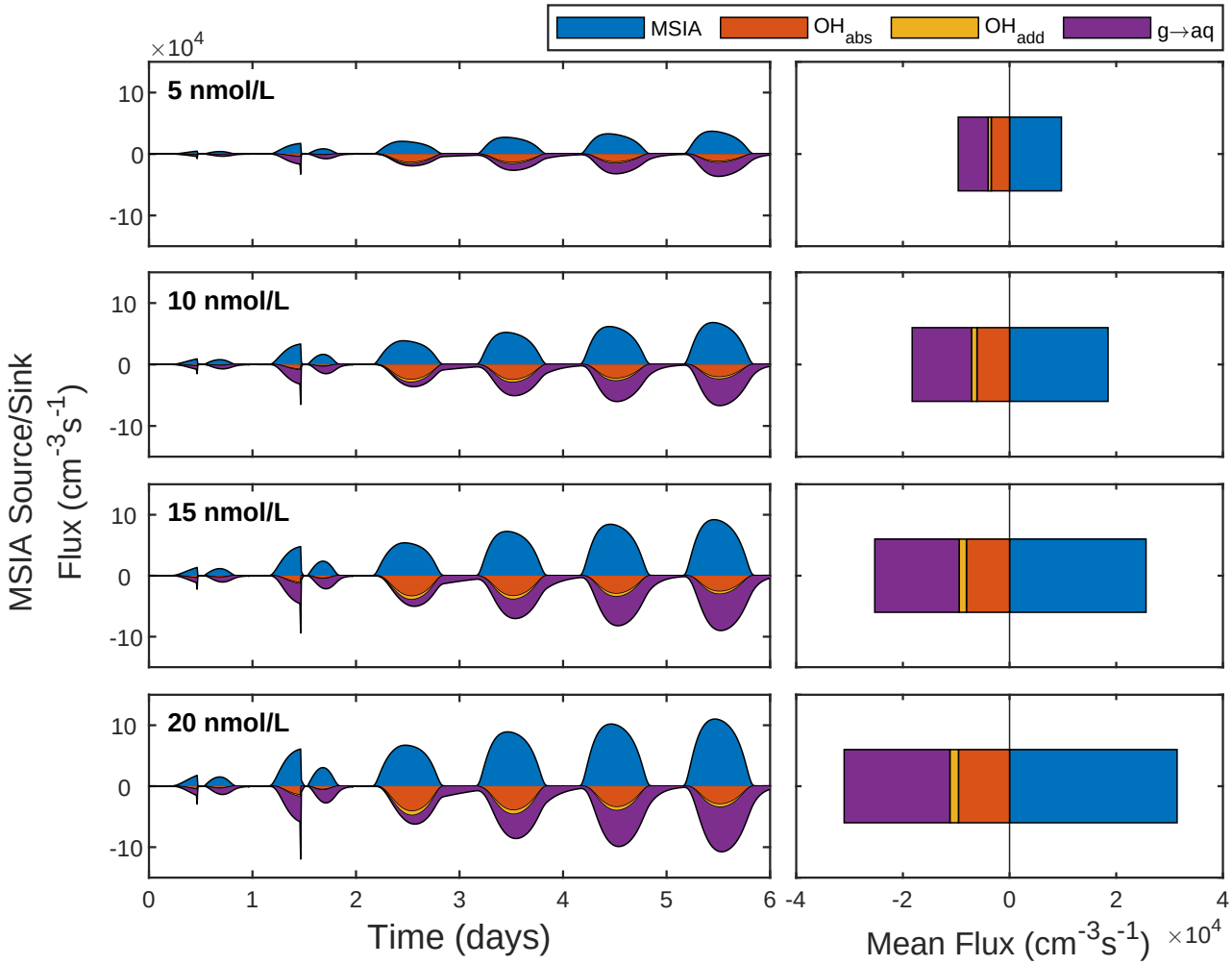

Figure S60. MSIA source/sink flux from DMSO and via reaction with OH (abstraction), OH (addition) and gas-aqueous phase uptake at varying DMS sea surface concentrations ranging from 5 nM to 20 nM. Reactions that contribute < 1% of the total source/sink flux are not displayed in the figure.

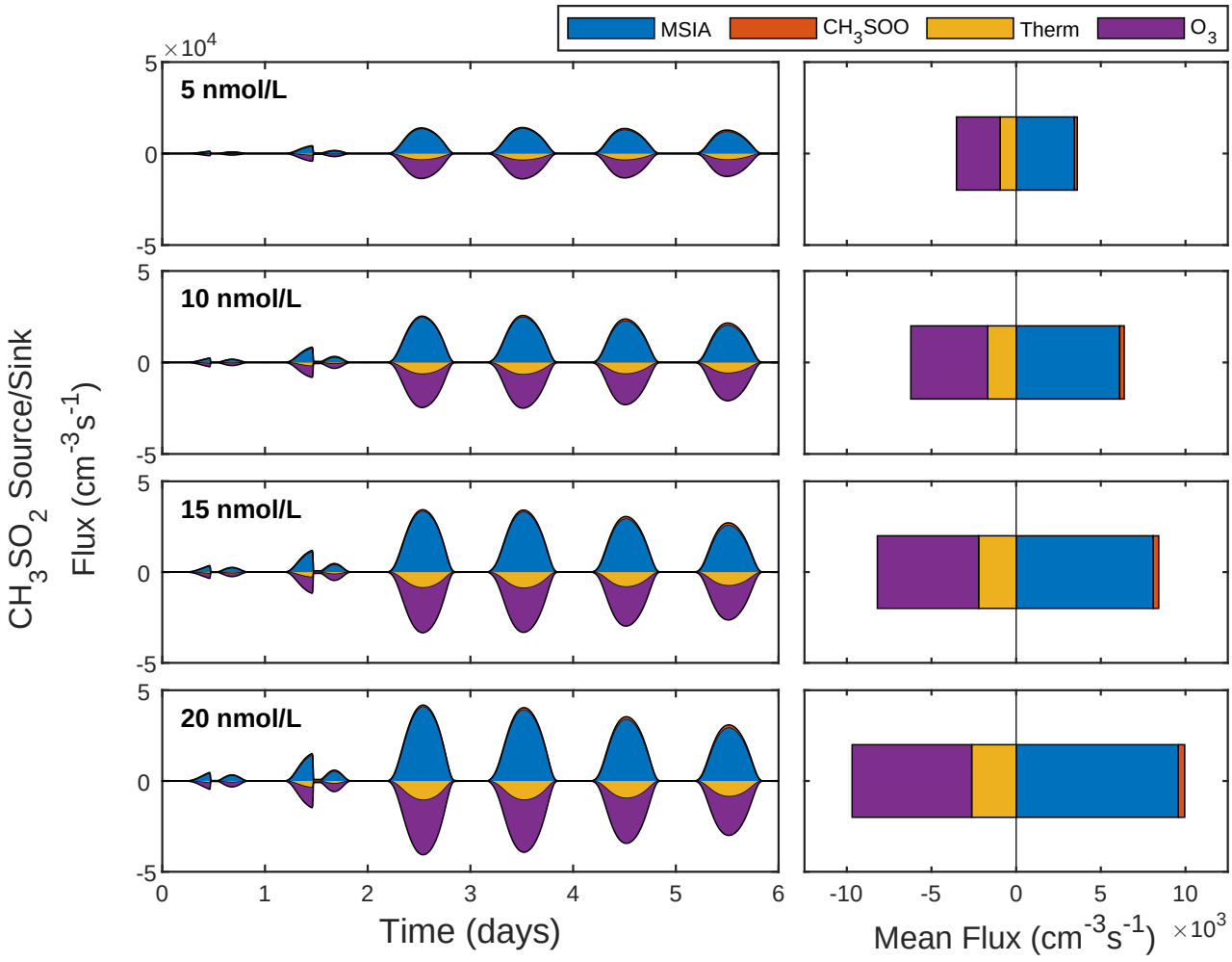

Figure S61. CH_3SO_2 source/sink flux from MSIA, CH_3SOO and via thermal decomposition and reaction with O_3 at varying DMS sea surface concentrations ranging from 5 nM to 20 nM. Reactions that contribute < 1% of the total source/sink flux are not displayed in the figure.

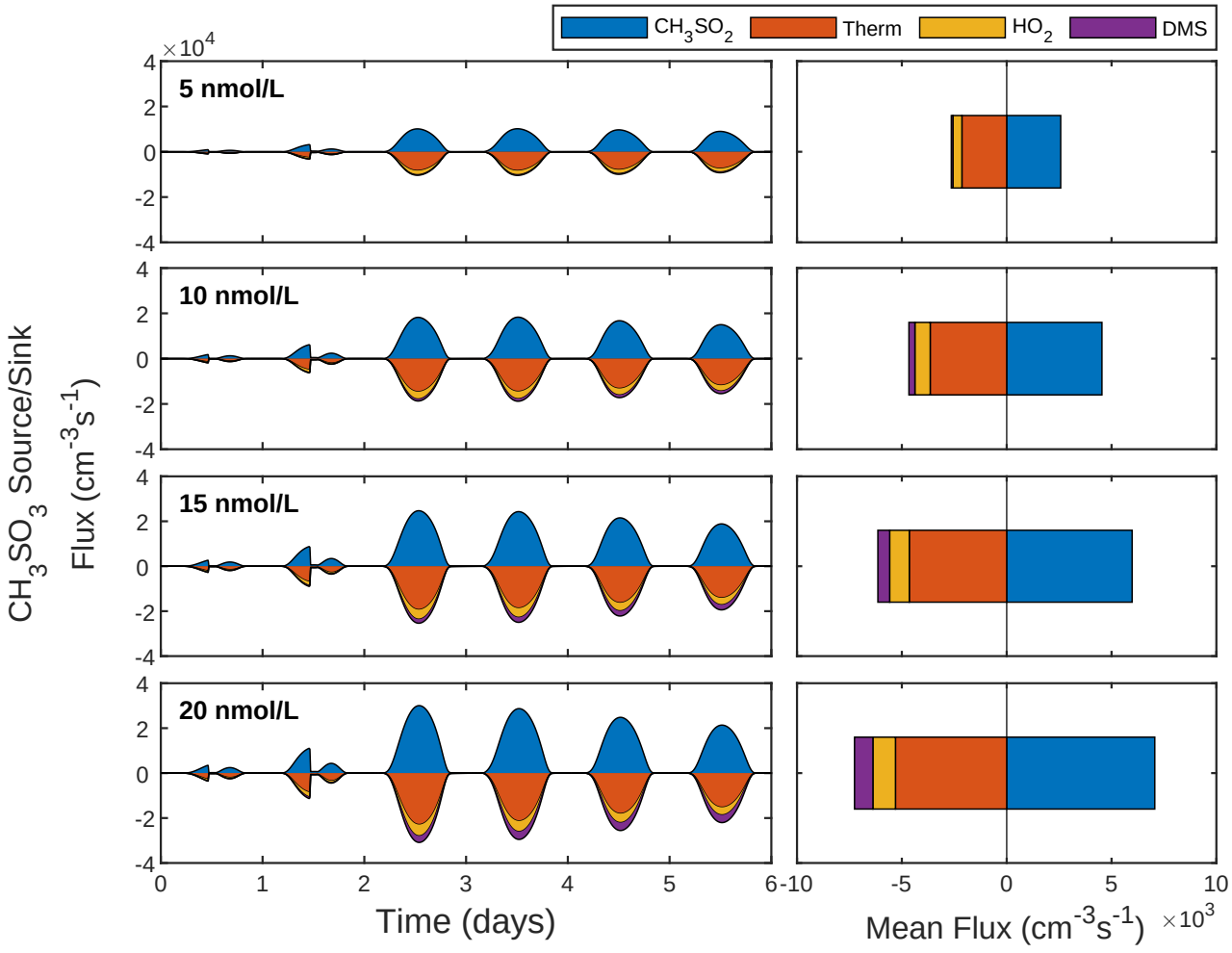

Figure S62. CH_3SO_3 source/sink flux from CH_3SO_2, via thermal decomposition and reaction with HO_2 and DMS at varying DMS sea surface concentrations ranging from 5 nM to 20 nM. Reactions that contribute < 1% of the total source/sink flux are not displayed in the figure.

S9 NH_x sea surface concentration sensitivity runs

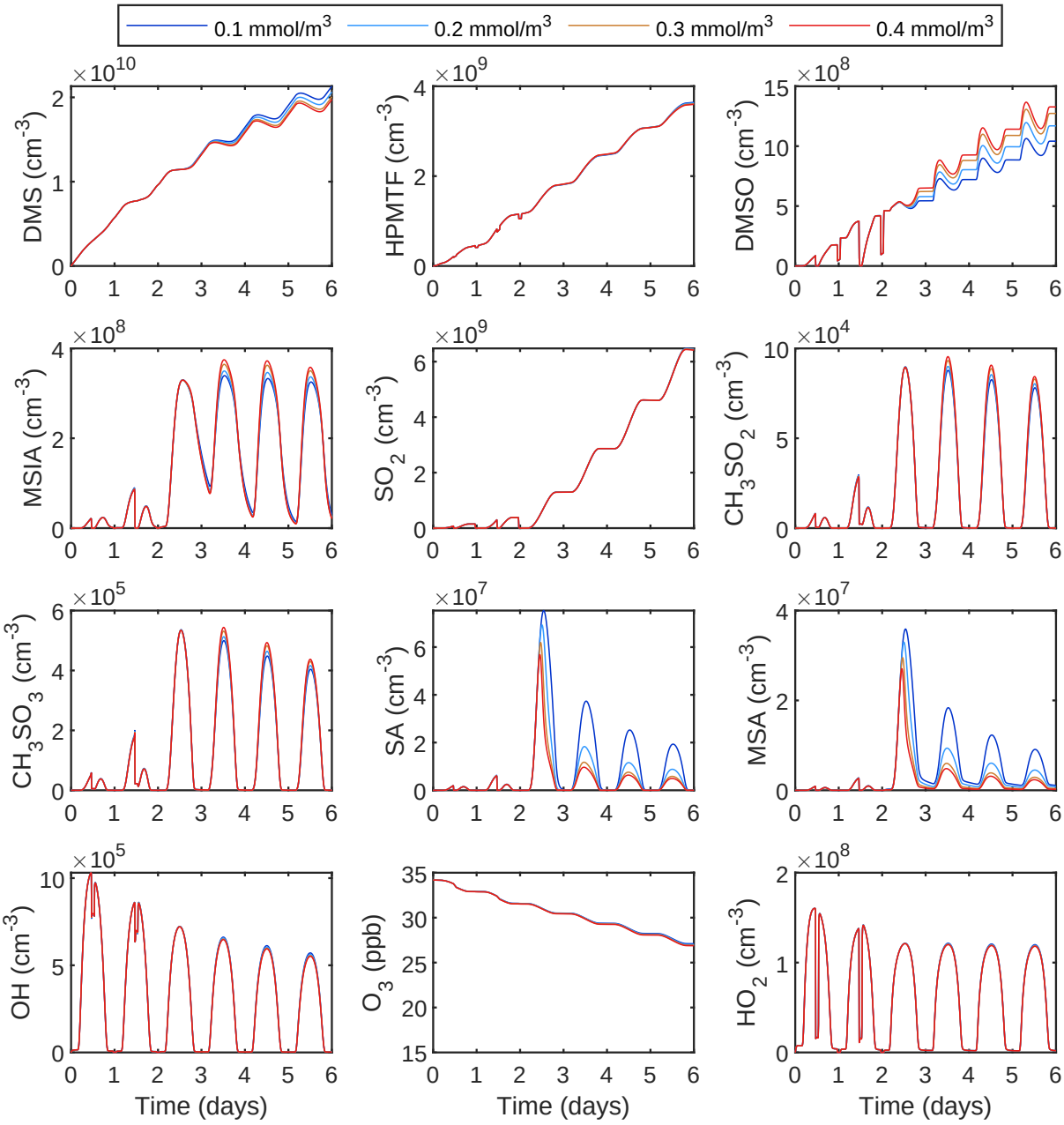

Figure S63. Concentrations of key gas-phase species at varying NH_x sea surface concentrations ranging from 0.1 $\mathrm{mmol/m^3}$ to 0.4 $\mathrm{mmol/m^3}$.

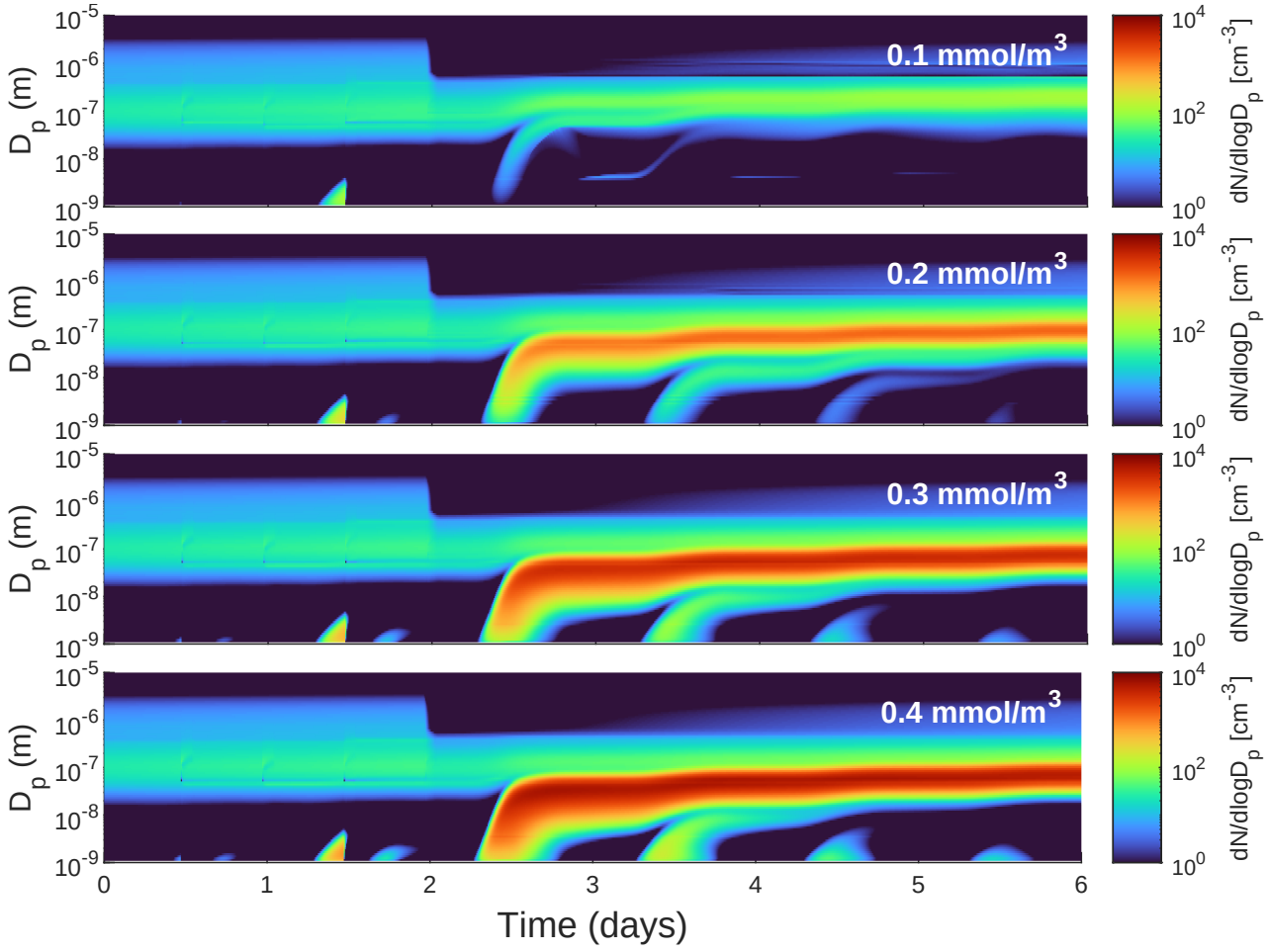

Figure S64. Aerosol particle number size distributions throughout the full simulation period at varying NH_x sea surface concentrations ranging from 0.1 $\mathrm{mmol/m^3}$ to 0.4 $\mathrm{mmol/m^3}$.

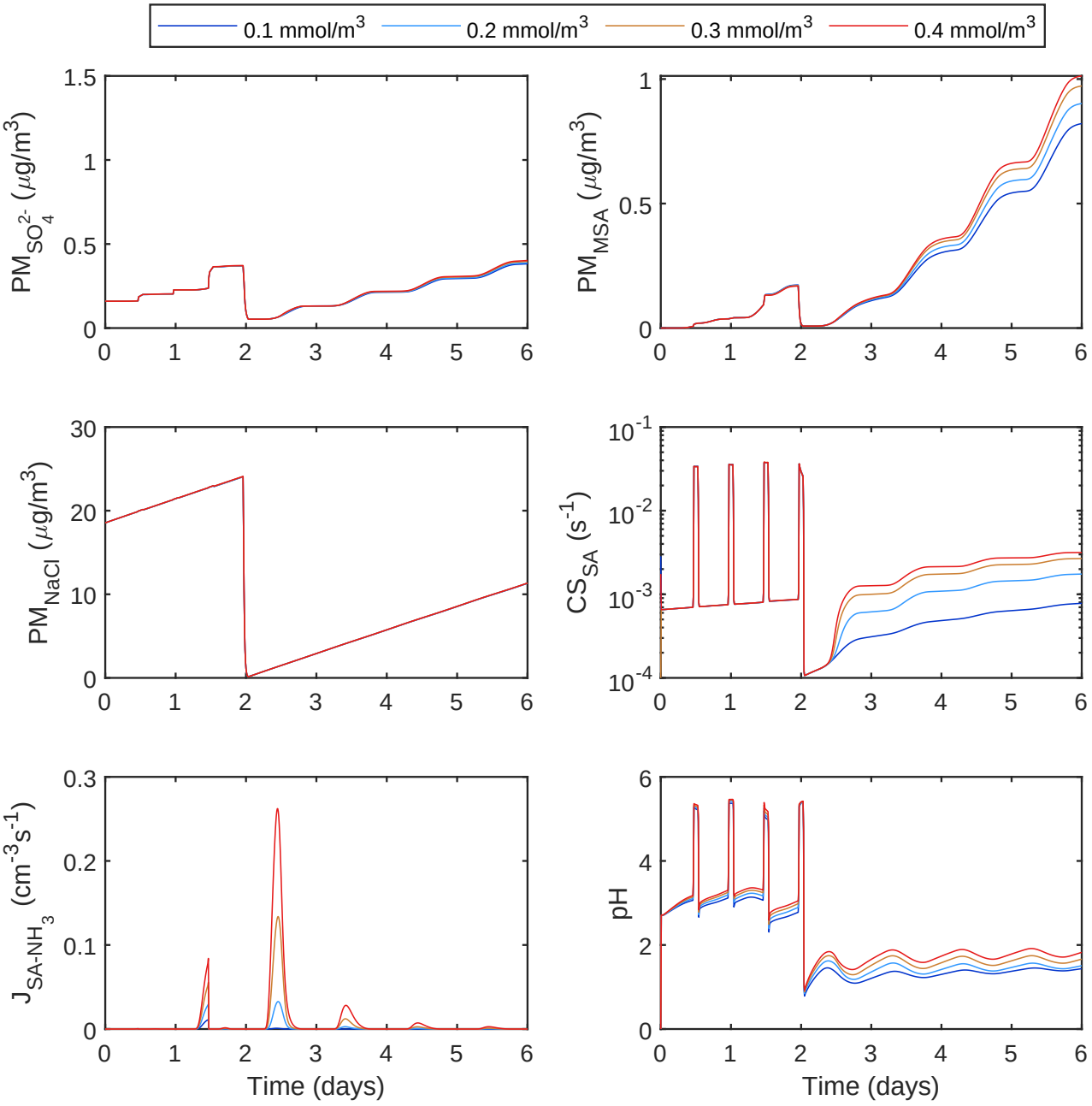

Figure S65. Total SO_4^{2-}, MSA and NaCl PM along with the SA condensation sink, SA-NH_3 driven nucleation rate and bulk pH at varying NH_x sea surface concentrations ranging from 0.1 $mmol/m^3$ to 0.4 $mmol/m^3$.

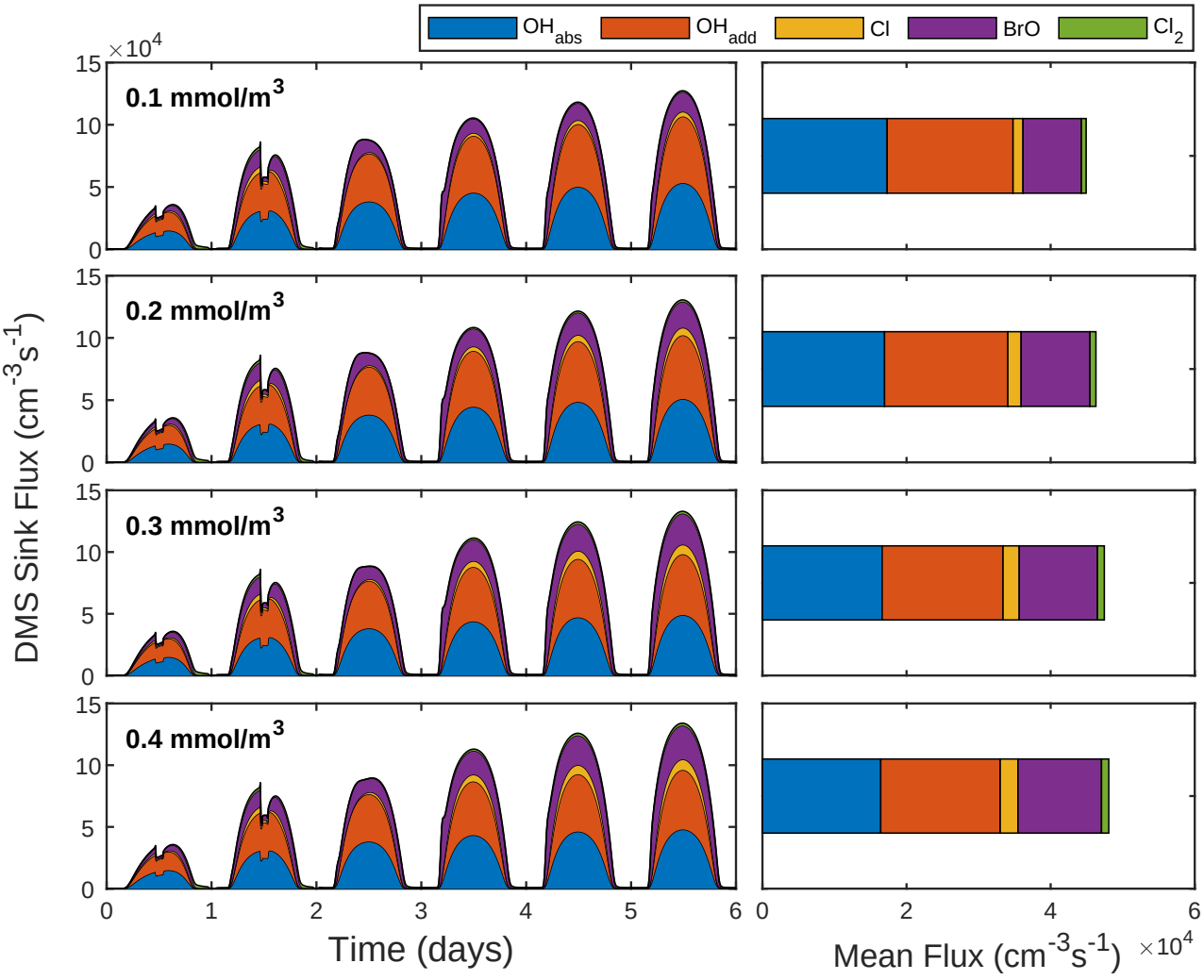

Figure S66. DMS sink flux driven by the reaction with OH (addition), OH (abstraction), Cl, Bro and Cl_2 at varying NH_x sea surface concentrations ranging from 0.1 $\mathrm{mmol/m^3}$ to 0.4 $\mathrm{mmol/m^3}$. Reactions that contribute < 1% of the total sink flux are not displayed in the figure.

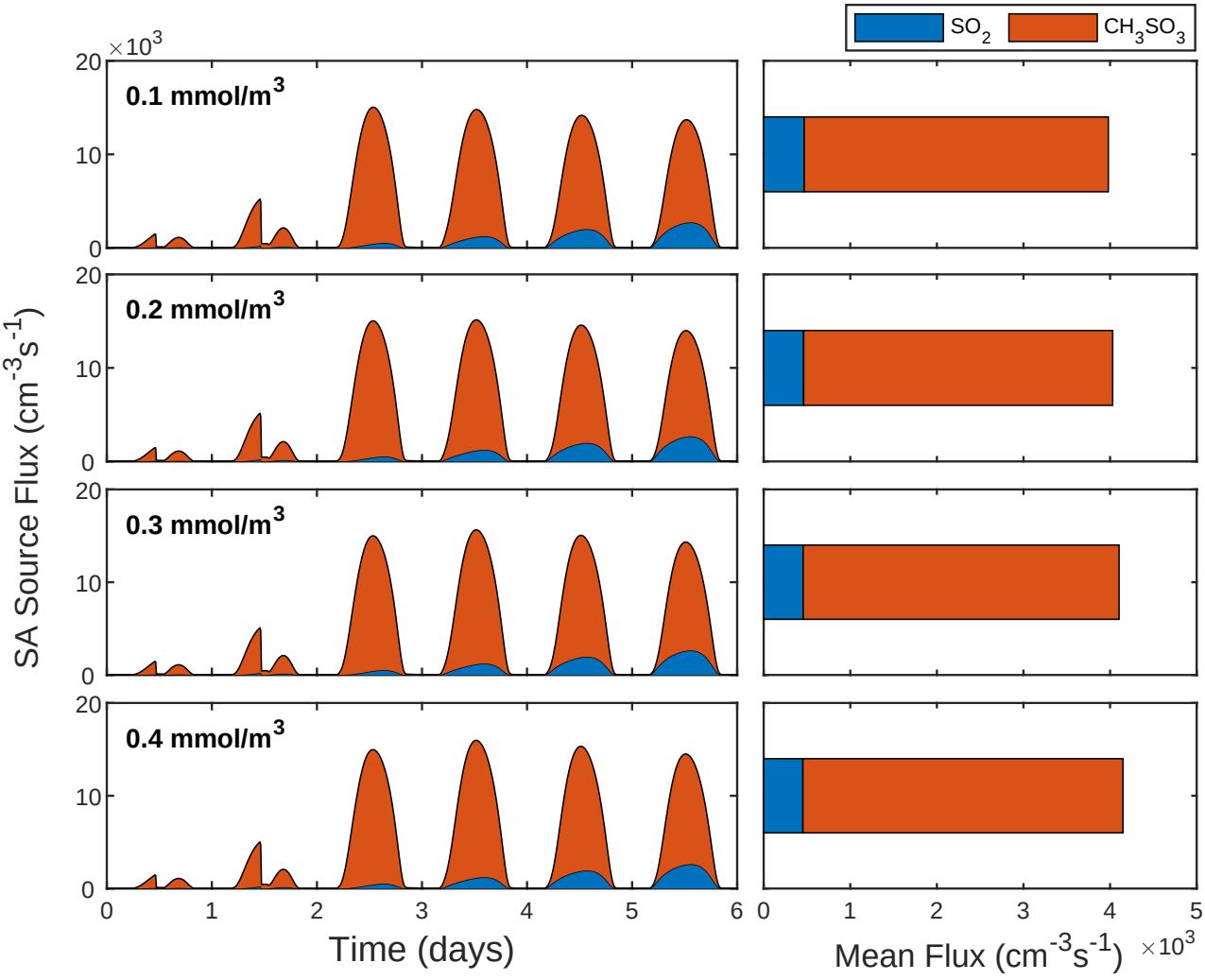

Figure S67. SA source flux from SO_2 and CH_3SO_3 at varying NH_x sea surface concentrations ranging from 0.1 $mmol/m^3$ to 0.4 $mmol/m^3$.

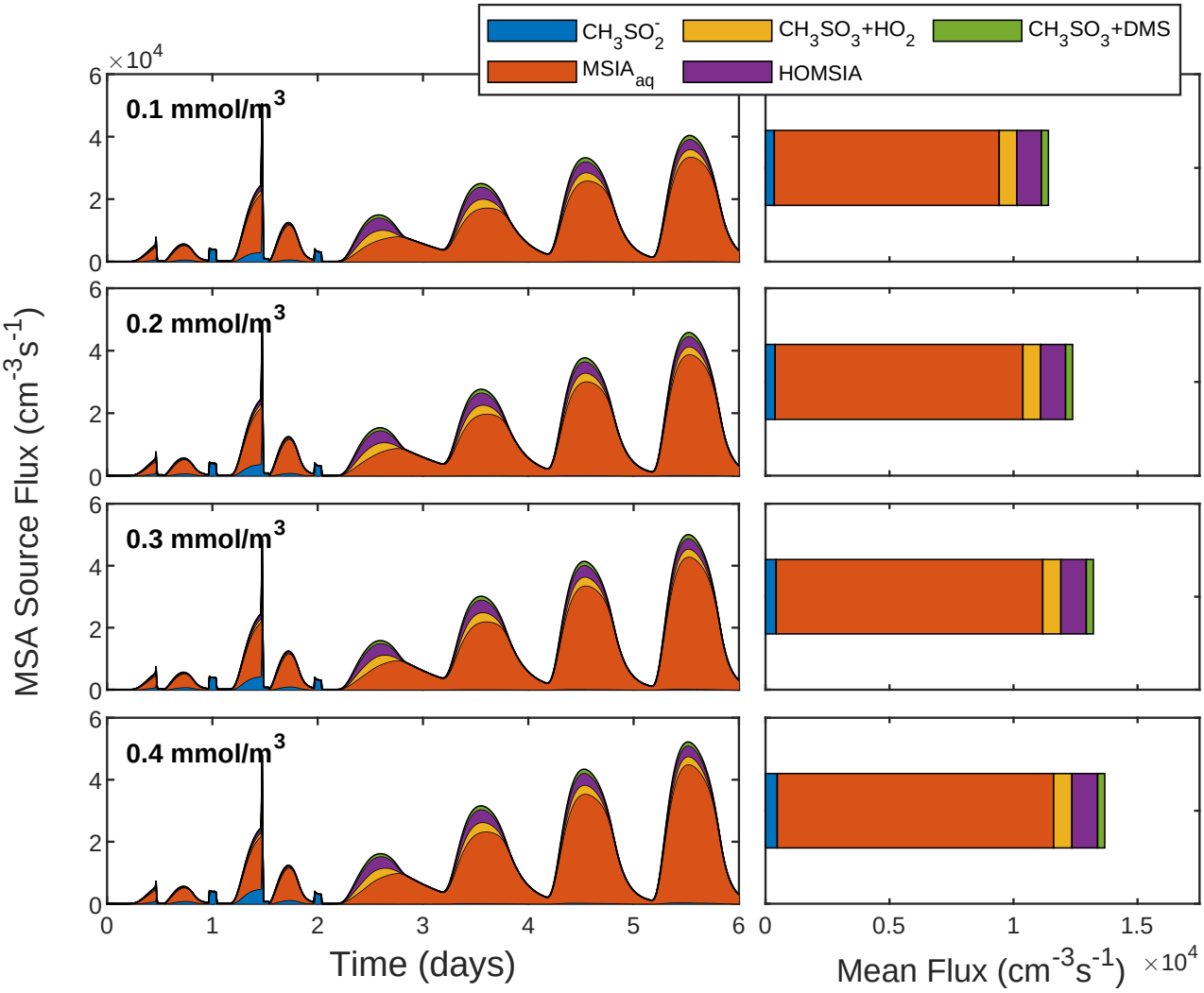

Figure S68. MSA source flux from $CH_3SO_2^-$ and $MSIA_{aq}$ in the aqueous-phase in addition to CH_3SO_3 via HO_2, CH_3SO_3 via DMS and HOMSIA in the gas-phase at varying NH_x sea surface concentrations ranging from 0.1 $mmol/m^3$ to 0.4 $mmol/m^3$.

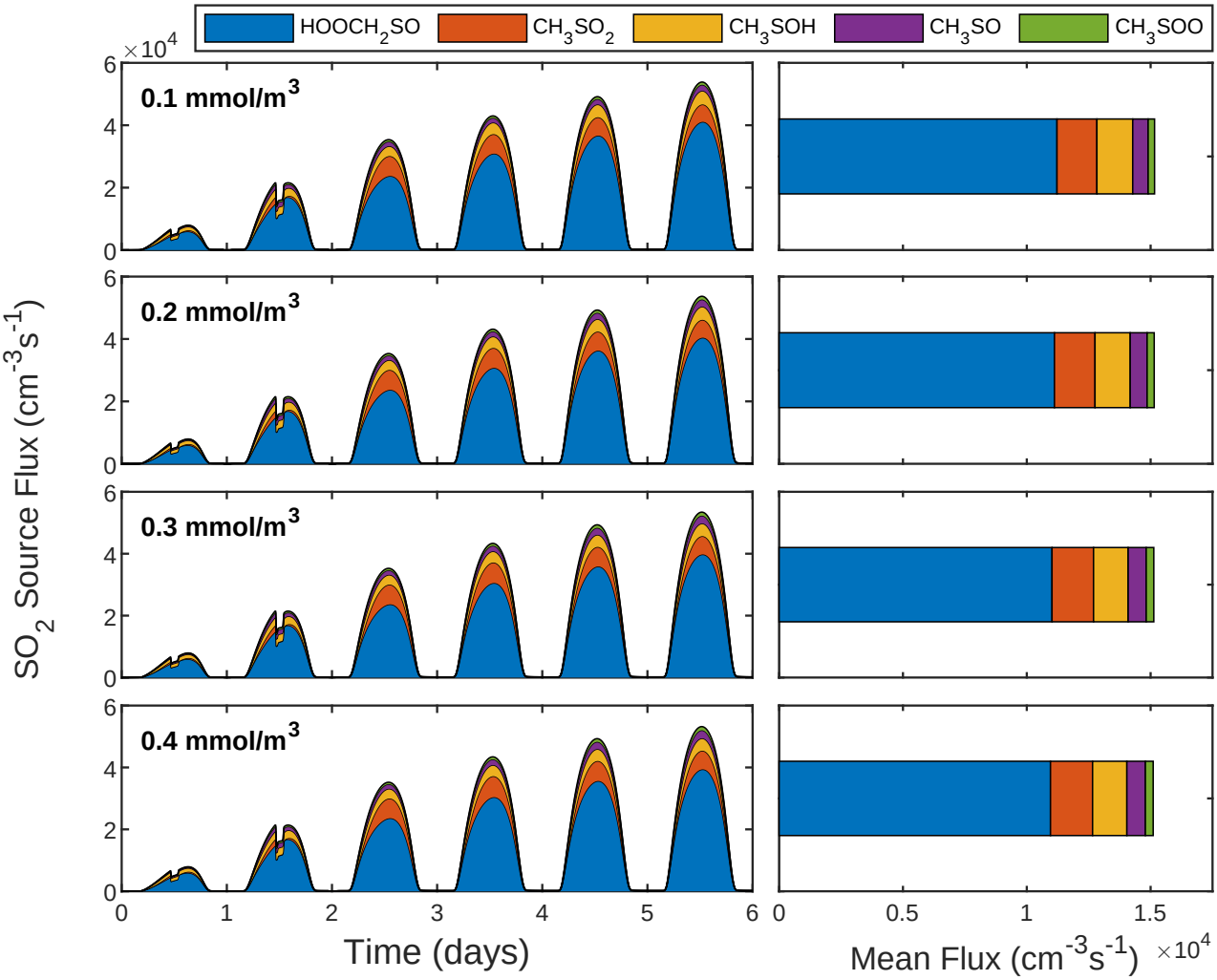

Figure S69. SO_2 source flux from $HOOCH_2SO$, CH_3SO_2, CH_3SOH, CH_3SO and CH_3SOO at varying NH_x sea surface concentrations ranging from 0.1 $\mathrm{mmol/m^3}$ to 0.4 $\mathrm{mmol/m^3}$. Reactions that contribute < 1% of the total source flux are not displayed in the figure.

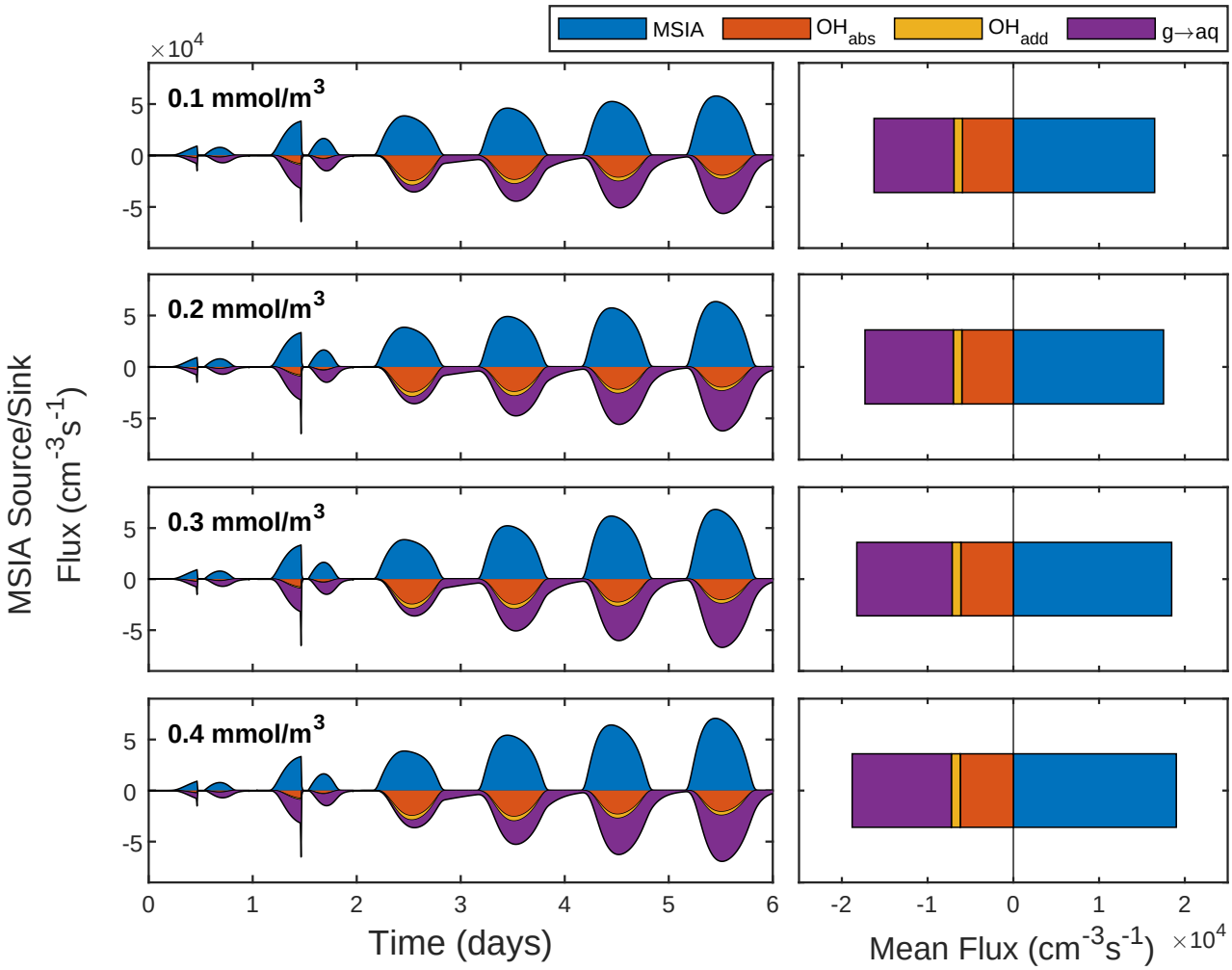

Figure S70. MSIA source/sink flux from DMSO and via reaction with OH (abstraction), OH (addition) and gas-aqueous phase uptake at varying NH_x sea surface concentrations ranging from 0.1 $mmol/m^3$ to 0.4 $mmol/m^3$. Reactions that contribute < 1% of the total source/sink flux are not displayed in the figure.

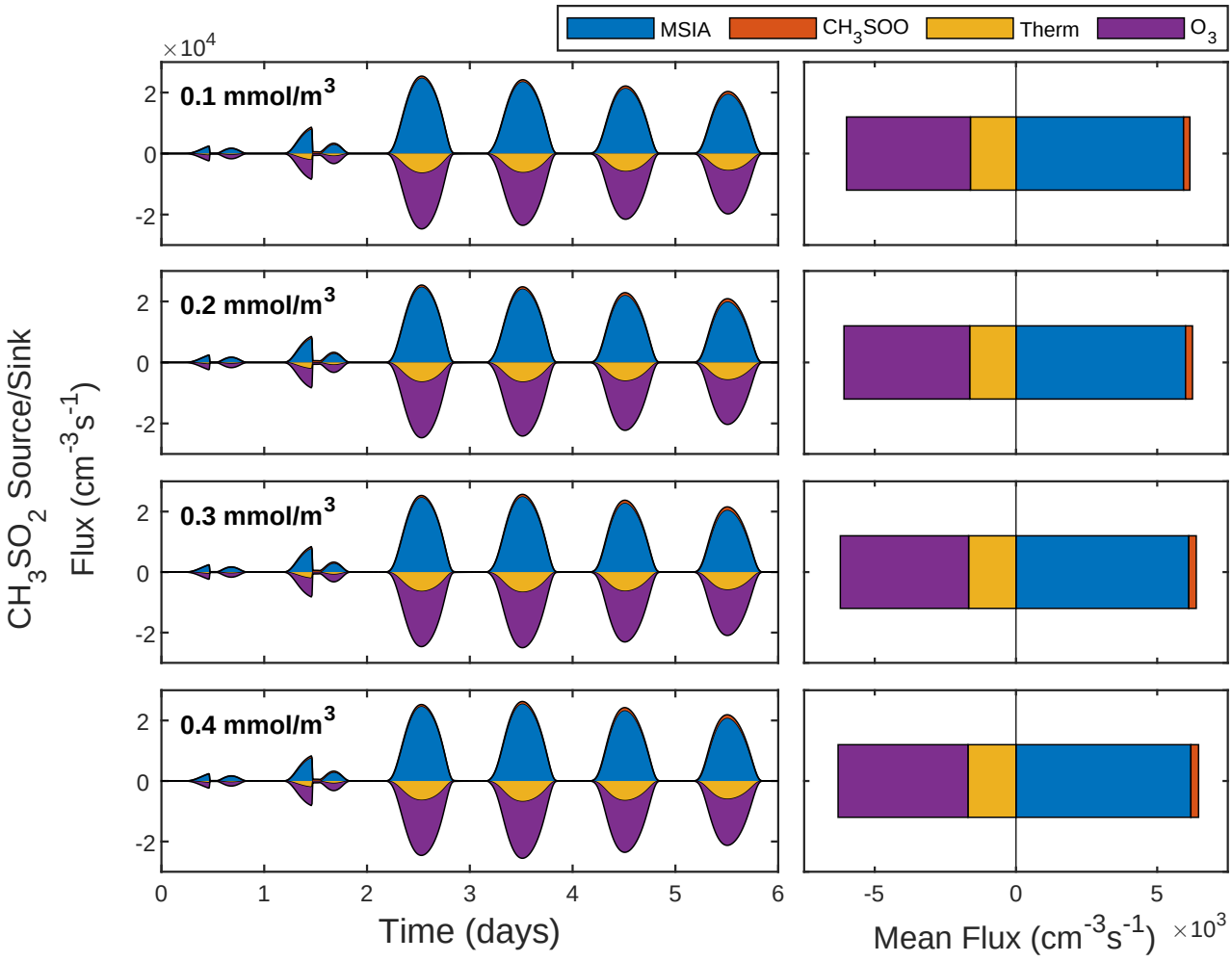

Figure S71. CH_3SO_2 source/sink flux from MSIA, CH_3SOO and via thermal decomposition and reaction with O_3 at varying NH_x sea surface concentrations ranging from 0.1 $\mathrm{mmol/m^3}$ to 0.4 $\mathrm{mmol/m^3}$. Reactions that contribute < 1% of the total source/sink flux are not displayed in the figure.

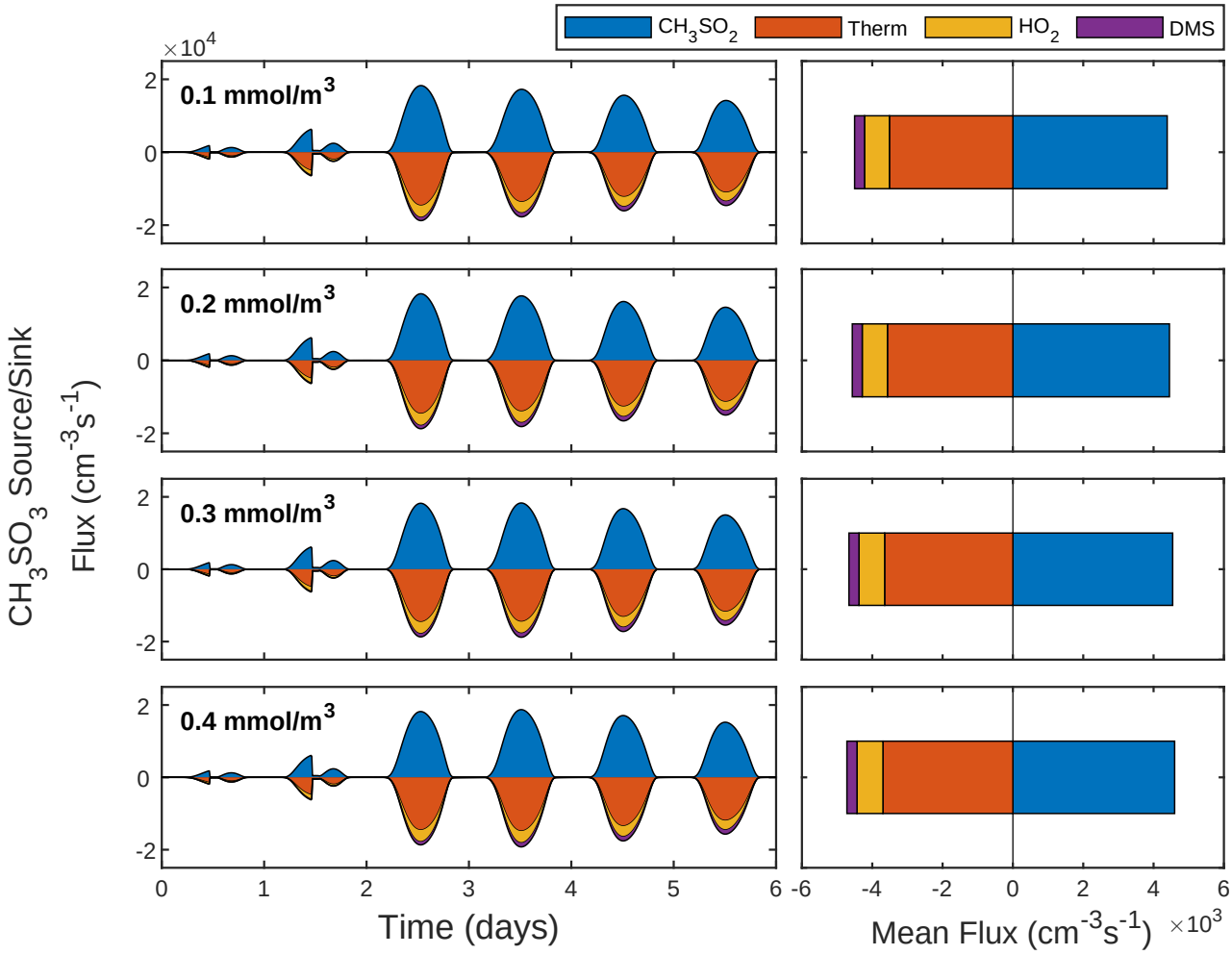

Figure S72. CH_3SO_3 source/sink flux from CH_3SO_2, via thermal decomposition and reaction with HO_2 and DMS at varying NH_x sea surface concentrations ranging from 0.1 $\mathrm{mmol/m^3}$ to 0.4 $\mathrm{mmol/m^3}$. Reactions that contribute < 1% of the total source/sink flux are not displayed in the figure.

S10 Cloudy conditions sensitivity runs

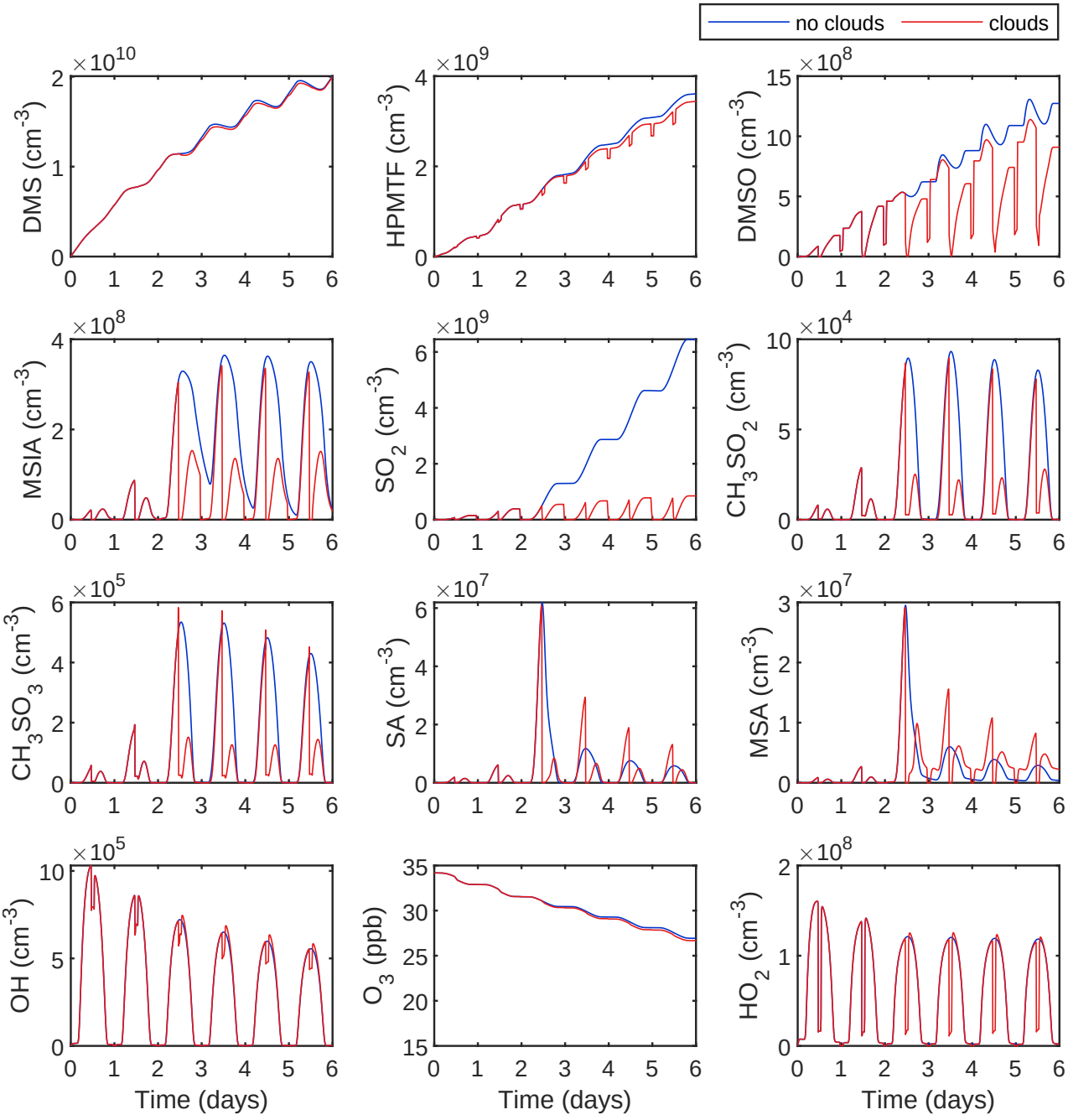

Figure S73. Concentrations of key gas-phase species during conditions with and without clouds.

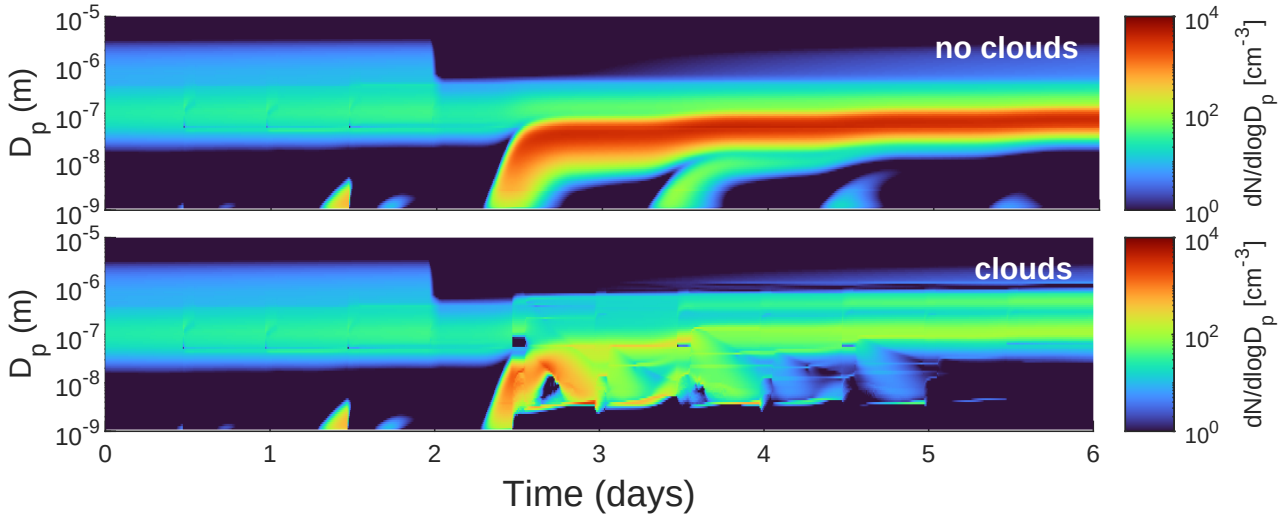

Figure S74. Aerosol particle number size distributions throughout the full simulation period during conditions with and without clouds.

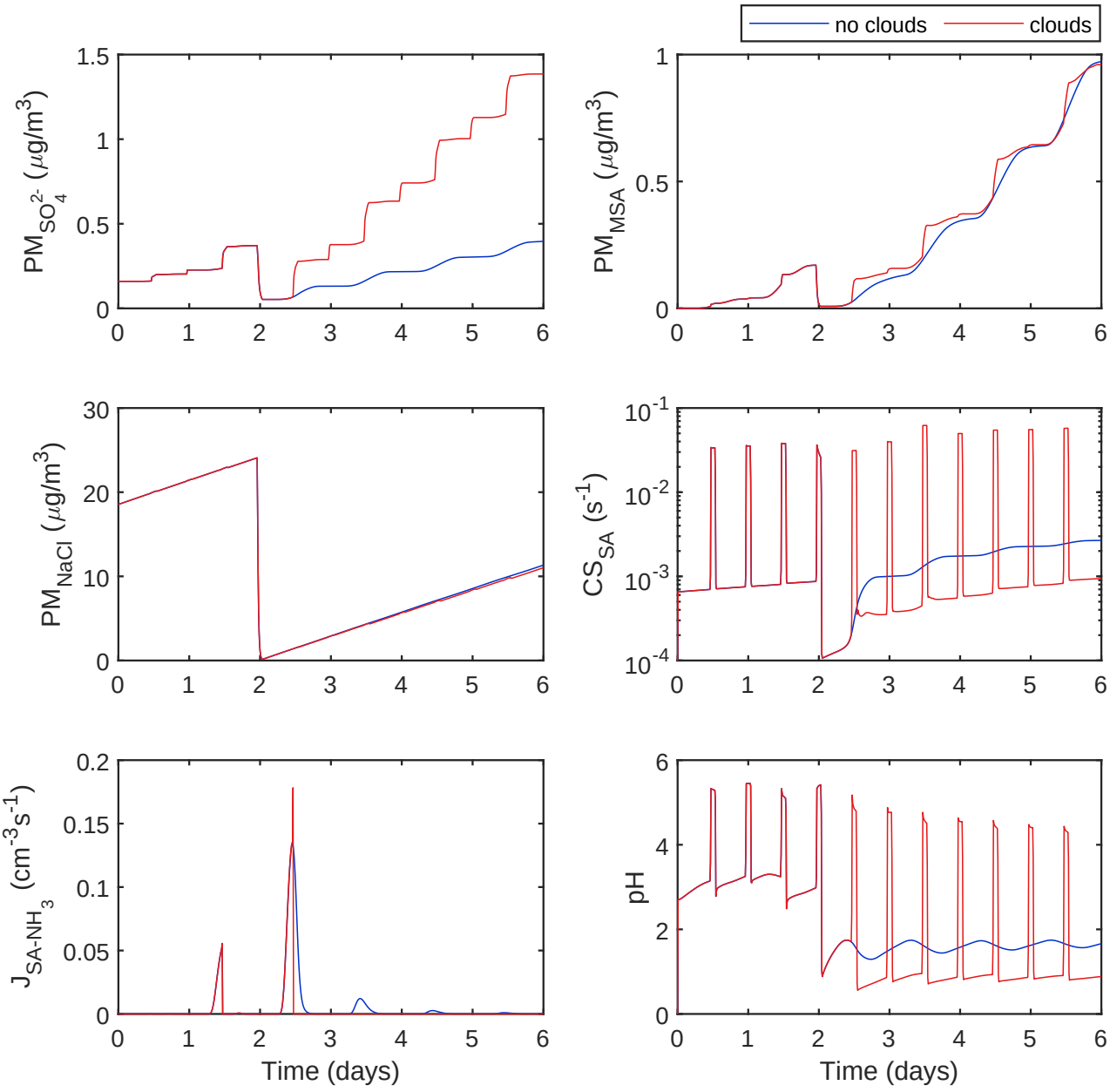

Figure S75. Total SO_4^{2-}, MSA and NaCl PM along with the SA condensation sink, SA-NH_3 driven nucleation rate and bulk pH during conditions with and without clouds.

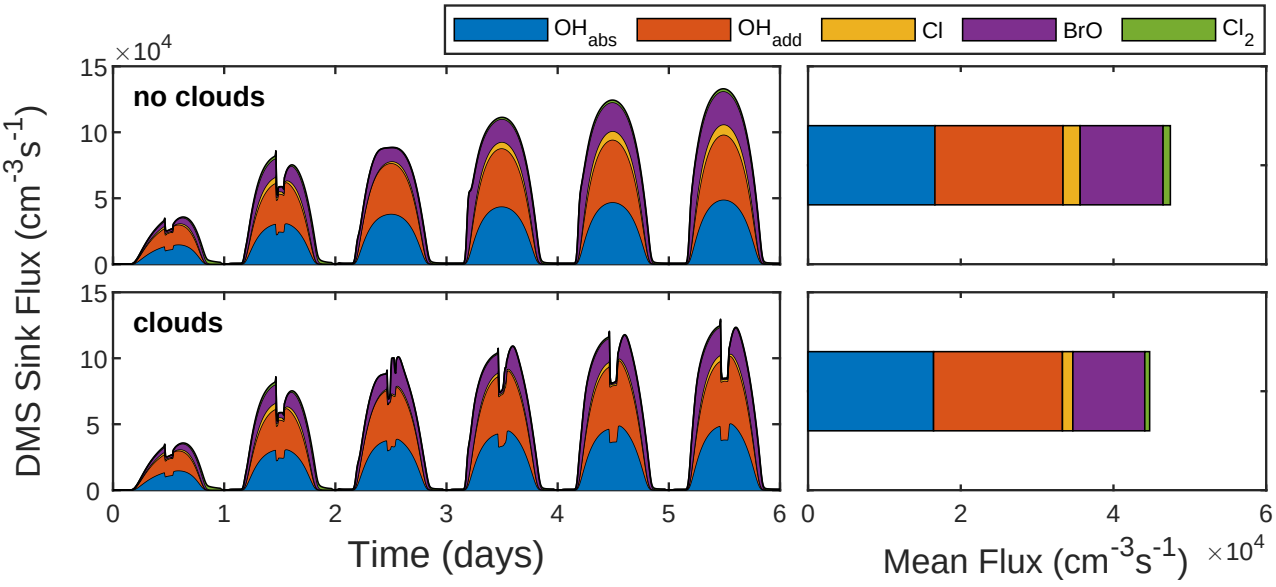

Figure S76. DMS sink flux driven by the reaction with OH (addition), OH (abstraction), Cl, Bro and Cl_2 during conditions with and without clouds. Reactions that contribute < 1% of the total sink flux are not displayed in the figure.

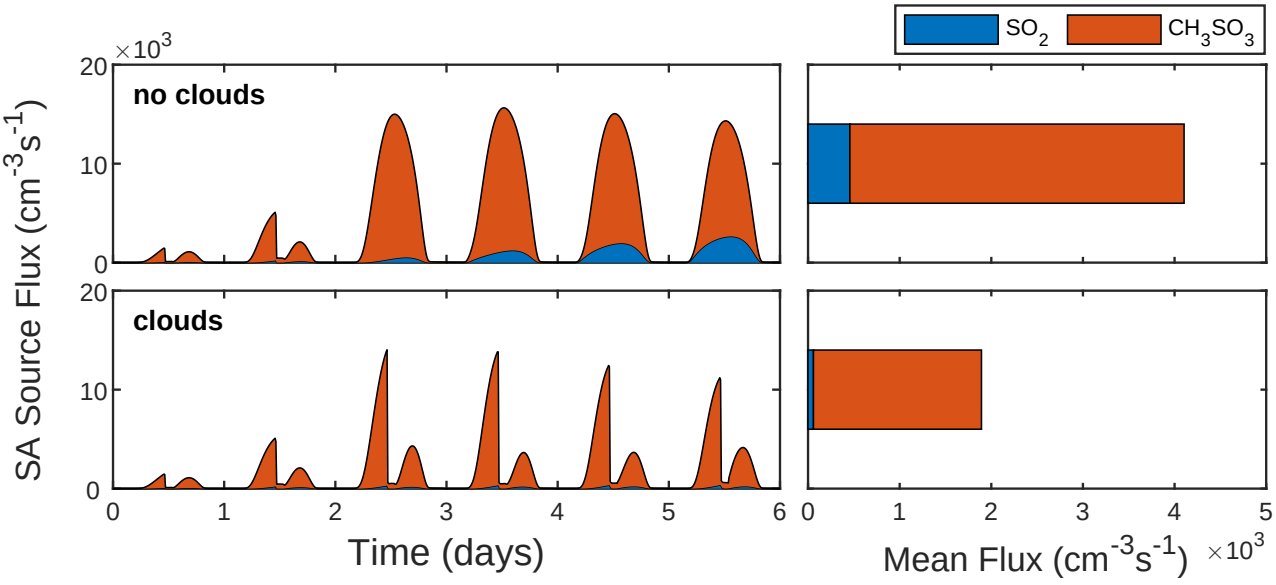

Figure S77. SA source flux from SO_2 and CH_3SO_3 during conditions with and without clouds.

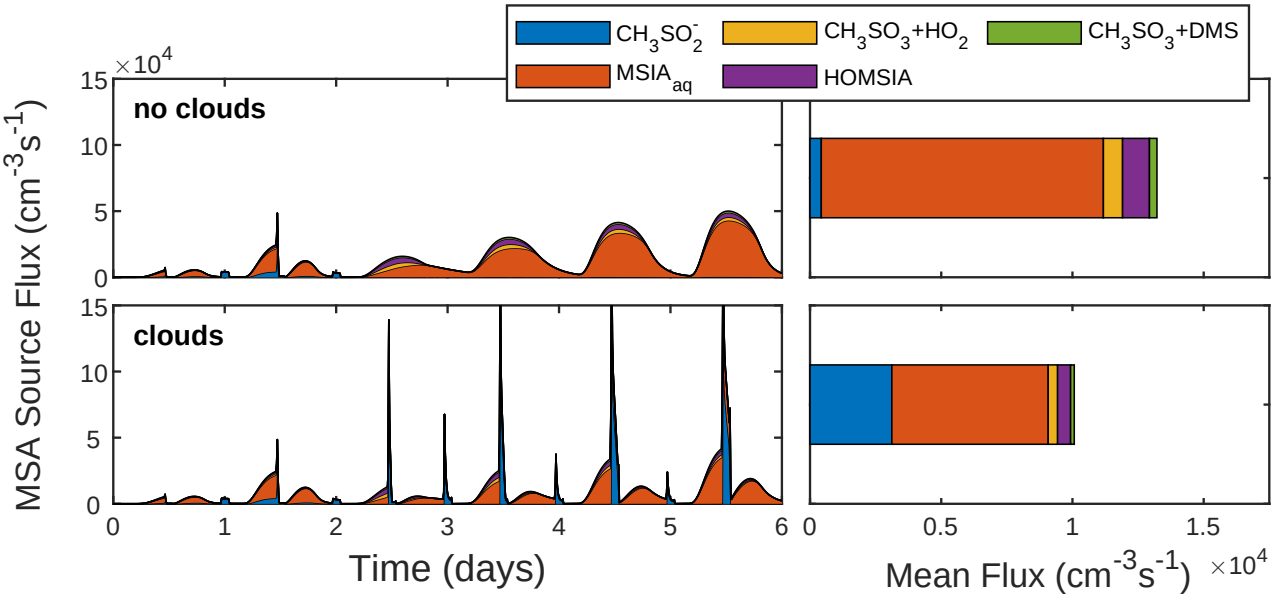

Figure S78. MSA source flux from $CH_3SO_2^-$ and $MSIA_{aq}$ in the aqueous-phase in addition to CH_3SO_3 via HO_2, CH_3SO_3 via DMS and HOMSIA in the gas-phase during conditions with and without clouds.

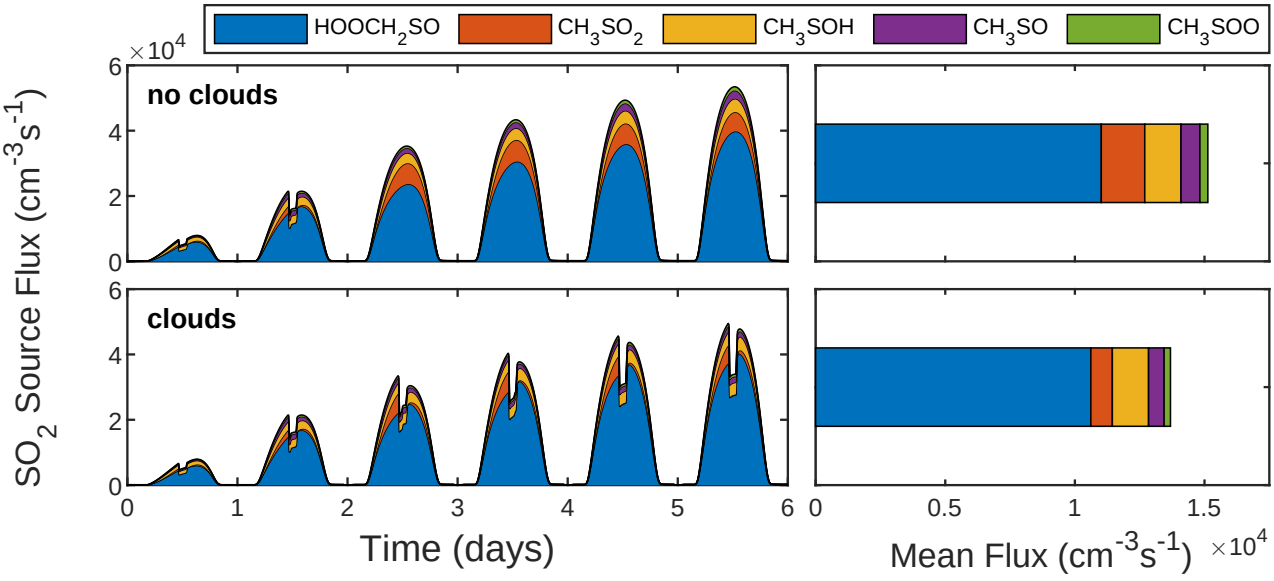

Figure S79. SO_2 source flux from $HOOCH_2SO$, CH_3SO_2, CH_3SOH, CH_3SO and CH_3SOO during conditions with and without clouds. Reactions that contribute < 1% of the total source flux are not displayed in the figure.

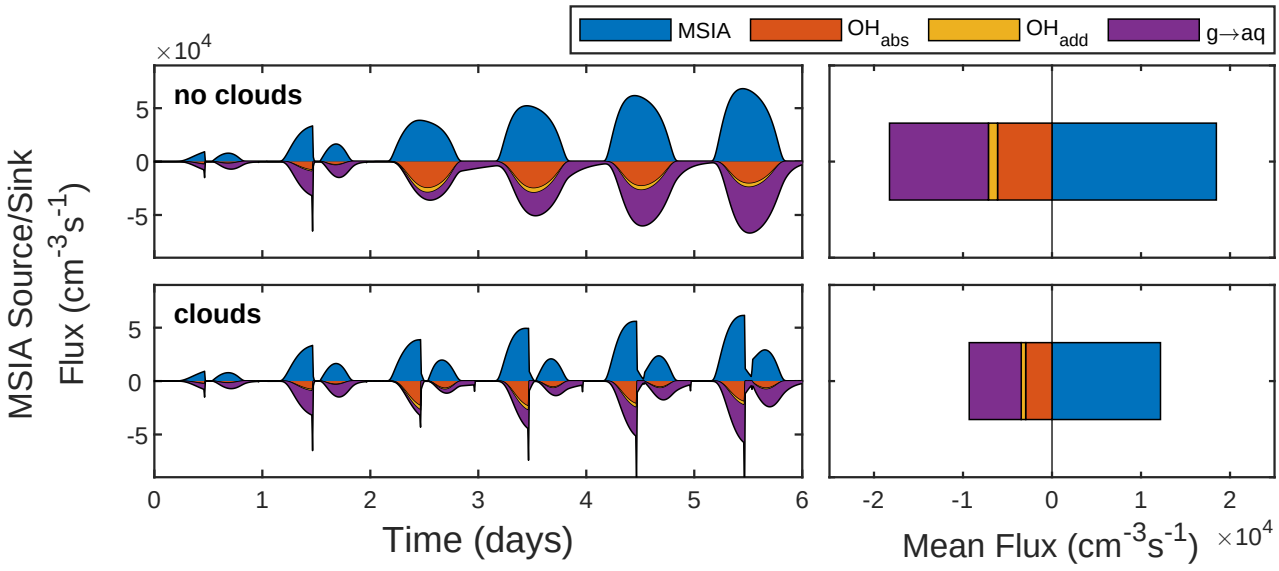

Figure S80. MSIA source/sink flux from DMSO and via reaction with OH (abstraction), OH (addition) and gas-aqueous phase uptake during conditions with and without clouds. Reactions that contribute < 1% of the total source/sink flux are not displayed in the figure.

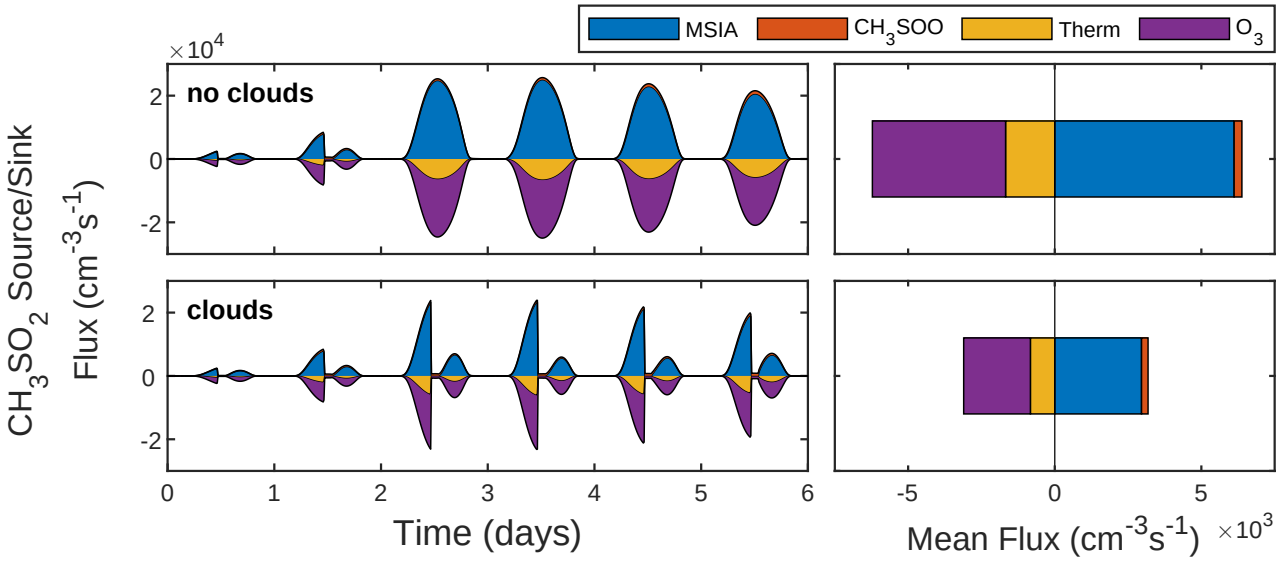

Figure S81. CH_3SO_2 source/sink flux from MSIA, CH_3SOO and via thermal decomposition and reaction with O_3 during conditions with and without clouds. Reactions that contribute < 1% of the total source/sink flux are not displayed in the figure.

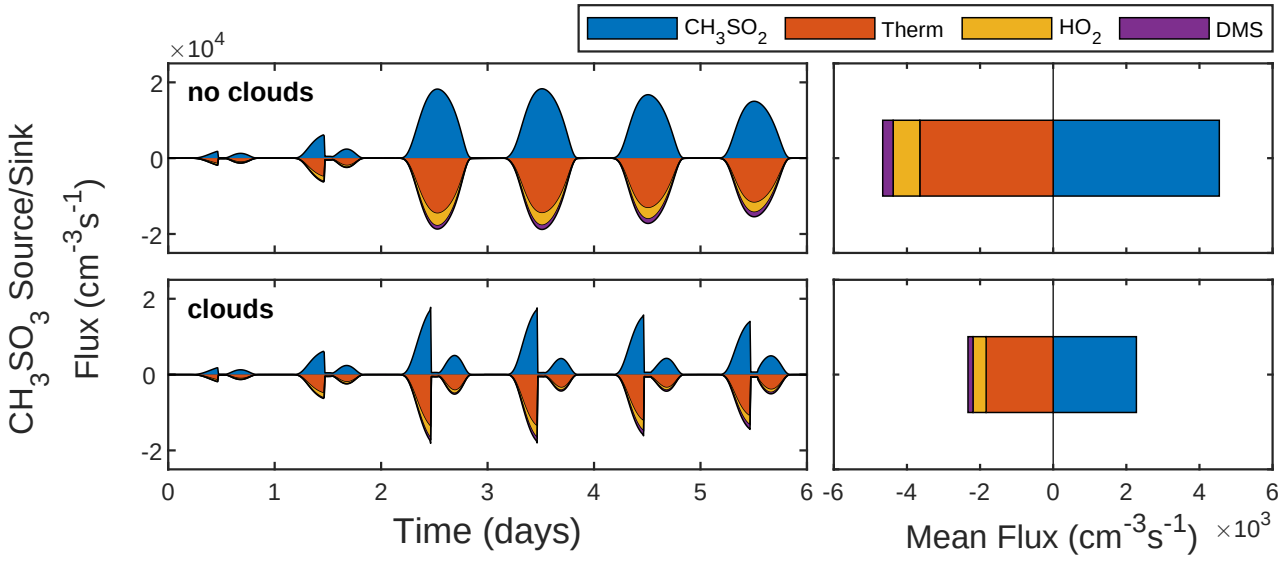

Figure S82. CH_3SO_3 source/sink flux from CH_3SO_2, via thermal decomposition and reaction with HO_2 and DMS during conditions with and without clouds. Reactions that contribute < 1% of the total source/sink flux are not displayed in the figure.

S11 Chemistry sensitivity runs

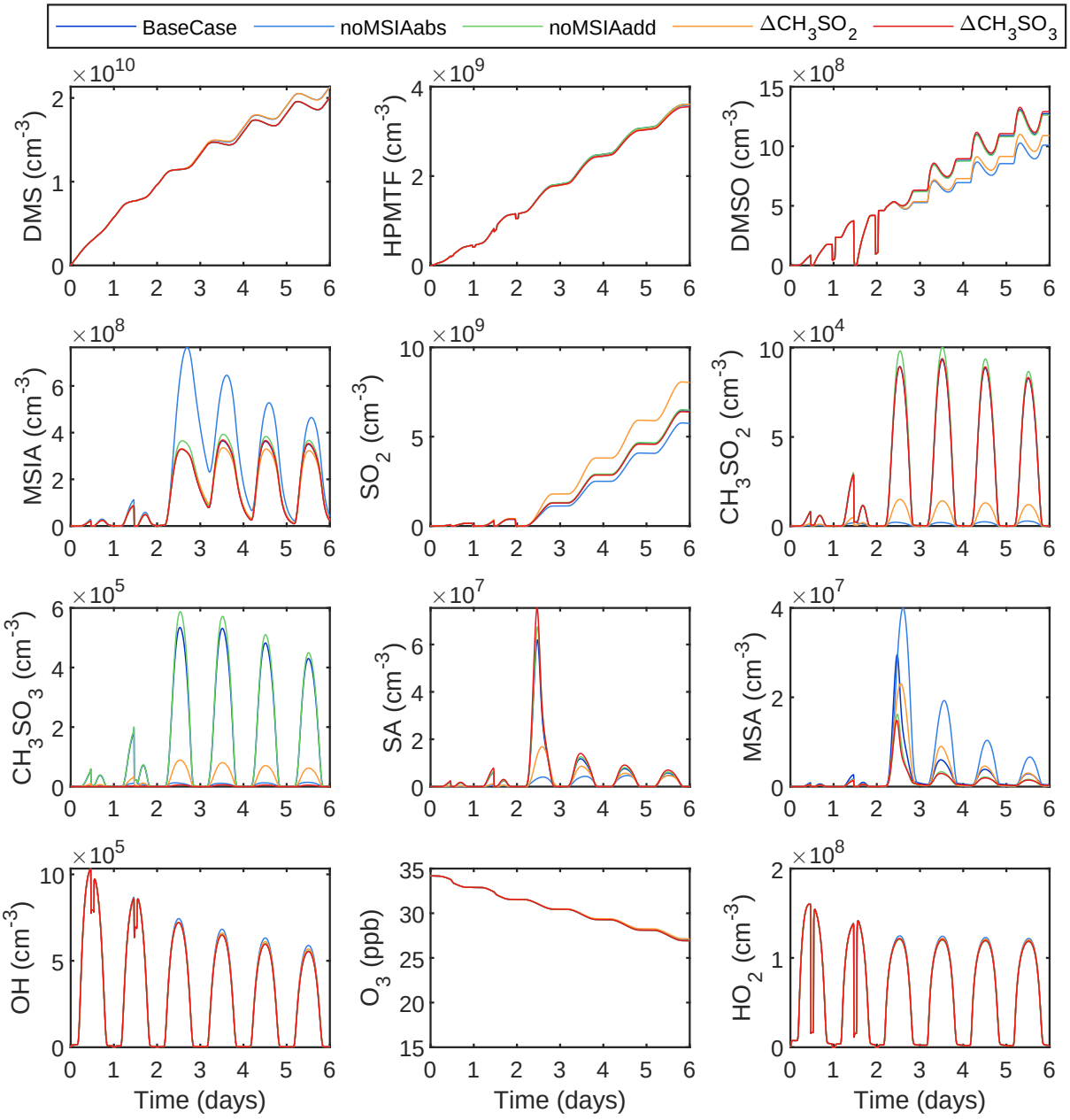

Figure S83. Concentrations of key gas-phase species for the BaseCase simulation and the noMSIAabs, noMSIAadd, ΔCH_3SO_2 and ΔCH_3SO_3 sensitivity runs.

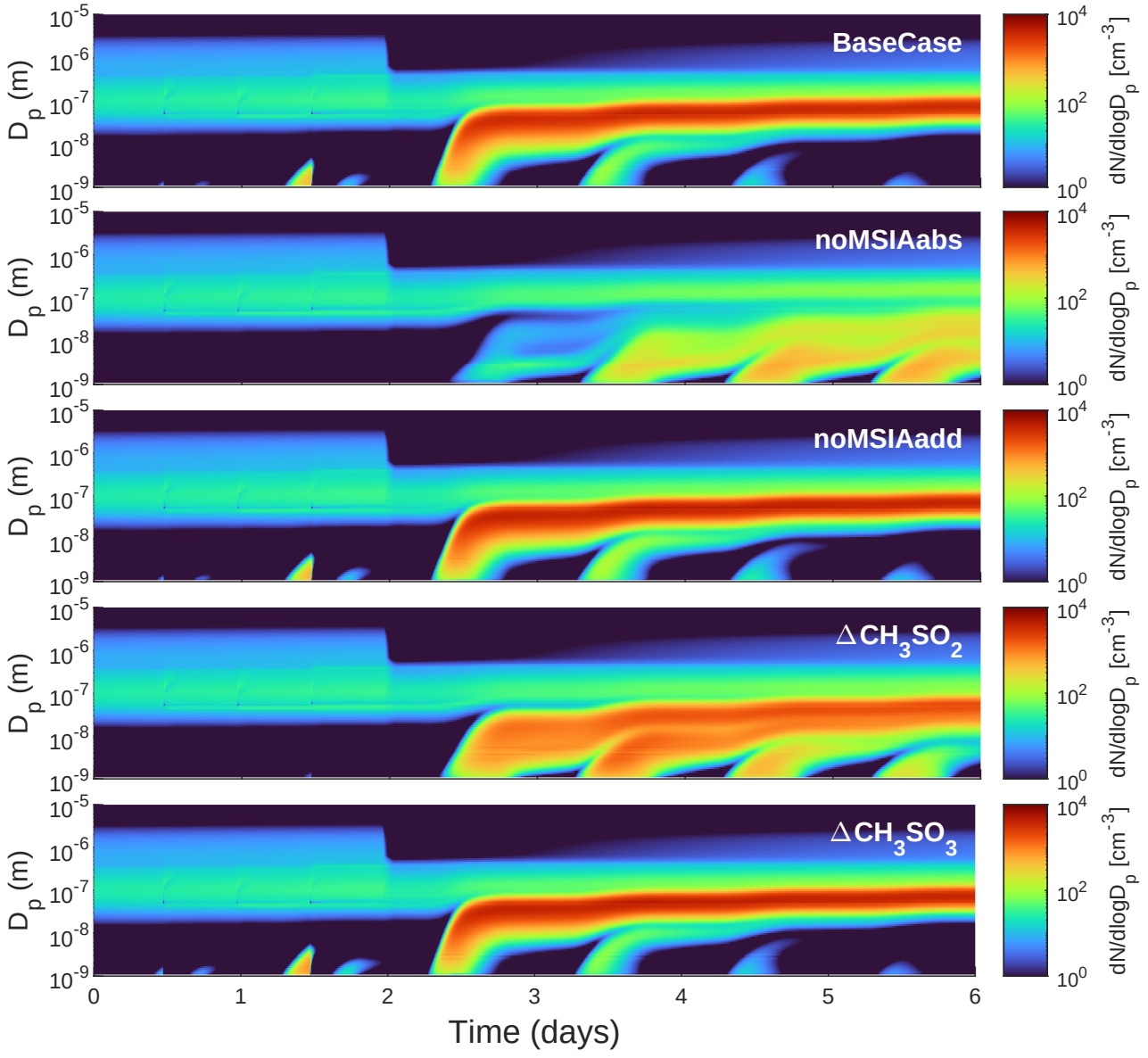

Figure S84. Aerosol particle number size distributions throughout the full simulation period for the BaseCase simulation and the noMSIAabs, noMSIAadd, ΔCH_3SO_2 and ΔCH_3SO_3 sensitivity runs.

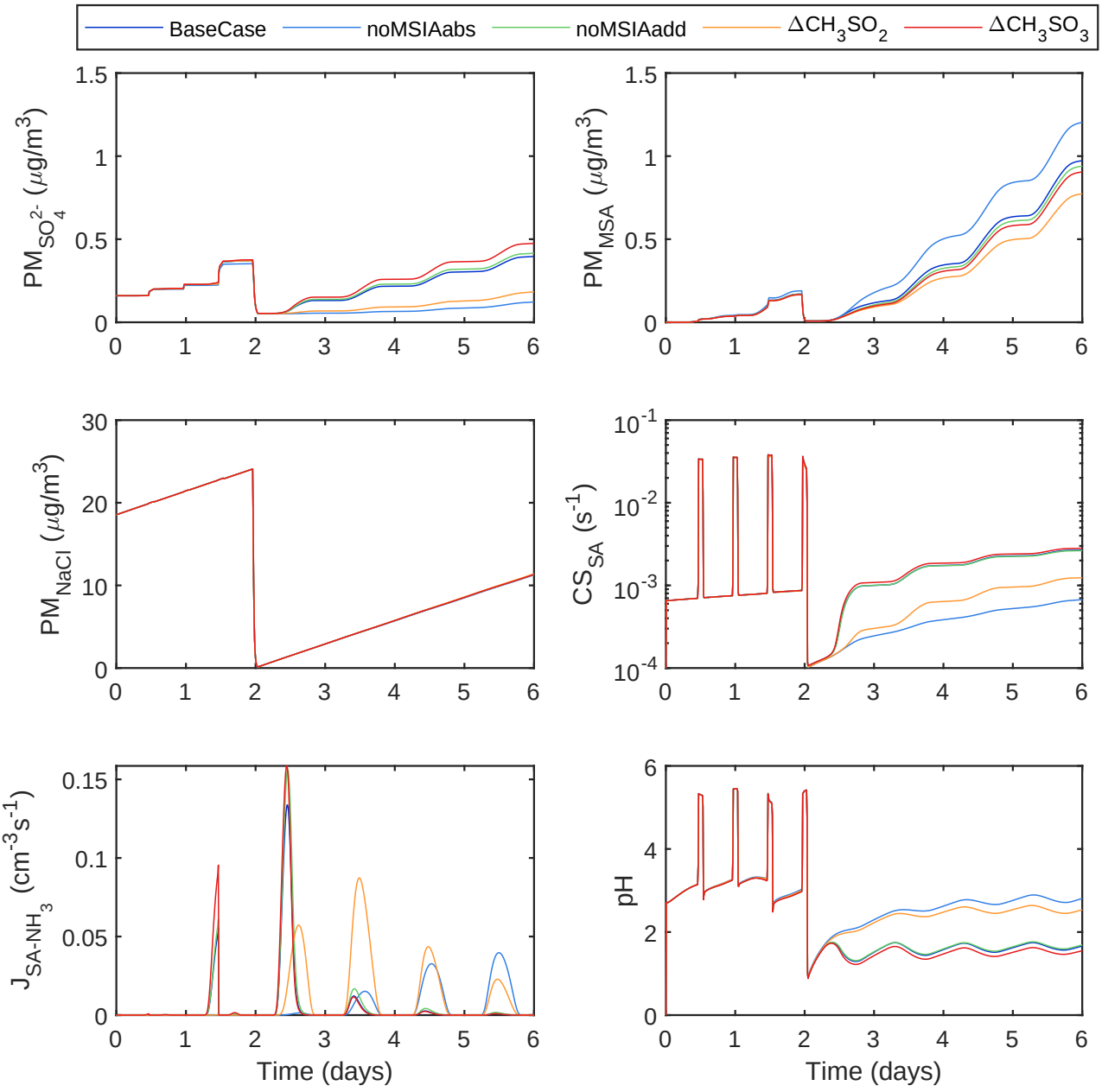

Figure S85. Total SO_4^{2-}, MSA and NaCl PM along with the SA condensation sink, SA-NH_3 driven nucleation rate and bulk pH for the BaseCase simulation and the noMSIAabs, noMSIAadd, ΔCH_3SO_2 and ΔCH_3SO_3 sensitivity runs.

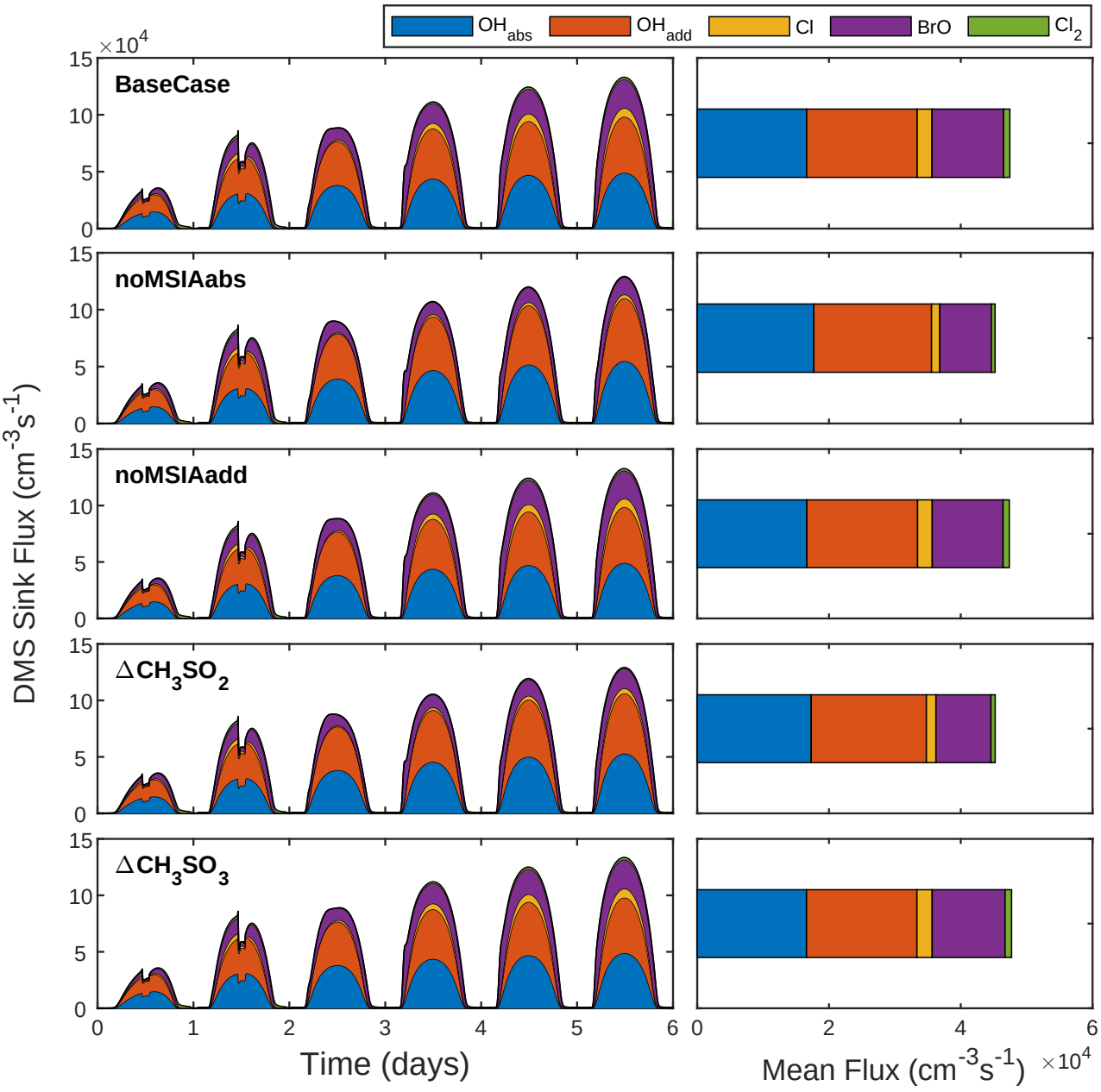

Figure S86. DMS sink flux driven by the reaction with OH (addition), OH (abstraction), Cl, Bro and Cl_2 for the BaseCase simulation and the noMSIAabs, noMSIAadd, ΔCH_3SO_2 and ΔCH_3SO_3 sensitivity runs. Reactions that contribute < 1% of the total sink flux are not displayed in the figure.

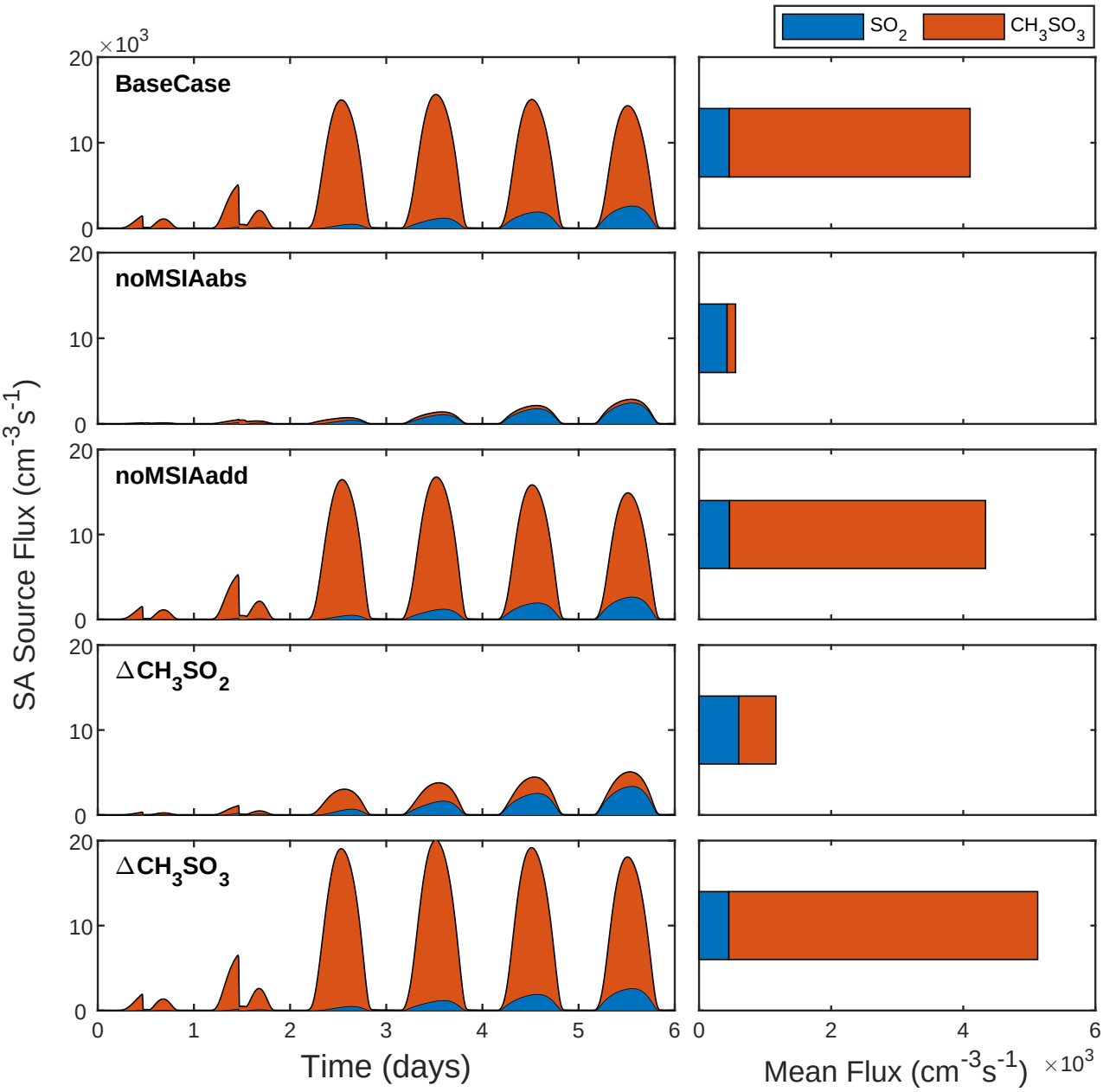

Figure S87. SA source flux from SO_2 and CH_3SO_3 for the BaseCase simulation and the noMSIAabs, noMSIAadd, ΔCH_3SO_2 and ΔCH_3SO_3 sensitivity runs.

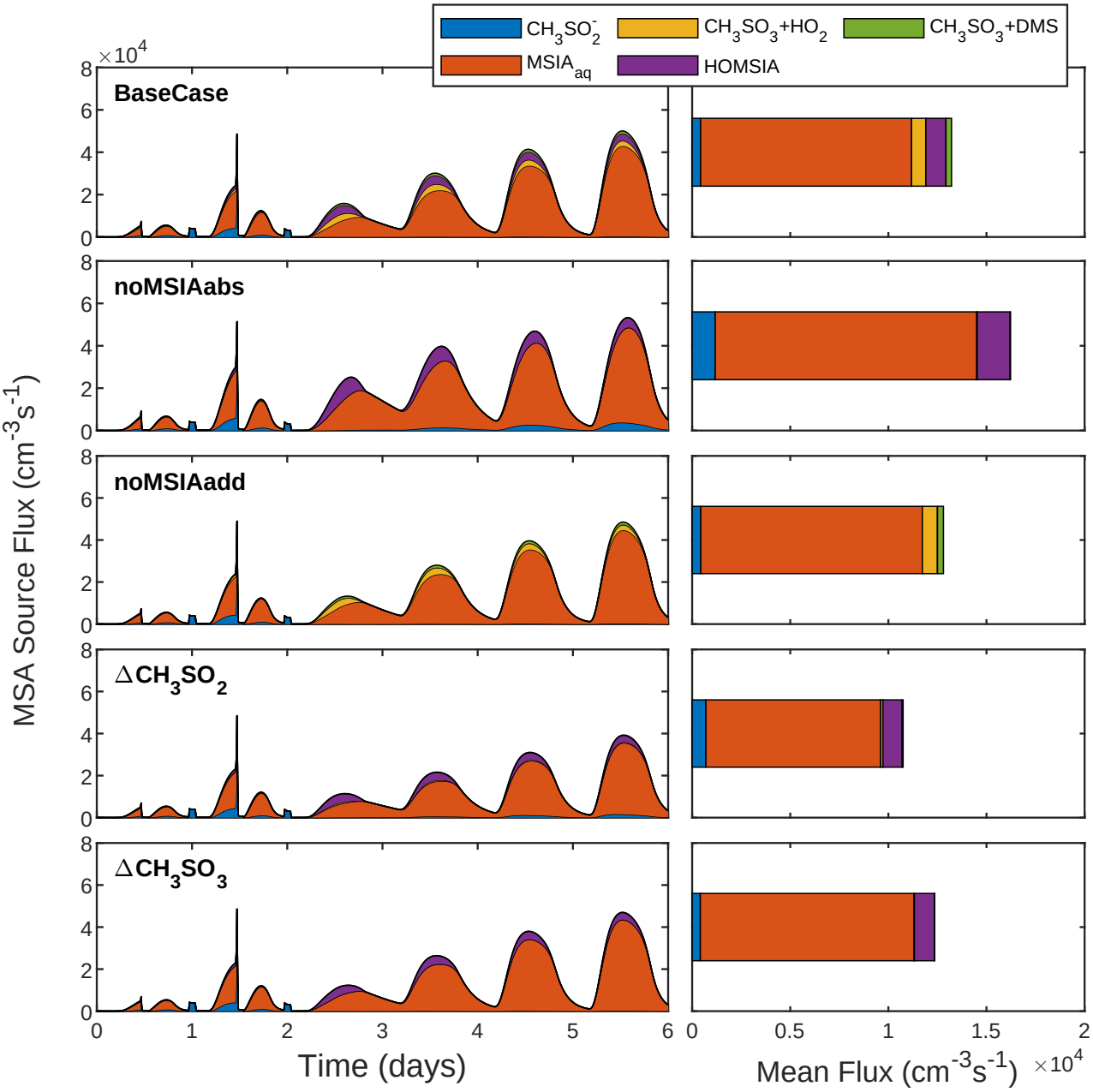

Figure S88. MSA source flux from $CH_3SO_2^-$ and $MSIA_{aq}$ in the aqueous-phase in addition to CH_3SO_3 via HO_2, CH_3SO_3 via DMS and HOMSIA in the gas-phase for the BaseCase simulation and the noMSIAabs, noMSIAadd, ΔCH_3SO_2 and ΔCH_3SO_3 sensitivity runs.

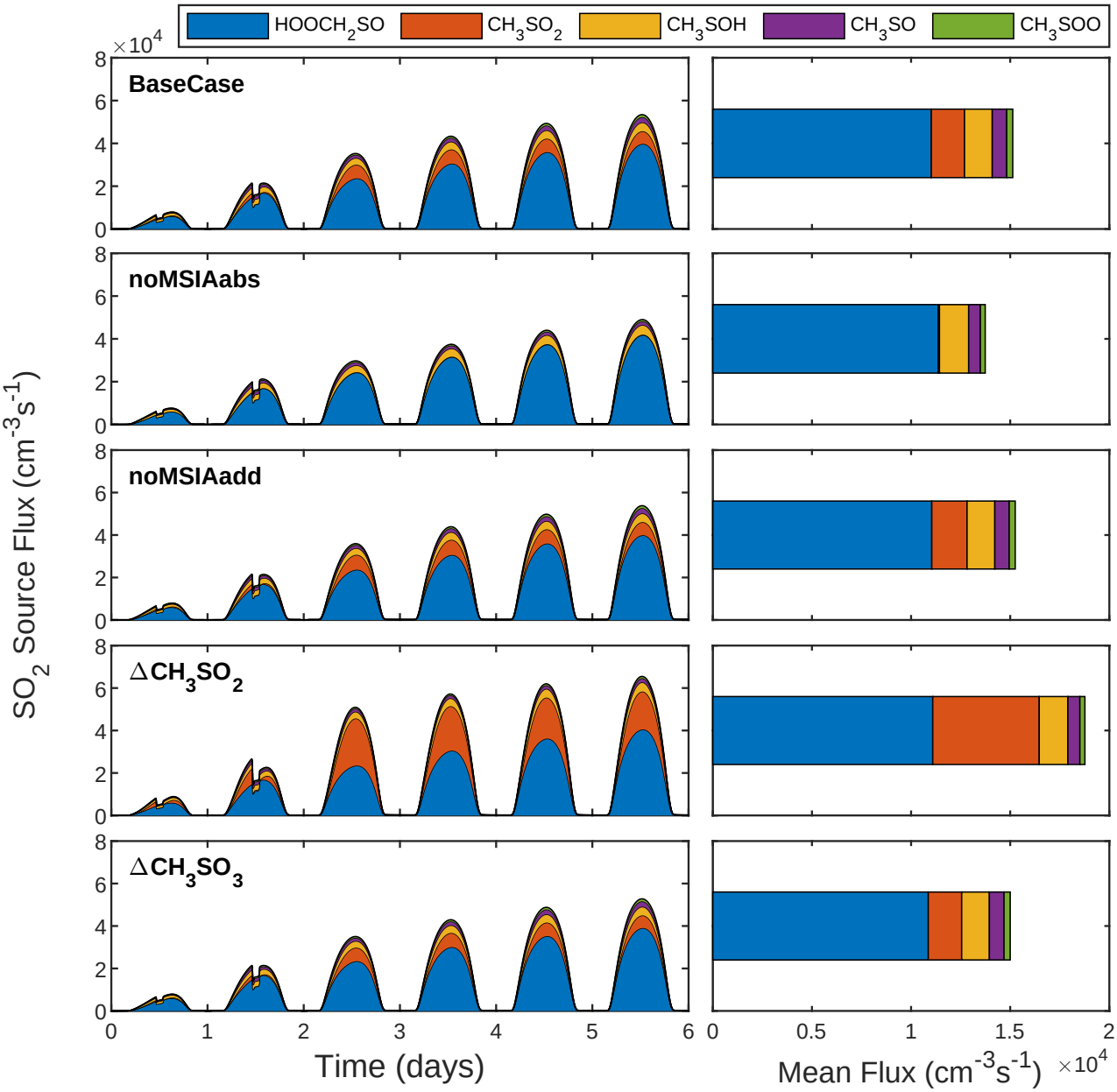

Figure S89. SO_2 source flux from $HOOCH_2SO$, CH_3SO_2, CH_3SOH, CH_3SO and CH_3SOO for the BaseCase simulation and the noMSIAabs, noMSIAadd, ΔCH_3SO_2 and ΔCH_3SO_3 sensitivity runs. Reactions that contribute < 1% of the total source flux are not displayed in the figure.

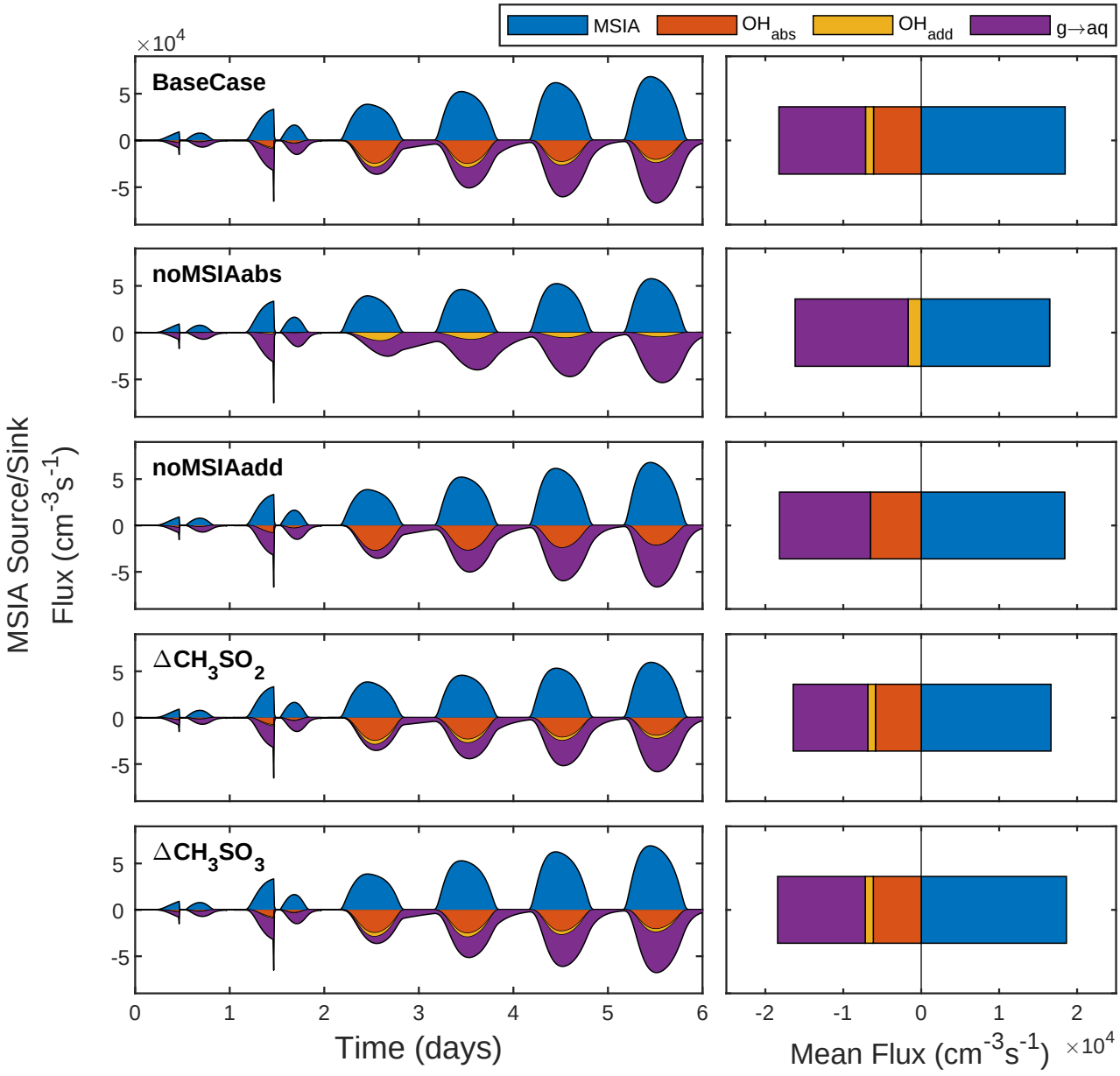

Figure S90. MSIA source/sink flux from DMSO and via reaction with OH (abstraction), OH (addition) and gas-aqueous phase uptake for the BaseCase simulation and the noMSIAabs, noMSIAadd, ΔCH_3SO_2 and ΔCH_3SO_3 sensitivity runs. Reactions that contribute < 1% of the total source/sink flux are not displayed in the figure.

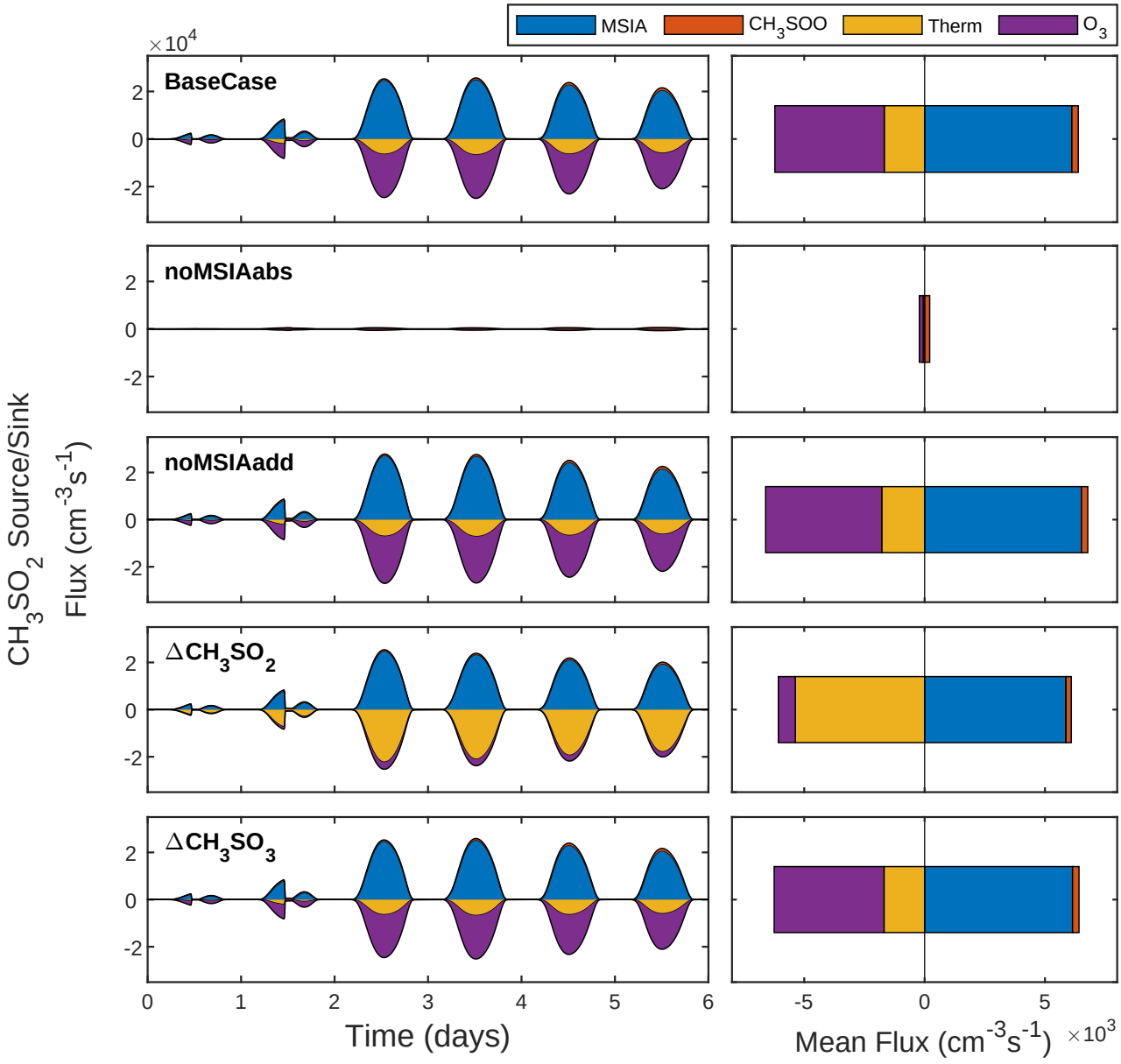

Figure S91. CH_3SO_2 source/sink flux from MSIA, CH_3SOO and via thermal decomposition and reaction with O_3 for the BaseCase simulation and the noMSIAabs, noMSIAadd, ΔCH_3SO_2 and ΔCH_3SO_3 sensitivity runs. Reactions that contribute < 1% of the total source/sink flux are not displayed in the figure.

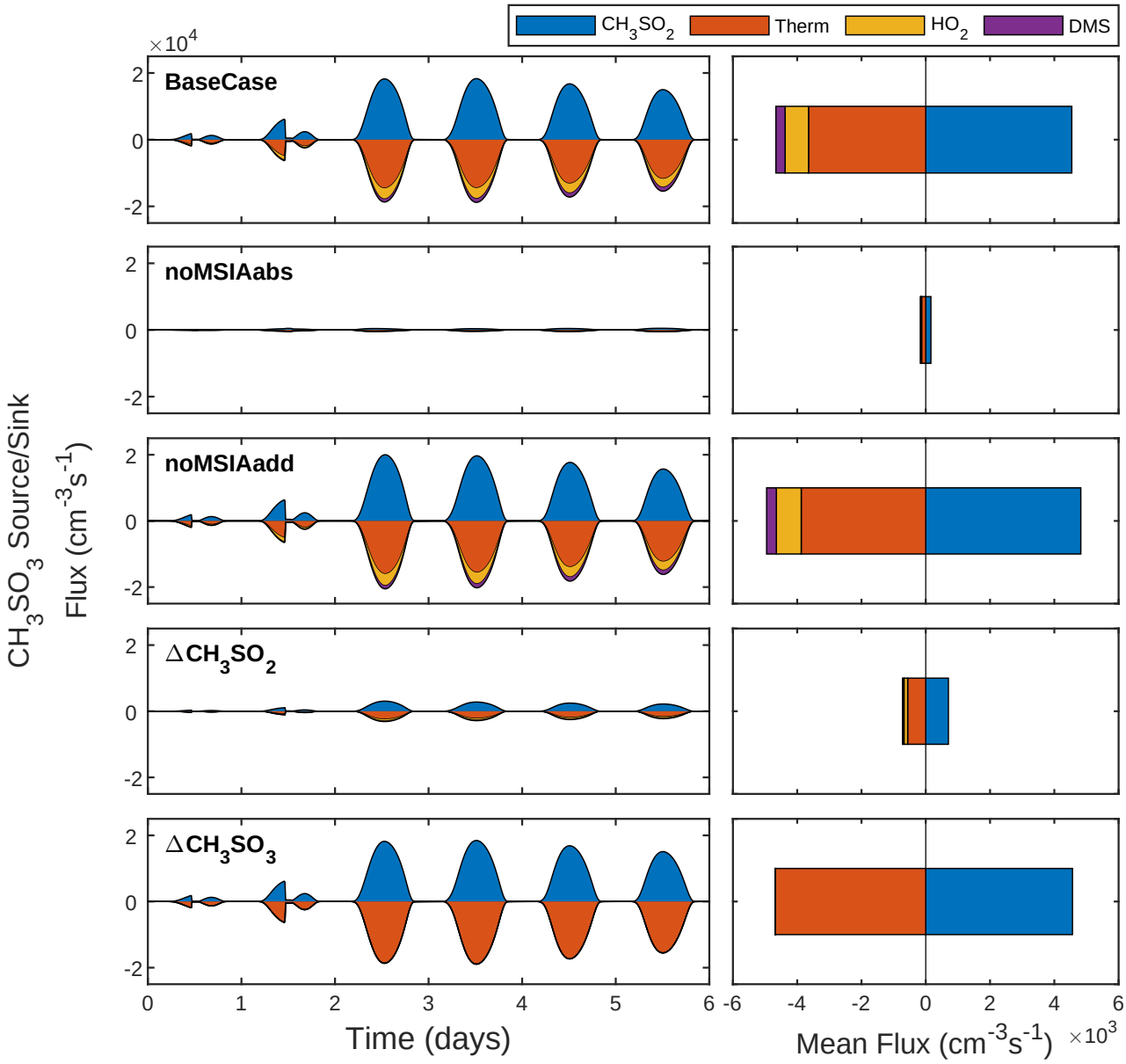

Figure S92. CH_3SO_3 source/sink flux from CH_3SO_2, via thermal decomposition and reaction with HO_2 and DMS for the BaseCase simulation and the noMSIAabs, noMSIAadd, ΔCH_3SO_2 and ΔCH_3SO_3 sensitivity runs. Reactions that contribute < 1% of the total source/sink flux are not displayed in the figure.

References

Berndt, T., Chen, J., Møller, K., Hyttinen, N., Prisle, N., Tilgner, A., Hoffmann, E., Herrmann, H., and Kjaergaard, H.: SO2 formation and peroxy radical isomerization in the atmospheric reaction of OH radicals with dimethyl disulfide, Chemical communications (Cambridge, England), 56, 13 634–13 637, https://doi.org/10.1039/d0cc05783e, 2020.

Gonzalez-García, N., Gonzalez-Lafont, À., and Lluch, J. M.: Methanesulfinic Acid Reaction with OH: Mechanism, Rate Constants, and Atmospheric Implications, The Journal of Physical Chemistry A, 111, 7825–7832, https://doi.org/10.1021/jp072260z, 2007.

Hoffmann, E. H., Tilgner, A., Schrödner, R., Bräuer, P., Wolke, R., and Herrmann, H.: An advanced modeling study on the impacts and atmospheric implications of multiphase dimethyl sulfide chemistry, Proceedings of the National Academy of Sciences, 113, 11 776–11 781, https://doi.org/10.1073/pnas.1606320113, 2016.

Jacob, L. S. D., Giorio, C., and Archibald, A. T.: Extension, development, and evaluation of the representation of the OH-initiated dimethyl sulfide (DMS) oxidation mechanism in the Master Chemical Mechanism (MCM) v3.3.1 framework, Atmospheric Chemistry and Physics, 24, 3329–3347, https://doi.org/10.5194/acp-24-3329-2024, 2024.

Kukui, A., Borissenko, D., Laverdet, G., and Bras, G.: Gas-Phase Reactions of OH Radicals with Dimethyl Sulfoxide and Methane Sulfinic Acid Using Turbulent Flow Reactor and Chemical Ionization Mass Spectrometry, Journal of Physical Chemistry A, 107, https://doi.org/10.1021/jp0276911, 2003.

Lv, G., Zhang, C., and Sun, X.: Understanding the oxidation mechanism of methanesulfinic acid by ozone in the atmosphere, Scientific Reports, 9, 322, https://doi.org/10.1038/s41598-018-36405-0, 2019.

Veres, P. R., Neuman, J. A., Bertram, T. H., Assaf, E., Wolfe, G. M., Williamson, C. J., Weinzierl, B., Tilmes, S., Thompson, C. R., Thames, A. B., Schroder, J. C., Saiz-Lopez, A., Rollins, A. W., Roberts, J. M., Price, D., Peischl, J., Nault, B. A., Møller, K. H., Miller, D. O., Meinardi, S., Li, Q., Lamarque, J.-F., Kupc, A., Kjaergaard, H. G., Kinnison, D., Jimenez, J. L., Jernigan, C. M., Hornbrook, R. S., Hills, A., Dollner, M., Day, D. A., Cuevas, C. A., Campuzano-Jost, P., Burkholder, J., Bui, T. P., Brune, W. H., Brown, S. S., Brock, C. A., Bourgeois, I., Blake, D. R., Apel, E. C., and Ryerson, T. B.: Global airborne sampling reveals a previously unobserved dimethyl sulfide oxidation mechanism in the marine atmosphere, Proceedings of the National Academy of Sciences, 117, 4505–4510, https://doi.org/10.1073/pnas.1919344117, 2020.

Wu, R., Wang, S., and Wang, L.: A New Mechanism for The Atmospheric Oxidation of Dimethyl Sulfide. The Importance of Intramolecular Hydrogen Shift in CH3SCH2OO Radical., The journal of physical chemistry. A, 119, https://doi.org/10.1021/jp511616j, 2014.

Ye, Q., Goss, M. B., Krechmer, J. E., Majluf, F., Zaytsev, A., Li, Y., Roscioli, J. R., Canagaratna, M., Keutsch, F. N., Heald, C. L., and Kroll, J. H.: Product distribution, kinetics, and aerosol formation from the OH oxidation of dimethyl sulfide under different RO_2 regimes, Atmospheric Chemistry and Physics, 22, 16 003–16 015, https://doi.org/10.5194/acp-22-16003-2022, 2022.

Yin, F., Grosjean, D., Flagan, R. C., and Seinfeld, J. H.: Photooxidation of dimethyl sulfide and dimethyl disulfide. II: Mechanism evaluation, Journal of Atmospheric Chemistry, 11, 365–399, https://doi.org/10.1007/BF00053781, 1990.